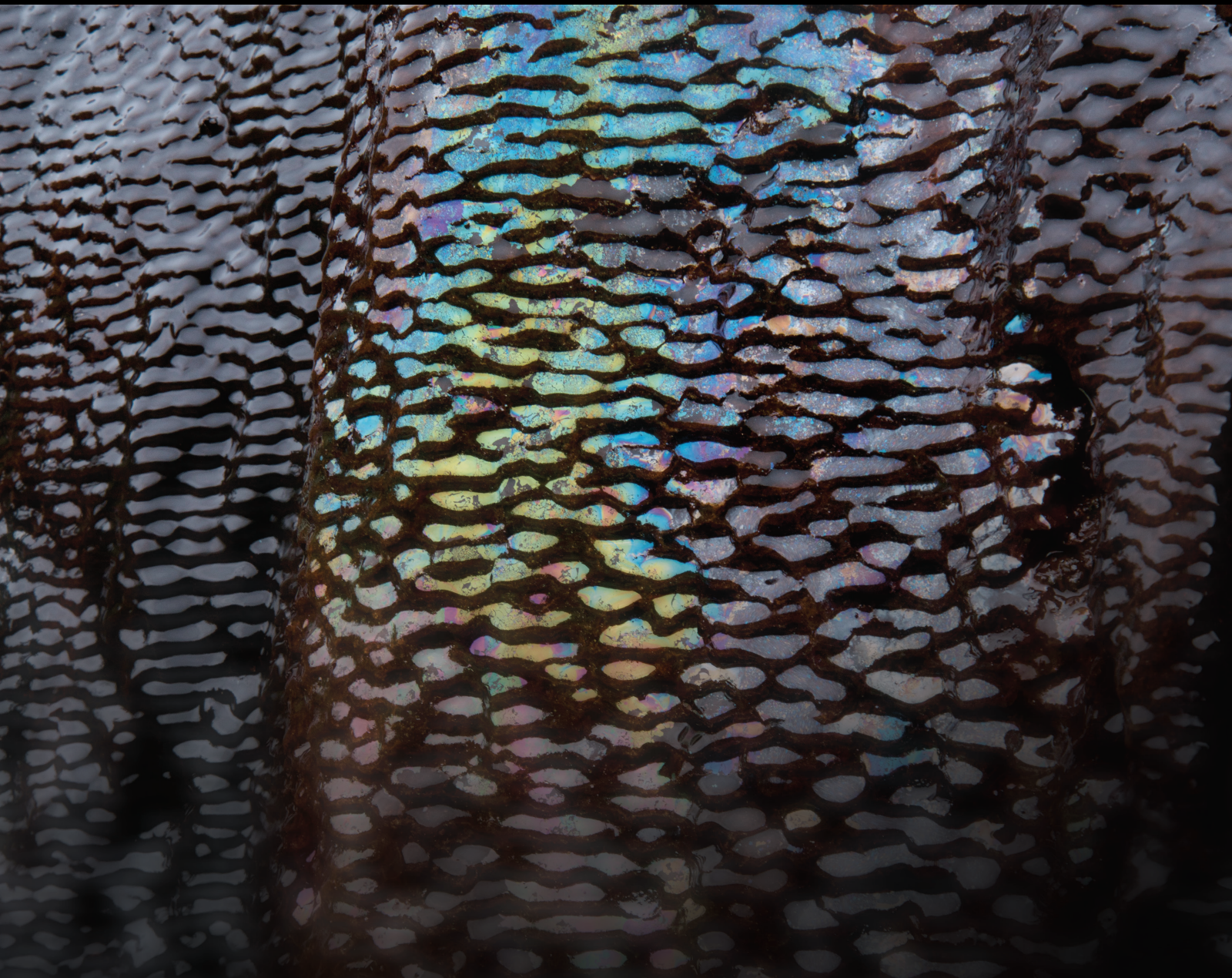


Advancement in Coupled Flow and Phase Behavior in Unconventional Reservoirs

Lead Guest Editor: Bao Jia

Guest Editors: Dr. Kouqi Liu, Ruyi Zheng, and Chenggang Xian





**Advancement in Coupled Flow and Phase
Behavior in Unconventional Reservoirs**

**Advancement in Coupled Flow and
Phase Behavior in Unconventional
Reservoirs**

Lead Guest Editor: Bao Jia

Guest Editors: Dr. Kouqi Liu, Ruyi Zheng, and
Chenggang Xian







Copyright © 2023 Hindawi Limited. All rights reserved.

This is a special issue published in "Geofluids." All articles are open access articles distributed under the Creative Commons Attribution License, which permits unrestricted use, distribution, and reproduction in any medium, provided the original work is properly cited.



























Chief Editor

































Umberta Tinivella, Italy

Associate Editors

Paolo Fulignati , Italy
Huazhou Li , Canada
Stefano Lo Russo , Italy
Julie K. Pearce , Australia

Academic Editors

Basim Abu-Jdayil , United Arab Emirates
Hasan Alsaedi , USA
Carmine Apollaro , Italy
Baojun Bai, USA
Marino Domenico Barberio , Italy
Andrea Brogi , Italy
Shengnan Nancy Chen , Canada
Tao Chen , Germany
Jianwei Cheng , China
Paola Cianfarra , Italy
Daniele Cinti , Italy
Timothy S. Collett , USA
Nicoló Colombani , Italy
Mercè Corbella , Spain
David Cruset, Spain
Jun Dong , China
Henrik Drake , Sweden
Farhad Ehya , Iran
Lionel Esteban , Australia
Zhiqiang Fan , China
Francesco Frondini, Italy
Ilaria Fuoco, Italy
Paola Gattinoni , Italy
Amin Gholami , Iran
Michela Giustiniani, Italy
Naser Golsanami, China
Fausto Grassa , Italy
Jianyong Han , China
Chris Harris , South Africa
Liang He , China
Sampath Hewage , Sri Lanka
Jian Hou, China
Guozhong Hu , China
Lanxiao Hu , China
Francesco Italiano , Italy
Azizollah Khormali , Iran
Hailing Kong, China

Karsten Kroeger, New Zealand
Cornelius Langenbruch, USA
Peter Leary , USA
Guangquan Li , China
Qingchao Li , China
Qibin Lin , China
Marcello Liotta , Italy
Shuyang Liu , China
Yong Liu, China
Yueliang Liu , China
Constantinos Loupasakis , Greece
Shouqing Lu, China
Tian-Shou Ma, China
Judit Mádl-Szonyi, Hungary
Paolo Madonia , Italy
Fabien Magri , Germany
Micòl Mastroicco , Italy
Agnes Mazot , New Zealand
Yuan Mei , Australia
Evgeniy M. Myshakin , USA
Muhammad Tayyab Naseer, Pakistan
Michele Paternoster , Italy
Mandadige S. A. Perera, Australia
Marco Petitta , Italy
Chao-Zhong Qin, China
Qingdong Qu, Australia
Reza Rezaee , Australia
Eliahu Rosenthal , Israel
Gernot Rother, USA
Edgar Santoyo , Mexico
Mohammad Sarmadivaleh, Australia
Venkatramanan Senapathi , India
Amin Shokrollahi, Australia
Rosa Sinisi , Italy
Zhao-Jie Song , China
Ondra Sracek , Czech Republic
Andri Stefansson , Iceland
Bailu Teng , China
Tivadar M. Tóth , Hungary
Orlando Vaselli , Italy
Benfeng Wang , China
Hetang Wang , China
Wensong Wang , China
Zhiyuan Wang , China
Ruud Weijermars , Saudi Arabia


Bisheng Wu , China
Da-yang Xuan , China
Yi Xue , China
HE YONGLIANG, China
Fan Yang , China
Zhenyuan Yin , China
Sohrab Zendeboudi, Canada
Zhixiong Zeng , Hong Kong
Yuanyuan Zha , China
Keni Zhang, China
Mingjie Zhang , China
Rongqing Zhang, China
Xianwei Zhang , China
Ye Zhang , USA
Zetian Zhang , China
Ling-Li Zhou , Ireland
Yingfang Zhou , United Kingdom
Daoyi Zhu , China
Quanle Zou, China
Martina Zucchi, Italy

Contents


The Time-Varying Variation Characteristics of Methane during Nitrogen Injection Process: An Experimental Study on Bituminous Coals

Aoxiang Zhang , Longyong Shu , Zhonggang Huo, and Xin Song
Research Article (11 pages), Article ID 5075888, Volume 2023 (2023)




Influence of Water Saturation on Adsorption Behavior at Liquid-Liquid Interfaces in Unsaturated Porous Media

Yan Zhu , Ziteng Cui , Kun Li, Chaoqi Wang , Zhao Li , Xueyi Zhang , and Zhi Dou 
Research Article (12 pages), Article ID 8155349, Volume 2023 (2023)



Evolutions of Anisotropic Hydraulic Properties of Rough-Walled Rock Fractures under Different Shear Displacements

Dapeng Lu 
Research Article (13 pages), Article ID 8841361, Volume 2023 (2023)

Stress Sensitivity of Proppant-Containing Fractures and Its Influence on Gas Well Productivity

Hao Chen , Jianfei Wei, Hanlie Cheng , Qiang Qin , Ying Chen, and Linqiang Zhang
Research Article (10 pages), Article ID 8851149, Volume 2023 (2023)

Characteristics and Gas-Bearing Properties of Yanchang Formation Shale Reservoirs in the Southern Ordos Basin

Zhendong Gao, Yongdong Wang, Xiaoyu Gu, Hanlie Cheng , and Nnamdi Puppe 
Research Article (9 pages), Article ID 5894458, Volume 2023 (2023)

Research Article

The Time-Varying Variation Characteristics of Methane during Nitrogen Injection Process: An Experimental Study on Bituminous Coals

Aoxiang Zhang , Longyong Shu , Zhonggang Huo, and Xin Song

China Coal Research Institute, Beijing 100013, China

Correspondence should be addressed to Longyong Shu; slyccri@163.com

Received 8 May 2023; Revised 30 November 2023; Accepted 30 November 2023; Published 11 December 2023

Academic Editor: Kouqi Liu

Copyright © 2023 Aoxiang Zhang et al. This is an open access article distributed under the Creative Commons Attribution License, which permits unrestricted use, distribution, and reproduction in any medium, provided the original work is properly cited.

The existing research on CH₄ displacement by N₂ mainly focuses on the gas injection displacement mechanism and the factors affecting displacement efficiency. And most of them are theoretical analyses at the model level or multifactor analyses at the simulation test level, while there are few targeted physical simulation tests and quantitative analyses. Given the above problems, the experiment system was used to study the gas migration evolution law and time-varying characteristics of CH₄ displacement by N₂ in coal under different injection pressures. The experimental results show that the whole process of CH₄ displacement by N₂ can be divided into three stages: stage I (original equilibrium stage); stage II (dynamic balance stage); stage III (new equilibrium stage). The concentration of CH₄ and N₂ presents an opposite variation trend, and the variation rate of CH₄ and N₂ increased first and then decreased. The breakthrough time was 50 minutes, 45 minutes, 35 minutes, 25 minutes, and 20 minutes, respectively, under different injection pressures. The displacement efficiency increased with the injection pressures, while the replacement ratio decreased with the injection pressures. The maximum flow rate of CH₄ was 0.085 mL/min, 0.110 mL/min, 0.130 mL/min, 0.222 mL/min, and 0.273 mL/min, respectively, under different injection pressures. The accumulated production of CH₄ was 3.59 mL, 3.91 mL, 4.39 mL, 5.58 mL, and 5.94 mL, respectively, under different injection pressures. The effective injection pressure range was 1.6~2 MPa. This research can provide a reference for the theoretical research of N₂-ECBM-related technology in low permeability reservoirs and the selection of injection pressure in the field technology implementation.

1. Introduction

Coalbed methane is a fossil energy associated with the natural evolution of coal [1]. The development of coalbed methane cannot only ensure the safe production of coal mines but also alleviate the increasingly severe energy crisis [2, 3]. Borehole gas extraction has become the main way to prevent gas disasters and develop coalbed methane [4–6]. Coal seams are a dual porous medium composed of coal matrix blocks and interblock fractures [7, 8]. The adsorbed gas and the free gas in the cracks reach equilibrium under a certain pressure [9]. The extraction drilling hole can form a gas pressure gradient, promoting the free gas in the fractures to flow towards the drilling hole [10–12]. With the extension of

the extraction time, the gas pressure in the coal seam fractures gradually decreases [13]. The dynamic equilibrium between the adsorbed gas and the free gas is broken, and the adsorbed gas is desorbed and diffused from the matrix to the fractures [14, 15]. However, with the progress of gas extraction, the gas pressure gradient between the coal seam and the borehole also gradually decreases [16–18].

Conventional enhanced extraction technology can be divided into three categories: mechanical methods, physical methods, and chemical methods [19–22]. The physical properties of coal and external technology in this process are transformed and utilized, which constitutes the main content of the enhanced extraction technology [23–25]. However, low permeability, low reservoir pressure, and low

gas content are the characteristics of coal reservoirs in China. Conventional enhanced extraction technologies are not effective in this type of reservoir. Due to its particularity, gas injection technology can effectively improve the gas extraction efficiency by increasing the gas driving force and reducing the effective stress and the gas partial pressure [26]. Thus, the gas injection technology can rapidly reduce the gas content in the coal seam and ensure mining safety.

There have been several theoretical and experimental studies on gas injection technology. Longinos et al. examined the efficacy of liquid nitrogen in the coal fracturing process in coalbed methane reservoirs [27–29]. Wu et al. developed a dual pores model for enhanced methane recovery by CO₂ injection [30]. Kumar et al. developed a coupled finite element (FE) model to study the heterogeneously permeable coal reservoirs [31]. Ozdemir established a mixed-gas-coupled seepage model of porous media, taking into account the effect of moisture in coal [32]. Huang et al. established a water-gas two-phase coupled seepage model which considered the influence of water on gas seepage [33]. Seto et al. established a gas-water two-phase flow model which considered the interaction of gases (CO₂, N₂, CH₄, and H₂O) in the coal seam [34]. Xia et al. used a coupled composition model to study the effect of borehole sealing on gas emissions [35]. There are also several field trials of enhanced methane recovery involving gas injection. The United States conducted CO₂-ECBM test and N₂-ECBM test at the Allison Unit and Tiffany Unit, respectively [36]. Canada had conducted a gas injection test for CO₂ storage in Alberta Province [37]. The European Union's RECOPOL project was first implemented in Poland, with a gas injection depth of 1050 m [38]. Japan had conducted a field test of gas injection to replace coalbed methane in Hokkaido [39, 40]. China and Canada jointly carried out a study that focused on the recovery enhancement of coalbed methane in the Qinshui Basin, Shanxi Province [41, 42].

In this paper, we investigated the gas migration law and time-varying characteristics of CH₄ displacement by N₂ in coal under different injection pressures by a physical simulation experiment. Based on the above results, this research can provide a reference for the theoretical research of N₂-ECBM-related technology in low permeability coal seams and the selection of injection pressure in the field technology implementation.

2. Materials and Methods

2.1. Sample Collection and Preparation. The raw coal samples were collected from the Tashan mine in Shanxi, China. The raw coal samples were made into cylindrical coal samples with specifications of 50 mm in length and 25 mm in diameter. The raw coal and cylindrical coal samples are shown in Figure 1.

2.2. Experimental Equipment. The experiment uses HA-I multiphase flow permeameter test device (Figure 2). Its main technical parameters include (1) maximum working pressure: annular pressure: 25 MPa, accuracy: ± 0.01 MPa; injection pressure: 20 MPa, accuracy: 0.01 MPa; ring pressure:

20 MPa, accuracy: ± 0.01 MPa; (2) maximum working temperature: 120°C, accuracy: ± 0.1 °C; and (3) specification of the core holder: 25 mm, 50 mm, and 60 mm (diameter).

The instrument mainly includes the following systems: (1) core clamping system: the core is wrapped by polytetrafluoroethylene casing; (2) gas injection system: gas can be injected into the core holder under constant pressure; (3) pressure system: the back pressure is controlled by the back pressure valve, and the annular pressure is the pressure loaded around the core by the injection pump; (4) data metering system: the inlet and outlet ends of the core holder are, respectively, equipped with a pressure sensor for real-time monitoring of the pressure values at both ends, and the gas component detector and drainage method are used to measure the flow rate of the mixed gas; (5) temperature control system: temperature control adopts thermostat air bath heating, temperature range: 20°C–120°C. The schematic diagram of the device is shown in Figure 3.

2.3. Experimental Scheme. The influence of different injection pressures on the process of CH₄ displacement by N₂ was analyzed. The standard coal sample size is 25 × 50 mm. The experiment adopts a true triaxial loading: the confining pressure is 4.0 MPa, and the axial pressure is 2 MPa. The adsorption pressure of CH₄ is 1 MPa, and the adsorption time is 24 h, which ensures that the pressure remains stable and the flow remains unchanged within 30 min when the adsorption is saturated. The N₂ injection pressure is within the range of 0.5–2.5 MPa, and the ambient temperature is set at 25°C. Specific experimental parameters are shown in Table 1.

2.4. Experimental Procedures. The following are the experimental operation steps: (1) replace the test sample with a solid cushion block, connect the instrument, and check the air tightness of the test device; (2) put the coal sample (25 × 50 mm) into the holder; (3) add an axial pressure of 1 MPa first, and then the ring pressure of 2 MPa, and pressurize alternately step by step until the ring pressure is 4 MPa, and the axial pressure is 2 MPa; (4) vacuum the whole system for 2 hours; (5) inject 1 MPa methane into the holder through the pressurization system, close the downstream valve, and maintain it for 12 hours to ensure complete adsorption; (6) inject 0.5, 1, 1.5, 2, and 2.5 MPa nitrogen, respectively, open the downstream valve, and connect the gas detector to analyze the outlet gas concentration; (7) when measuring the flow, close the branch valve of the gas detector, open the flow valve, and measure the flow. Switch back to the gas detector branch in time after measurement; (8) collect the monitoring data, record the flow, and the gas detector shows that the concentration of each gas is not changing; (9) after the test, relieve the pressure step by step and disassemble the test device.

3. Results

3.1. Conversion Process of CH₄ Displaced by N₂. The displacement of CH₄ by N₂ is a dynamic process. The released gas volume changed constantly under different injection

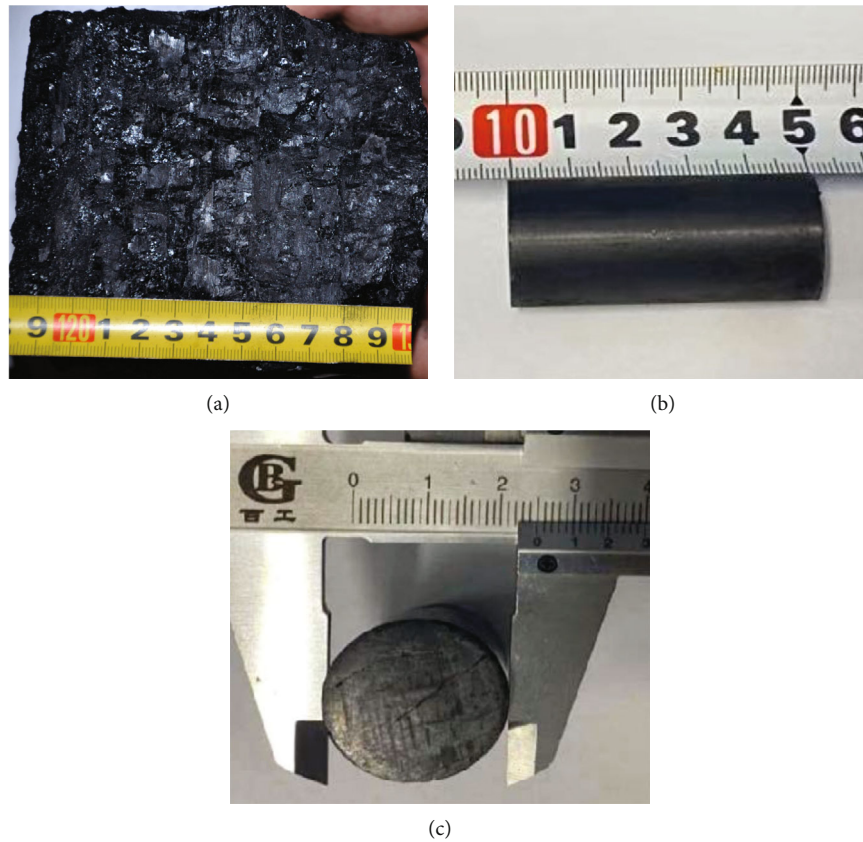


FIGURE 1: Experimental sample diagram: (a) raw coal sample, (b) front view columnar coal sample, and (c) sectional view of columnar coal sample.

pressures and injection times. The results show that the displacement of CH_4 by N_2 results from the joint action of multiple mechanisms. It can be seen from Figure 4 that the whole process can be divided into three stages (taking the injection pressure of 1.0 MPa as an example). Stage I (original equilibrium stage): the volume fraction of N_2 was 0, and the volume fraction of CH_4 was 100%. At first, N_2 was injected into the coal samples saturated with CH_4 . The migration speed of N_2 through “seepage-diffusion-adsorption” under the pressure gradient is relatively slow. It takes a specific time to break the original equilibrium state. Stage II (dynamic balance stage): N_2 had seeped from fractures with continuous gas injection. Then, N_2 diffused into the pores of the coal matrix, and the concentration of N_2 began to increase while the concentration of CH_4 decreased. There was a dynamic change relationship of “this and the other.” This is because the partial pressure of CH_4 decreased, and CH_4 is desorbed from the coal matrix after N_2 injection. In addition, the concentration difference between macropores and micropores will be increased with the migration of free CH_4 in fractures. Thus, the CH_4 desorption was accelerated. In this stage, CH_4 desorbed from the coal matrix and diffused to the fractures under the concentration gradient. Stage III (new equilibrium stage): the concentration of N_2 increased to 100%, while the concentration of CH_4 decreased to 0 with continuous N_2 injection. The new equilibrium state was established, and the CH_4 was no longer desorbed.

3.2. *The Concentration Change of the Output Gas.* It can be seen from Figures 5 and 6 that the concentrations of CH_4 and N_2 present an opposite variation trend, and the variation rate of CH_4 and N_2 increased first and then decreased. The results showed that the CH_4 concentration was 100% while the N_2 concentration was 0 in stage I. The duration of stage I was 50 minutes, 35 minutes, 25 minutes, 15 minutes, and 10 minutes, respectively, at the level of 0.5 MPa, 1 MPa, 1.5 MPa, 2 MPa, and 2.5 MPa. This indicated that the N_2 had not broken through the coal samples at this stage. Then, the CH_4 concentration gradually decreased. But the decrease rate of CH_4 concentration decreased in the 85th minute, 70th minute, 50th minute, 35th minute, and 25th minute, respectively, at the level of 0.5 MPa, 1 MPa, 1.5 MPa, 2 MPa, and 2.5 MPa. Finally, the CH_4 concentration decreased to less than 5% in the 100th minute, 80th minute, 60th minute, 40th minute, and 30th minute, respectively, at the level of 0.5 MPa, 1 MPa, 1.5 MPa, 2 MPa, and 2.5 MPa.

3.3. *Breakthrough Time and Displacement Time.* Breakthrough time refers to the time that the N_2 passes through the coal samples. The breakthrough time was an important index to evaluate the effect of CH_4 displacement by N_2 . The seepage and diffusion of N_2 in the coal samples depended on the pressure gradient and concentration gradient. Due to the slow diffusion rate, the injection pressure played a crucial role in this process. At the initial stage of

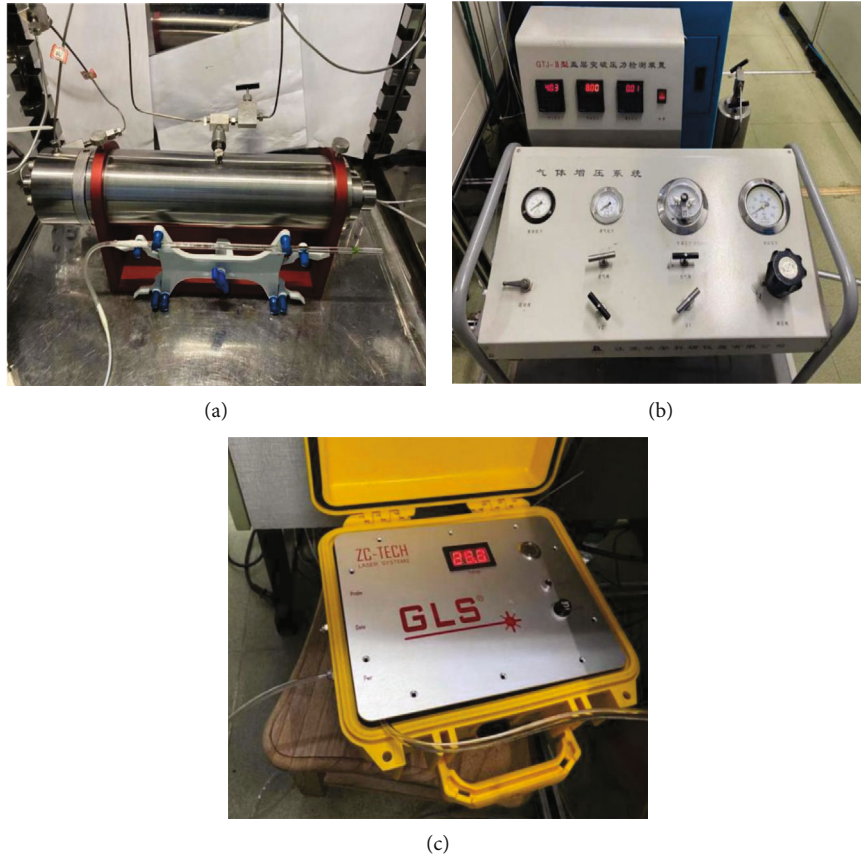


FIGURE 2: Diagram of main experimental equipment: (a) core holder, (b) pressurization system, and (c) gas component detector.

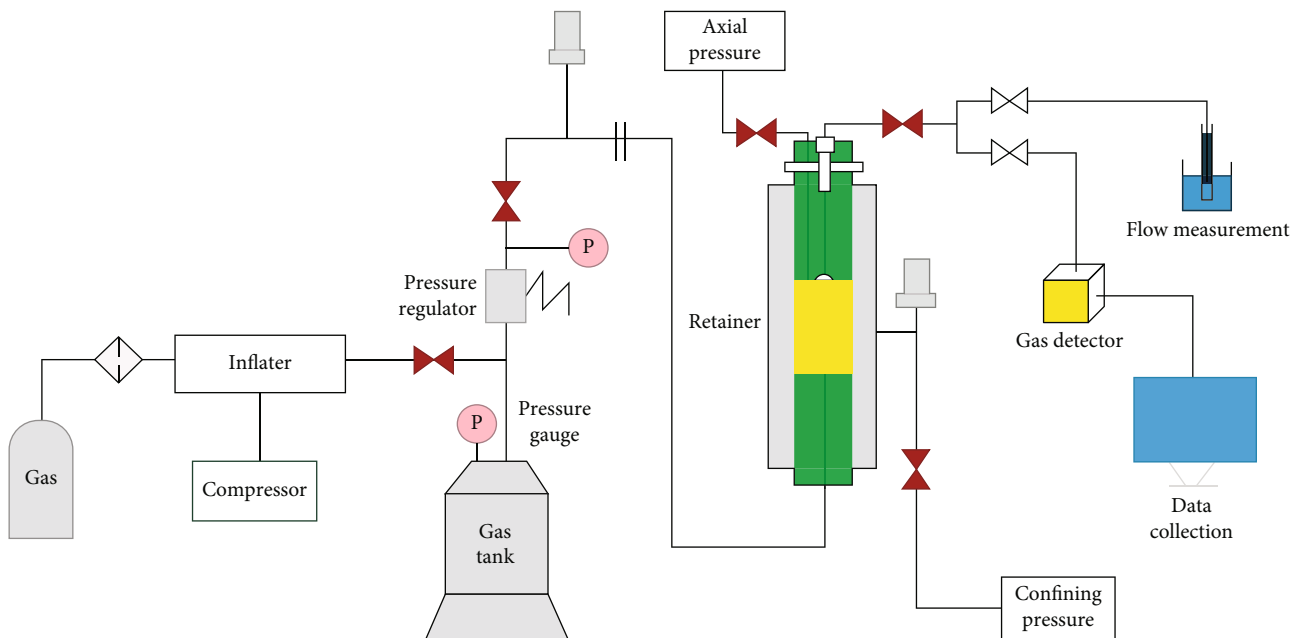


FIGURE 3: Flow chart of the experimental device.

N_2 injection, the N_2 will remain in the coal samples and cannot be detected at the outlet. It can be seen from Figure 7 that the breakthrough time was 50 minutes, 45 minutes, 35 minutes, 25 minutes, and 20 minutes, respectively, at the

level of 0.5 MPa, 1 MPa, 1.5 MPa, 2 MPa, and 2.5 MPa. In this process, the breakthrough time decreased by 10%, 30%, 50%, and 60%, respectively, with the increase in injection pressure. It can be concluded that the breakthrough

TABLE 1: Experimental parameters of CH₄ displacement by N₂.

Code	Displacement pressure (MPa)	Sample size (mm)	CH ₄ adsorption pressure (MPa)	Confining pressure (MPa)	Axial pressure (MPa)	Temperature (°C)					
1	0.5	25 × 50	1	4	2	20					
2	1	25 × 50	1	4	2	20					
3	1.5	25 × 50	1	4	2	20					
4	2	25 × 50	1	4 </tr <tr> <td>5</td> <td>2.5</td> <td>25 × 50</td> <td>1</td> <td>4</td> <td>2</td> <td>20</td> </tr>	5	2.5	25 × 50	1	4	2	20
5	2.5	25 × 50	1	4	2	20					

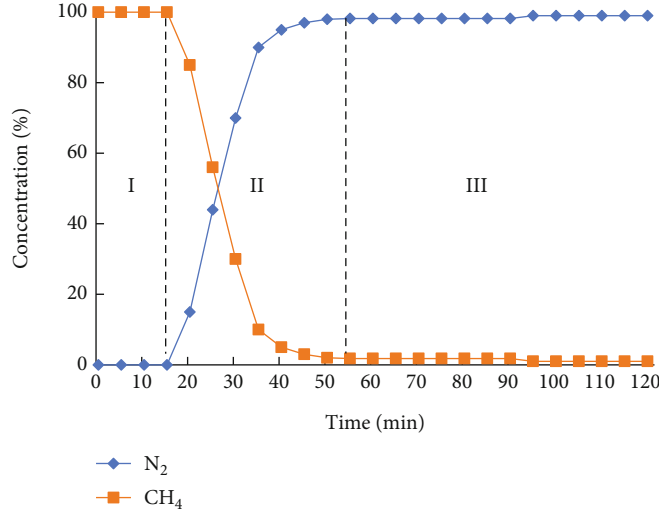


FIGURE 4: Variation of concentration with gas injection time.

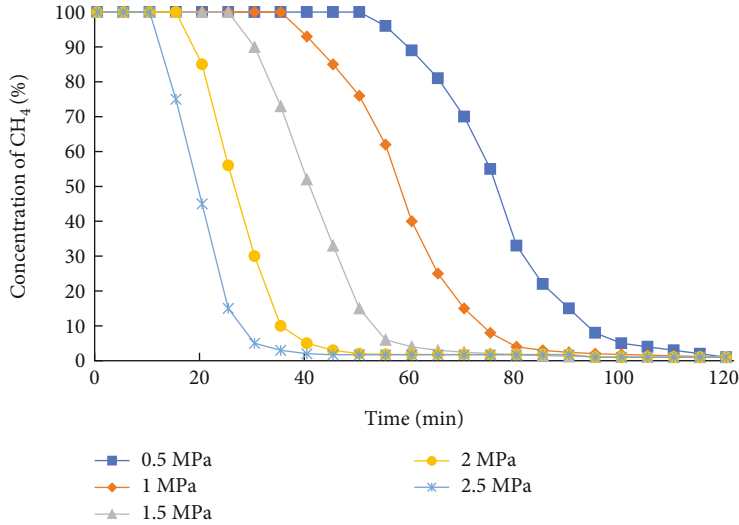


FIGURE 5: Variation of CH₄ concentration under different pressures.

time was gradually shortened and the change rate decreased with the increase of injection pressure. At this stage, the N₂ would diffuse into the micropores and occupy the adsorption vacancy in the coal surface. At this time, the seepage process was not dominant. Then, the seepage velocity of N₂ in the fractures increased with the increase of N₂ injection

pressure. Thus, the seepage velocity was faster than the diffusion velocity result in that the seepage process was dominant. Therefore, the N₂ would pass through the coal samples rapidly.

Displacement time refers to the time that the concentration of CH₄ decreased from 100% to a particular value in the

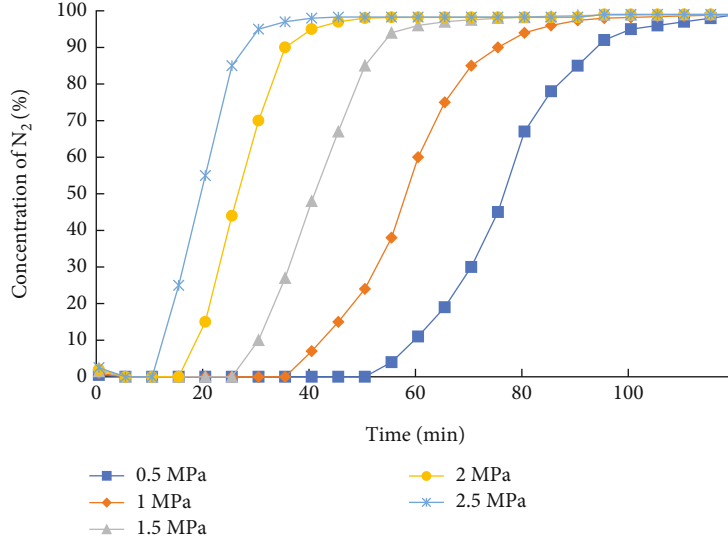


FIGURE 6: Variation of N_2 concentration under different pressures.

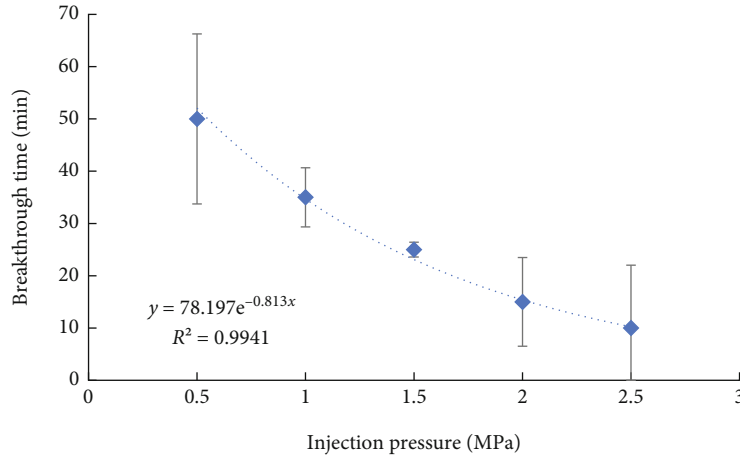


FIGURE 7: Breakthrough time under different pressures.

injection process. It can be seen from Figure 8 that the displacement time was 5 minutes at the level of 2.5 MPa, while the displacement time was 35 minutes at the level of 0.5 MPa. This indicated that the higher the injection pressure, the faster the variation of the CH_4 concentration. The results showed that the pressure gradient between the inlet and the outlet of the coal sample increased with the increase of injection pressure. Thus, the gas was easier to migrate. On the other hand, the high pore pressure offsets part of the effective stress, which reduced the pressure on the coal skeleton. Then, the porosity increased. Thus, the permeability of the coal sample was increased so that the gas migration velocity was accelerated.

3.4. Displacement Efficiency and Replacement Ratio. According to the total mixed flow q of CH_4 and N_2 measured under different injection pressures and different gas volume fractions (φ_{CO_2} , φ_{CH_4}), the output of CH_4 and N_2 can be calculated. Finally, the displacement efficiency η and replacement

ratio μ under different pressure conditions are obtained. The calculation formula is as follows:

$$\eta = \frac{Q_{CH_4}}{Q_{CH_4}^T} \times 100\% = \frac{\int_0^t \varphi_{CH_4} q dt}{Q_{CH_4}^T} \times 100\%, \quad (1)$$

$$\mu = \frac{Q_{N_2}^T}{Q_{CH_4}} \times 100\% = \frac{Q_{N_2}^T}{\int_0^t \varphi_{CH_4} q dt}$$

where η is the efficiency of N_2 displacing CH_4 (%); Q_{CH_4} is CH_4 output (mL); $Q_{CH_4}^T$ is the total injection amount of CH_4 (mL); φ_{CH_4} is the CH_4 concentration (%); q is the total flow of mixed gas (mL); μ is the replacement ratio (dimensionless); $Q_{N_2}^T$ is the total injected amount of N_2 (mL); t is time (min).

According to the experimental results, the η was 52.3%, 55.9%, 62.9%, 79.9%, and 85.2%, respectively, under different injection pressures. With increase in pressure, the η

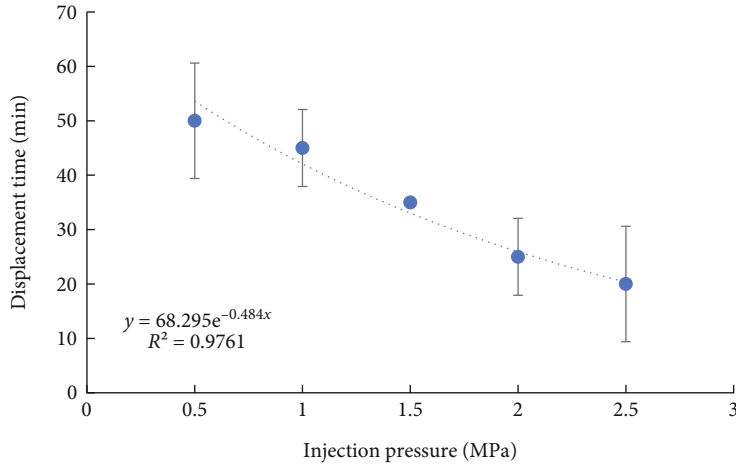


FIGURE 8: Displacement time under different pressures.

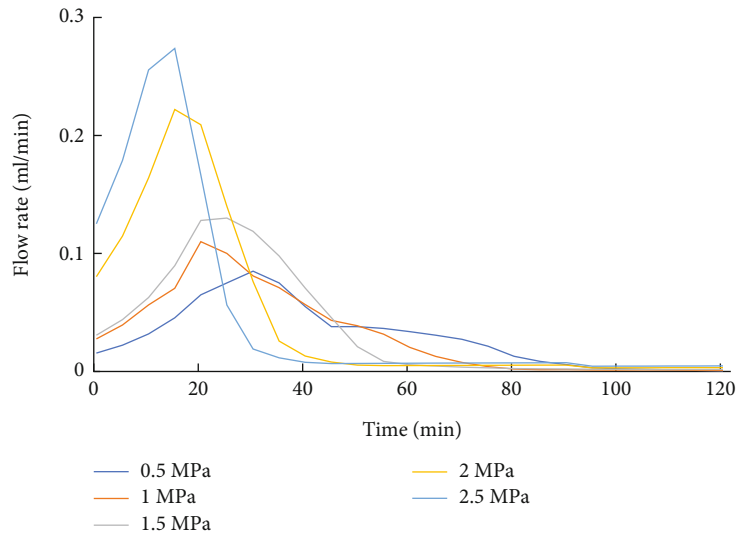


FIGURE 9: The flow rate of CH₄ under different injection pressures.

increased by 6.8%, 20.2%, 52.7%, and 62.9%, respectively. The μ in different pressures was 10.9, 10.2, 9.1, 7.2, and 6.7, respectively. With increase in pressure, the μ decreased by 6.4%, 16.5%, 33.9%, and 38.5%, respectively. It can be concluded that η increased with the increase of injection pressure. And the greater the pressure, the more significant the η increased. The maximum increase was more than 60%. The μ decreased with increase in pressure. The maximum decrease of μ was more than 38%.

3.5. Flow Rate of CH₄ and Accumulated Production of CH₄. It can be seen from Figure 9 that the maximum flow rate of CH₄ was 0.085 mL/min, 0.110 mL/min, 0.130 mL/min, 0.222 mL/min, and 0.273 mL/min, respectively, at the level of 0.5 MPa, 1 MPa, 1.5 MPa, 2 MPa, and 2.5 MPa. The regression curve appeared wave top under different injection pressures. The greater the injection pressure, the sharper the waveform. While the less the injection pres-

sure, the wider the waveform. According to the experimental results, the flow rate of CH₄ decreased after an initial increase under different injection pressures. The peak value of the flow rate of CH₄ increased with the injection pressure. But the flow rate of CH₄ decreased rapidly at the pressure above 1.5 MPa. This indicated that the N₂ flowed easily in pores and fractures with high injection pressure so that the breakthrough time decreased. But the N₂ do not remain in the coal matrix at high injection pressure. Therefore, the coal matrix cannot effectively adsorb N₂ at a pressure above 1.5 MPa, which results in a large amount of CH₄ remaining in the coal.

It can be seen from Figure 10 that the accumulated production of CH₄ was 3.59 mL, 3.91 mL, 4.39 mL, 5.58 mL, and 5.94 mL, respectively, at the level of 0.5 MPa, 1 MPa, 1.5 MPa, 2 MPa, and 2.5 MPa. The results showed that the accumulated production of CH₄ increased with the increase in injection pressure. However, the increase of accumulated

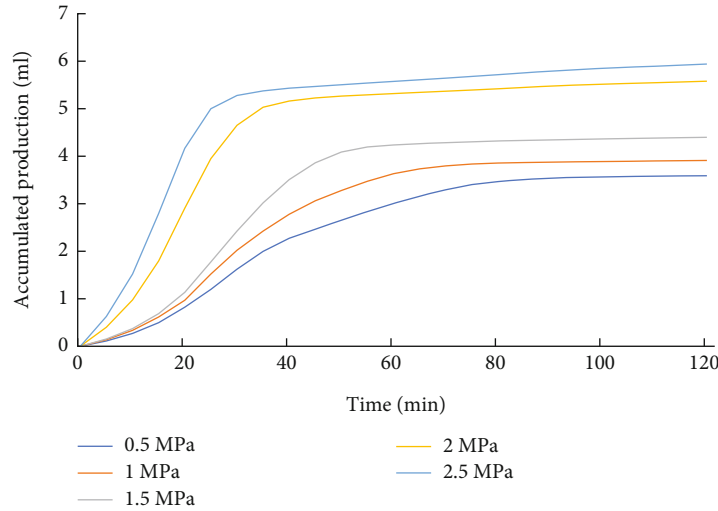


FIGURE 10: Accumulated CH_4 production under different pressures.

TABLE 2: Data standardization results under different pressures.

Code	Injection pressure (MPa)	Displacement efficiency (%)	Standardized processing	Replacement ratio	Standardized processing
1	0.5	52.3	0	10.9	1
2	1	55.9	0.89	10.2	0.16
3	1.5	62.9	0.32	9.1	0.57
4	2	79.9	0.16	7.2	0.88
5	2.5	85.2	1	6.7	0

production of CH_4 decreased at the injection pressure above 2 MPa. This indicated that the amount of CH_4 displaced by N_2 increased with the increase of injection pressure. The increase of injection pressure will increase the permeability of the coal so that it is easier for the gas to migrate in the seepage channel. It can be concluded that at the beginning, N_2 diffused from fractures to micropores, and competitive adsorption occurred. A large amount of CH_4 had been replaced due to a decrease of the partial pressure of CH_4 . After reaching the critical time, CH_4 desorption and N_2 adsorption reached dynamic equilibrium. Therefore, the production of CH_4 will no longer increase. According to the displacement efficiency, the injection pressure can be divided into three stages. At the range of 0.5~1 MPa, it was the low-efficiency stage, and the displacement efficiency was about 50%; at the range of 1~2 MPa, it was the medium efficiency stage, and the displacement efficiency was about 60%; at the range of 2~2.5 MPa, it was the high-efficiency stage, and the displacement efficiency was 70~85%.

3.6. N_2 Injection Pressure. In the experiment, the displacement efficiency and replacement ratio were obtained according to different evaluation indicators. The two parameters cannot be directly compared and analyzed. In order to eliminate the impact of the difference in the dimension and value range among the indicators, it was necessary to carry out a standardization process and scale the parameters according to the proportion. The minimum-maximum normalization of the parameters, also known as discrete normalization,

maps the parameter's value to (0, 1) according to the linear transformation of the original data according to formula (2). The data processing results are shown in Table 2.

$$A_z = \frac{A - \min}{\max - \min}. \quad (2)$$

It can be seen from Figure 11 that there is a crossover point between the displacement efficiency and replacement ratio with different injection pressures after the discrete standardization treatment of the two parameters. The injection pressure corresponding to the crossover point was 1.6 MPa, and the displacement efficiency was 45%. Theoretically, the injection pressure corresponding to the crossover point was the most economical. The displacement efficiency increased with the increase of the injection pressures, while the replacement ratio decreased with the increase of the injection pressures. Figure 11 shows that the displacement efficiency was low while the replacement ratio is relatively high at the range of 0.5~1.6 MPa. This indicated that the amount of N_2 required for the displacement of CH_4 per unit volume was large. This pressure range was not ideal from a technical and economic perspective. At the range of 1.6~2 MPa, the displacement efficiency was high, but the replacement ratio is gradually reduced. This indicated that the amount of N_2 required for the displacement of unit volume of CH_4 was low. At injection pressure above 2 MPa, the increase rate of displacement efficiency was low, and the decrease rate of displacement ratio was reduced. This

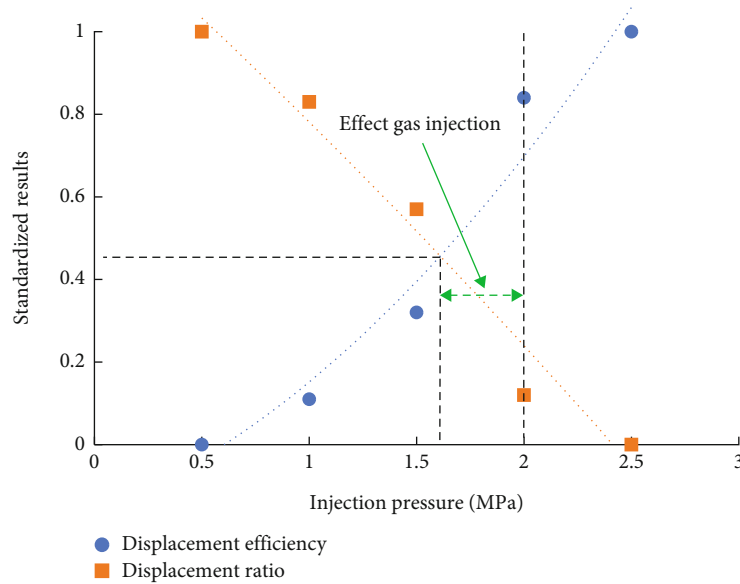


FIGURE 11: Displacement efficiency and displacement ratio under different pressures.

indicated that the flow velocity of N_2 and free CH_4 increased with the increase of injection pressure. At the same time, the displacement efficiency increased with the increase of injection pressure. Therefore, more N_2 enters into the tiny pores of the coal matrix so that more adsorbed CH_4 was displaced in the pores. The larger the amount of CH_4 displaced, the smaller the replacement ratio. When the injection pressure is greater than 2 MPa, the change rate of displacement efficiency and replacement ratio decreases with the increase of injection pressure, which shows that the influence of injection pressure on displacement efficiency and replacement ratio is weakened.

4. Discussion

The displacement of CH_4 by N_2 is a dynamic process. Most of the researchers [17, 23, 32] divide the process into three stages. This is also verified by our experimental results. According to our experimental results, the variation rate of the concentration of CH_4 showed a trend of increase before decrease. It was believed that the free CH_4 in the coal samples would be driven away to the outlet first after N_2 was injected into the coal samples. When the concentration of CH_4 in the fractures and macropores decreased, the desorbed CH_4 in the coal surface increased. Then, a large number of empty adsorption sites would be left [8, 17]. The N_2 would diffuse into the coal surface with the increase of injection [13]. Thus, the N_2 molecules would collide with the empty adsorption sites which had not yet adsorbed CH_4 molecules [27]. Then, the N_2 molecules would occupy the empty adsorption sites. In addition, the partial pressure of CH_4 decreased with the injection of N_2 . The partial pressure of CH_4 would promote the desorption of CH_4 , which provides more adsorption sites for N_2 [43]. However, the adsorption of N_2 molecules on the coal surface was weak. The coal surface cannot absorb N_2 molecules anymore with continuous injection. Then, the injected N_2 would migrate

directly to the outlet of the coal samples. At the inception of stage II, the concentration of CH_4 produced increased rapidly because there was a large amount of free CH_4 in the fractures. Then, both of the free CH_4 and adsorbable CH_4 in the coal samples were decreased. Thus, the rate of decrease of CH_4 concentration was increased first and then decreased.

Gas extraction undergoes a desorption-diffusion-seepage process [44]. The transport of N_2 and CH_4 after N_2 injection into coal seams is an interactive process. After the injection of N_2 , the injected gas occupies a certain space and bears part of the pore pressure. The number of adsorption sites in coal is fixed. The number of adsorption sites occupied by the injected gas increases which results to the decrease of CH_4 -occupied adsorption sites [43]. This means that the increased partial pressure after N_2 injection can promote the desorption of CH_4 . In addition, after gas injection, the reservoir pressure increases while the effective stress decreases. Thus, the permeability of the coal increases, which is conducive to the transport of CH_4 [42]. These two points indicate that the higher the injection pressure, the more methane is produced. However, the results of Figure 10 show that when the injection pressure is increased to a certain level, the methane output increases insignificantly. We believe that the bidirectional diffusion processes of gases influence the output of methane. The flow rate of the injected gas increases as the injection pressure increases. When the flow rate of injection gas is too fast, the injected gas cannot diffuse sufficiently into the coal matrix, resulting in reduced methane production. Thus, there is a specific pressure range which is beneficial to the production of methane.

5. Conclusion

- (1) The whole process of CH_4 displacement by N_2 is a dynamic process. It can be divided into three stages:

stage I (original equilibrium stage); stage II (dynamic balance stage); stage III (new equilibrium stage). The concentration of CH₄ and N₂ presented an opposite variation trend, and the variation rate of CH₄ and N₂ increased first and then decreased

- (2) Both of the breakthrough time and displacement time were negatively correlated with the injection pressures. The maximum flow rates of CH₄ increased with the increased injection pressures. But the attenuating tendency of flow rates of CH₄ was obvious with the increased injection pressures. The accumulated production of CH₄ increased with the increased injection pressures
- (3) The displacement efficiency increased with the increased injection pressures while the replacement ratio decreased with the increased injection pressures. The effective injection pressure range for the test samples was 1.6~2 MPa from a technical and economic perspective

Data Availability

The data used to support the findings of this study are available from the corresponding author upon request.

Conflicts of Interest

The authors declare no conflict of interest.

Authors' Contributions

Z.A. and S.L. were responsible for the conceptualization. S.X. was responsible for the methodology. Z.A. was responsible for the formal analysis. Z.A. was responsible for the resources. Z.A. was responsible for the writing—original draft preparation. S.L. was responsible for the writing—review and editing. S.L. was responsible for the visualization. H.Z. was responsible for the supervision. S.L. was responsible for the project administration. All authors have read and agreed to the published version of the manuscript.

Acknowledgments

This research was funded by the National Natural Science Foundation of China (No. 51974161).

References

- [1] Y. Qin, T. A. Moore, J. Shen, Z. Yang, Y. Shen, and G. Wang, "Resources and geology of coalbed methane in China: a review," *International Geology Review*, vol. 60, pp. 777–812, 2018.
- [2] Y. Cao, D. He, and D. C. Glick, "Coal and gas outbursts in footwalls of reverse faults," *International Journal of Coal Geology*, vol. 48, no. 1-2, pp. 47–63, 2001.
- [3] M. Qian, J. Xu, and X. Miao, "Gully-specific debris flow hazard assessment in China," *Journal of China University of Mining and Technology*, vol. 13, no. 2, pp. 112–118, 2003.
- [4] C. Wu, C. Yuan, G. Wen, L. Han, and H. Liu, "A dynamic evaluation technique for assessing gas output from coal seams during commingling production within a coalbed methane well: a case study from the Qinshui Basin," *International Journal of Coal Science & Technology*, vol. 7, no. 1, pp. 122–132, 2020.
- [5] Q. Zou, H. Liu, Z. Cheng, T. Zhang, and B. Lin, "Effect of slot inclination angle and borehole-slot ratio on mechanical property of pre-cracked coal: implications for ECBM recovery using hydraulic slotting," *Natural Resources Research*, vol. 29, pp. 1705–1729, 2020.
- [6] L. Zhang, S. Lu, C. Zhang, and S. Chen, "Effect of cyclic hot/cold shock treatment on the permeability characteristics of bituminous coal under different temperature gradients," *Journal of Natural Gas Science and Engineering*, vol. 75, p. 103121, 2020.
- [7] C. Fan, M. Luo, S. Li, H. Zhang, Z. Yang, and Z. Liu, "A thermo-hydro-mechanical-chemical coupling model and its application in acid fracturing enhanced coalbed methane recovery simulation," *Energies*, vol. 12, no. 4, p. 626, 2019.
- [8] L. Zhang, S. Chen, C. Zhang, X. Fang, and S. Li, "The characterization of bituminous coal microstructure and permeability by liquid nitrogen fracturing based on CT technology," *Fuel*, vol. 262, article 116635, 2020.
- [9] M. Lu and L. D. Connell, "Coal seam failure during primary/enhanced gas production: how failure develops in fields," *International Journal of Coal Geology*, vol. 221, p. 103432, 2020.
- [10] C. Fan, S. Li, D. Elsworth, J. Han, and Z. Yang, "Experimental investigation on dynamic strength and energy dissipation characteristics of gas outburst-prone coal," *Energy Science & Engineering*, vol. 8, no. 4, pp. 1015–1028, 2020.
- [11] Z. Liu, Y. Cheng, Y. Wang, L. Wang, and W. Li, "Experimental investigation of CO₂ injection into coal seam reservoir at in-situ stress conditions for enhanced coalbed methane recovery," *Fuel*, vol. 236, pp. 709–716, 2019.
- [12] B. Brattækås and M. Haugen, "Explicit tracking of CO₂-flow at the core scale using micro-positron emission tomography (μ PET)," *Journal of Natural Gas Science and Engineering*, vol. 77, p. 103268, 2020.
- [13] N. Fan, J. Wang, C. Deng, Y. Fan, Y. Mu, and T. Wang, "Numerical study on enhancing coalbed methane recovery by injecting N₂/CO₂ mixtures and its geological significance," *Energy Science & Engineering*, vol. 8, no. 4, pp. 1104–1119, 2020.
- [14] M. Asif, M. Pillalamarri, D. C. Panigrahi, P. Naveen, and K. Ojha, "Measurement of coalbed gas content of Indian coalfields: a statistical approach," *International Journal of Oil, Gas and Coal Technology*, vol. 25, no. 1, pp. 73–88, 2020.
- [15] R. Wang, Q. Wang, Q. Niu, J. Pan, H. Wang, and Z. Wang, "CO₂ adsorption and swelling of coal under constrained conditions and their stage-change relationship," *Journal of Natural Gas Science and Engineering*, vol. 76, p. 103205, 2020.
- [16] C. R. Clarkson, A. Vahedian, A. Ghanizadeh, and C. Song, "A new low-permeability reservoir core analysis method based on rate-transient analysis theory," *Fuel*, vol. 235, pp. 1530–1543, 2019.
- [17] X. Zhang and P. G. Ranjith, "Experimental investigation of effects of CO₂ injection on enhanced methane recovery in coal seam reservoirs," *Journal of CO₂ Utilization*, vol. 33, pp. 394–404, 2019.
- [18] A. S. Ranathunga, M. S. A. Perera, P. G. Ranjith, and C. Wei, "An experimental investigation of applicability of CO₂ enhanced coal bed methane recovery to low rank coal," *Fuel*, vol. 189, pp. 391–399, 2017.

- [19] S. Liu, C. Zhu, B. Lin, and T. Liu, "The effect of spatial distribution mode of hydraulic slotting on pressure relief and permeability enhancement of the coal seam," *Journal of Mining and Safety Engineering*, vol. 37, pp. 983–990, 2020.
- [20] Y. Yang, Q. Xu, X. Li et al., "Pore-scale simulation of gas-water two-phase flow in volcanic gas reservoir based on volume of fluid method," *Journal of Natural Gas Science and Engineering*, vol. 106, p. 104733, 2022.
- [21] S. Zhu and A. Salmachi, "Flowing material balance and rate-transient analysis of horizontal wells in under-saturated coal seam gas reservoirs: a case study from the Qinshui Basin, China," *Energies*, vol. 14, no. 16, p. 4887, 2021.
- [22] S. Chen, J. Zhang, D. Yin, X. Cheng, and N. Jiang, "Relative permeability measurement of coal microchannels using advanced microchip technology," *Fuel*, vol. 312, article 122633, 2022.
- [23] H. Wang, Q. Ran, X. Liao, X. Zhao, M. Xu, and P. Fang, "Study of the CO₂ ECBM and sequestration in coalbed methane reservoirs with SRV," *Journal of Natural Gas Science and Engineering*, vol. 33, pp. 678–686, 2016.
- [24] X. Liu, C. Liu, and G. Liu, "Dynamic behavior of coalbed methane flow along the annulus of single-phase production," *International Journal of Coal Science & Technology*, vol. 6, no. 4, pp. 547–555, 2019.
- [25] L. Zhang, Z. Ye, M. Li, C. Zhang, Q. Bai, and C. Wang, "The binary gas sorption in the bituminous coal of the Huaibei coalfield in China," *Adsorption Science and Technology*, vol. 36, pp. 1612–1628, 2018.
- [26] D. J. Black, "Review of current method to determine outburst threshold limits in Australian underground coal mines," *International Journal of Mining Science and Technology*, vol. 29, no. 6, pp. 859–865, 2019.
- [27] S. N. Longinos, L. Wang, and R. Hazlett, "Advances in cryogenic fracturing of coalbed methane reservoirs with LN₂," *Energies*, vol. 15, no. 24, p. 9464, 2022.
- [28] S. N. Longinos, A. Serik, D. Zhang, L. Wang, and R. Hazlett, "Experimental evaluation of liquid nitrogen fracturing on the coal rocks in Karaganda Basin, Kazakhstan," *Arabian Journal for Science and Engineering*, pp. 1–16, 2023.
- [29] S. N. Longinos, A. Dillinger, L. Wang, and R. Hazlett, "Uniaxial compressive strength (UCS) and SEM study of liquid nitrogen for waterless hydraulic fracturing in coalbed methane reservoirs of Karaganda Basin in Kazakhstan," *Gas Science and Engineering*, vol. 115, article 204998, 2023.
- [30] Y. Wu, J. Liu, Z. Chen, D. Elsworth, and D. Pone, "A dual poroelastic model for CO₂-enhanced coalbed methane recovery," *International Journal of Coal Geology*, vol. 86, pp. 177–189, 2011.
- [31] H. Kumar, D. Elsworth, J. P. Mathews, J. Liu, and D. Pone, "Effect of CO₂ injection on heterogeneously permeable coalbed reservoirs," *Fuel*, vol. 135, pp. 509–521, 2014.
- [32] E. Ozdemir, "Modeling of coal bed methane (CBM) production and CO₂ sequestration in coal seams," *International Journal of Coal Geology*, vol. 77, no. 1-2, pp. 145–152, 2009.
- [33] X. Huang, L. Zhang, R. Zhang, X. Chen, Y. Zhao, and S. Yuan, "Numerical simulation of gas-liquid two-phase flow in the micro-fracture networks in fractured reservoirs," *Journal of Natural Gas Science and Engineering*, vol. 94, article 104101, 2021.
- [34] C. J. Seto, K. Jessen, and F. M. Orr, "A four-component two-phase flow model for CO₂ storage and enhanced coalbed methane recovery," in *Paper presented at the SPE Annual Technical Conference and Exhibition*, San Antonio, Texas, USA, 2006.
- [35] T. Xia, F. Zhou, J. Liu, S. Hu, and Y. Liu, "A fully coupled coal deformation and compositional flow model for the control of the pre-mining coal seam gas extraction," *International Journal of Rock Mechanics and Mining Sciences*, vol. 72, pp. 138–148, 2014.
- [36] S. R. Reeves, D. W. Davis, and A. Y. Oudinot, "A technical and economic sensitivity study of enhanced coalbed methane recovery and carbon sequestration in coal," *Doe Topical Report*, vol. 65, pp. 58–60, 2013.
- [37] W. D. Gunter, M. J. Mavor, and J. R. Robinson, "CO₂ storage and enhanced methane production: field testing at Fenn-Big Valley, Alberta, Canada, with application," *Greenhouse Gas Control Technologies*, vol. I, pp. 413–421, 2005.
- [38] W. Z. Zhao, X. B. Su, D. P. Xia, S. H. Hou, Q. Wang, and Y. X. Zhou, "Enhanced coalbed methane recovery by the modification of coal reservoir under the supercritical CO₂ extraction and anaerobic digestion," *Energy*, vol. 259, article 124914, 2022.
- [39] J. Shi, S. Durucan, and M. Fujioka, "A reservoir simulation study of CO₂ injection and N₂ flooding at the Ishikari coalfield CO₂ storage pilot project, Japan," *International Journal of Greenhouse Gas Control*, vol. 2, no. 1, pp. 47–57, 2008.
- [40] S. Yamaguchi, K. Ohga, M. Fujioka, and M. Nako, "Field test and history matching of the CO₂ sequestration project in coal seams in Japan," *International Journal of the Society of Materials Engineering for Resources*, vol. 13, no. 2, pp. 64–69, 2006.
- [41] S. Cho, S. Kim, and J. Kim, "Life-cycle energy, cost, and CO₂ emission of CO₂-enhanced coalbed methane (ECBM) recovery framework," *Journal of Natural Gas Science and Engineering*, vol. 70, article 102953, 2019.
- [42] S. Harpalani and A. Mitra, "Impact of CO₂ injection on flow behavior of coalbed methane reservoirs," *Transport in Porous Media*, vol. 82, no. 1, pp. 141–156, 2010.
- [43] X. Du, D. Pang, Y. Cheng et al., "Adsorption of CH₄, N₂, CO₂, and their mixture on montmorillonite with implications for enhanced hydrocarbon extraction by gas injection," *Applied Clay Science*, vol. 210, article 106160, 2021.
- [44] P. Ji, Y. Guo, L. Zhang, X. Kong, X. Wang, and Y. Zhou, "Research on gas pre-draining in coal roadway strips by combined ordinary drilling and directional drilling," *Industrial and Mining Automation*, vol. 47, pp. 61–66, 2021.

Research Article

Influence of Water Saturation on Adsorption Behavior at Liquid-Liquid Interfaces in Unsaturated Porous Media

Yan Zhu ¹, Ziteng Cui ², Kun Li,³ Chaoqi Wang ¹, Zhao Li ¹, Xueyi Zhang ¹,
and Zhi Dou ¹

¹School of Earth Sciences and Engineering, Hohai University, Nanjing 210098, China

²China Water Investment Co., LTD., Beijing 100053, China

³Shandong Water Transfer Project Operation and Maintenance Center, Jinan 250000, China

Correspondence should be addressed to Zhao Li; lizhao1990@hhu.edu.cn and Zhi Dou; dz.uriah@gmail.com

Received 21 July 2023; Revised 6 September 2023; Accepted 12 October 2023; Published 9 November 2023

Academic Editor: Bao Jia

Copyright © 2023 Yan Zhu et al. This is an open access article distributed under the Creative Commons Attribution License, which permits unrestricted use, distribution, and reproduction in any medium, provided the original work is properly cited.

Adsorption reaction in unsaturated porous media is of great importance for soil and groundwater remediation. In this study, the influence of the Peclet number (Pe) and water saturation on adsorption behavior at liquid-liquid interfaces was quantitatively investigated. The pore-scale reactive transport in unsaturated porous media was directly simulated. The Navier-Stokes equations, the surface transfer and adsorption reaction equations, and the advection-diffusion equation (ADE) were coupled to obtain the flow and concentration fields. The results showed that water saturation had a significant influence on the complexity of the flow field. A nonmonotonic relationship was found between water saturation and the uniformity of the flow field. Peclet number had little influence on the maximum adsorption. On the other hand, the adsorption time showed a nearly linear relationship with the Peclet number and increased with increasing Peclet number. Additionally, a nonlinear relationship was found between water saturation and the maximum adsorption. As water saturation increased, the maximum adsorption tended to increase to a peak and then decrease. The peak of the maximum adsorption occurred at $Pe = 5$, $S_w = 0.458$, and the shortest adsorption time was observed at $S_w = 0.902$. However, the difference in adsorption times for saturations of 0.458 and 0.698 was not significant and was only about 20 PV difference.

1. Introduction

Soil is an important resource for human survival and a site for various reactions in groundwater. Surface soils are mostly unsaturated porous media subject to natural influences. In recent years, it has become evident that uncontrolled use and immature environmental regulations have led to a variety of ecological and environmental problems. Pollutants such as organic matter, heavy metals, pesticides, and fertilizers led to long-term soil pollution. In addition, soil pollution caused significant pollution of groundwater due to adsorption reactions at the soil surface and hydrodynamic influences on the groundwater system [1–5]. Therefore, understanding and applying reactive solute transport in unsaturated porous media and their internal adsorption reactions are crucial for soil and groundwater remediation.

Solute transport in porous media has been widely studied [6–9]. As in previous studies, solute transport research focused on the macroscopic scale. Transport processes in porous media were studied by constructing unit bodies and using averaging parameters to make macroscopic generalizations about their relevant properties. Wu et al. [10] determined the topology of spatial structure between particles of agar bead-filled beds under water-saturated conditions using magnetic resonance imaging (MRI). Wang et al. [11] studied the influence of soil anisotropy on solute transport. Pore-scale studies have made significant progress in recent years due to advances in computer technology and the refinement of numerical simulation techniques. Current methods for determining microscopic pore structure in porous media include physical imaging techniques and numerical methods. Zhou and Xiao [12] proposed a method to reconstruct 3D

multiphase rock models using a combination of computerized tomography (CT) and multiple features to study simulated fracture formation and obtained better results compared to experimental data. Scanning electron microscope (SEM) is also widely used; Liu et al. [13] and Zhao et al. [14] produced gray-scale images to refine the microstructure and quantify the characteristic parameters of the pore structure. Luo et al. [15] combined process-driven three-dimensional (3D) digital rock modeling with fractal analysis to create a digital rock model of simulated sandstone. Zhao et al. [16] determined the porosity of residual granite beds under external loading by CT scanning and derived the microstructural evolution process. However, due to the economic and technical limitations of the physical imaging method, the numerical simulation method has been used more frequently.

Although considerable efforts have been made in the field of solute transport in recent years, many studies have addressed only partial aspects that have been covered, especially in reactive solute transport problems [17–21]. Unsaturated brucite [$\text{Mg}(\text{OH})_2$] bearing column experiments have been used to evaluate the influence of the change in reactive mineral surface area, water content, precipitation of hydrous Mg carbonate, and gas distribution on the reaction of brucite [$\text{Mg}(\text{OH})_2$] with CO_2 gas [22, 23]. The results confirmed that conventional geometric surface updating models do not adequately represent the observed reaction process during the carbonation of brucite. Raoof et al. [24] presented a pore network modeling tool capable of simulating fluid flow and reactive and adsorptive transport of multiple components under saturated and differentially saturated conditions. Jiménez-Martínez et al. [25] pointed out mechanisms by which the mixing of an invading fluid with the resident fluid is considerably enhanced as saturation decreases, and the effective reactivity is much greater than under saturated conditions. Mixing-driven reactions in porous media are ubiquitous, but predicting where and how fast the reactions occur has been a tremendous challenge due to the complex and nonuniform nature of porous media flows [26]. Dou et al. [27] developed a pore-level numerical simulation model to investigate the saturation dependence of mass transfer in unsaturated porous residual media and the influence of saturation topography on mass transfer. They discovered a nonmonotonic relationship between dispersivity and residual saturation. However, the reactive properties at the liquid-liquid interface are neglected. Especially for adsorption, Yue et al. [28] studied the adsorption and desorption of the herbicide atrazine on soils, which is dominated by surface adsorption at low concentrations and influenced by adsorption sites on the adsorption surface. According to Lyu et al. [29], the spherical structure and ultrahigh surface ratio of the extremely efficient catalyst were studied to make it more efficient and stable. Thus, interfacial adsorption is the key to soil remediation, and the research combining unsaturated porous media with interfacial adsorption will receive more attention.

In this study, the complex pore structure was reconstructed to simulate the reactive solute transport in unsaturated porous media considering adsorption reactions at the interfaces at the pore scale. An immiscible two-phase trans-

port (ITPT) model was used to construct the geometric model of the unsaturated porous media with different water saturations. The Navier-Stokes equation, the surface transfer and adsorption reaction equations, and the advection-diffusion equation (ADE) were coupled and applied to the geometric model using COMSOL Multiphysics. We investigated the influence of water saturation on the flow field and quantitatively evaluated the uniformity of the flow velocity distribution. The influence of the Peclet number and water saturation on adsorption behavior at liquid-liquid interfaces was analyzed.

2. Materials and Methods

2.1. Unsaturated Porous Media Generation. A series of regular circles with different radii were simulated as solid particles in the porous media. The microscopic pore structure of saturated porous media particles was generated using the method described by Dou et al., i.e., a single porous medium with target porosity is generated in a specific region [30]. It should be noted that the size of the solid particles must be appropriate. To this end, the radius of the particle size should not only be within the range where the mean particle size and the standard deviation of the particle size distribution were usually controlled but also followed a truncated log-normal distribution. In this study, the radius ranged from 0.3 mm to 0.9 mm and was randomly distributed in a size range of 41×18 mm. The coefficient of variation (COV) was equal to 0.25, and the porosity of the generated porous media was set to 0.42. Due to the random distribution of particles and heterogeneous radius sizes, the internal spatial structure of the porous media was complex. Therefore, the porous media were considered heterogeneous in this study.

Our numerical simulations were based on four porous medium topologies with different water saturations ($S_w = 0.458$, $S_w = 0.698$, $S_w = 0.902$, and $S_w = 1.000$). The topology was determined by an ITPT model consisting of immiscible two-phase flows at the pore scale of Dou et al. [27]. Transport at the immiscible boundary was tracked using the phase field method (PFM). Trichloroethylene (TCE) was assumed to be the nonwetting phase fluid, and water was injected as the wetting phase fluid. The porous medium was first saturated with TCE and then injected with water at three rates to displace the TCE. In the end, we obtained models with different water saturations. As shown in Figure 1, the solid grains were shown in white. The liquid in the nonwetting phase was shown in gray, the blue areas showed the flow paths, and the interface between gray and blue is the liquid-liquid interface, where the adsorption and desorption reaction occurred.

2.2. Fluid Flow and Adsorptive Transport Modeling. To solve the mass transfer problem in unsaturated porous media, it is necessary to couple the groundwater flow field with the mass transfer concentration field. The mathematical fields of the reactive adsorption process must also be coupled with the two aforementioned fields to account for the adsorption reaction of solutes with the internal residual non-wetting phase.

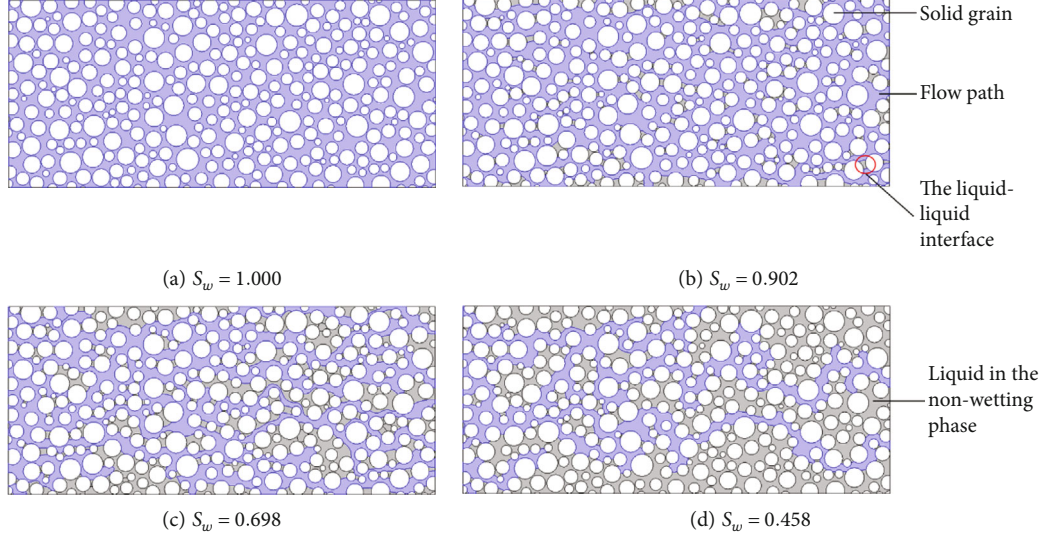


FIGURE 1: Topologies of porous media with different water saturations. The solid grains were shown in white. The liquid in the nonwetting phase was shown in gray, the blue areas showed the flow paths, and the interface between gray and blue is the liquid-liquid interface, where the adsorption and desorption reaction occurred.

To simulate water flow in unsaturated porous media, we used the Navier-Stokes equation as the control equation for water flow.

$$\begin{aligned} \rho g \nabla \varphi + \mu \nabla u &= 0, \\ \nabla \cdot u &= 0, \end{aligned} \quad (1)$$

where ρ [$\text{kg}\cdot\text{m}^3$] is the density of water, g [$\text{m}\cdot\text{s}^{-2}$] is the acceleration of gravity, and φ [m] represents the water head. $\mu = 1 \times 10^{-3} \text{ kg}\cdot(\text{m}\cdot\text{s})^{-1}$ is the dynamic viscosity coefficient of water, and u [$\text{m}\cdot\text{s}^{-1}$] is the velocity.

The adsorption/desorption reaction at the interface of unsaturated porous media can be described as



where the forward reaction rate is k_f , the reverse reaction rate is k_r , A is the molecular material in the solute, and A_s is the molecular material adsorbed on the surface.

In this study, adsorption in a single molecular layer was used for the reaction interface, and molecular forces between adsorbed molecules were neglected to account for adsorption at the interface during solute transport. According to the Langmuir hypothesis of adsorption in a single molecular layer, the adsorption capacity at all adsorbable interfaces was the same because the interface was homogeneous throughout. Therefore, the adsorption and desorption processes were in a dynamic equilibrium state during solute transport.

Assuming that θ is the percentage of the surface covered by adsorbed molecules, the percentage of the free zone is $1 - \theta$. According to Langmuir's theory of monolayer adsorption, the desorption rate of molecules, r_{des} ($\text{mol}/(\text{m}^2 \cdot \text{s})$), was proportional to θ and equal to $k_r \theta$, where k_r was constant at a

TABLE 1: Calculation parameter settings.

Symbols	Parameter name	Unit	Value
c_0	Initial concentration	mol/m^3	0.002
k_{ads}	Adsorption rate constants	$\text{m}^3/(\text{s}\cdot\text{mol})$	4.12
k_{des}	Desorption rate constant	1/s	2E-4
Γ_s	Active site concentration	mol/m^2	2E-6
D_s	Surface diffusivity	m^2/s	1E-11
D	Reactant diffusivity	m^2/s	1E-9

constant temperature. The adsorption rate of molecules was proportional to the percentage of free zone $1 - \theta$ and the rate at which the molecule collided with the surface. The collision rate was in turn proportional to the partial pressure of the substance P_A (Pa). The adsorption rate ($\text{mol}/(\text{m}^2\cdot\text{s})$) was therefore expressed as r_{ads} , which was equal to $k_f P_A (1 - \theta)$. The k_r was constant at a constant temperature.

To establish the equation by the concentrations, the following substitutions are made.

$$\theta = \frac{c_s}{\Gamma_s}, \quad (3)$$

$$P_A = cRT, \quad (4)$$

where we set the in-domain concentration of A to c [$\text{mol}\cdot\text{m}^{-3}$] and the surface concentration to c_s [$\text{mol}\cdot\text{m}^{-3}$]. $\Gamma_s = 2 \times 10^{-6} \text{ mol}\cdot\text{m}^{-2}$ is the total concentration of the surface that can be covered by the adsorbed molecules, R [$\text{J}\cdot(\text{mol}\cdot\text{K})^{-1}$] is the gas constant, and T [K] is the temperature.

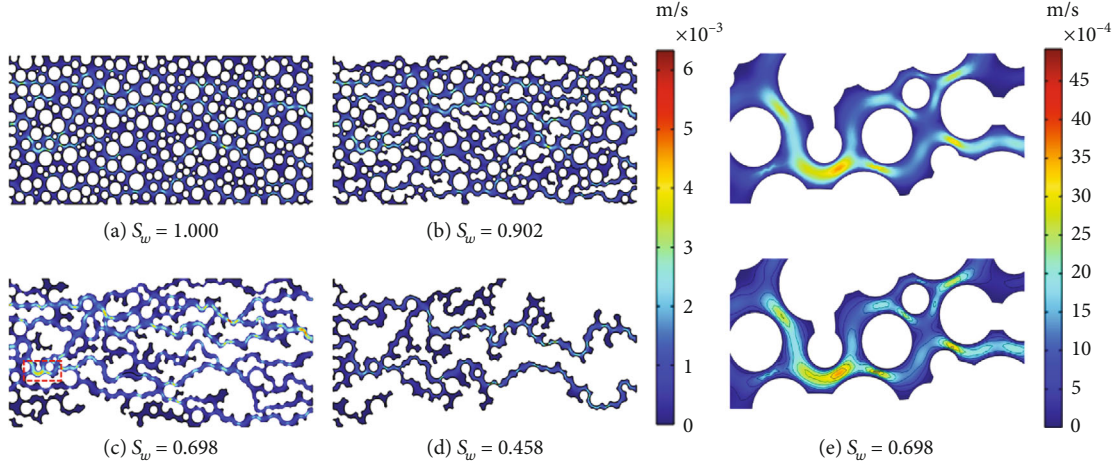


FIGURE 2: The flow fields in saturated (a) and unsaturated porous media (b–d) and the distribution of water flow (e).

Eq. (3) and Eq. (4) were used to derive the adsorption and desorption rates.

$$\gamma_{\text{des}} = k_{\text{des}} c_s, \quad (5)$$

$$\gamma_{\text{ads}} = k_{\text{ads}} c (\Gamma_s - c_s), \quad (6)$$

where the rate constant for the desorption reaction $k_{\text{des}} = 2 \times 10^{-4} \text{ s}^{-1}$ and the rate constant for the adsorption reaction $k_{\text{ads}} = 4.12 \text{ m}^3 \cdot (\text{mol} \cdot \text{s})^{-1}$.

This leads to the equations for surface transfer and adsorption.

$$\frac{\partial C_s}{\partial t} + \nabla \cdot (-D_s \nabla C_s) = k_{\text{ads}} c (\Gamma_s - c_s) - k_{\text{des}} c_s. \quad (7)$$

The nonuniform velocity field of groundwater flow in unsaturated porous media and the surface reaction rate can be derived from Eq. (5) and Eq. (6), which are inserted into ADE to obtain the following equation.

$$\frac{\partial c}{\partial t} + \nabla \cdot (-D \nabla c + cu) = 0, \quad (8)$$

where the surface diffusion coefficient $D_s = 1 \times 10^{-11} \text{ m}^2 \cdot \text{s}^{-1}$ and the reactant diffusivity $D = 1 \times 10^{-9} \text{ m}^2 \cdot \text{s}^{-1}$.

2.3. Numerical Modeling Strategy and Setup. COMSOL Multiphysics finite element software (COMSOL Inc., Burlington, MA, USA) was used to simulate water flow, solute transport, and adsorption at the interface using. The model was set up with a constant pressure outlet boundary on the right and a constant pressure inlet boundary on the left. The particle boundary and the upper and lower boundaries of the geometric model were set as slip-free boundaries. The slip-free boundary condition is a central part of the boundary conditions used in fluid dynamics. It assumes that the fluid in direct contact with a solid surface adheres to that surface and has the same velocity as the surface. In other words, the velocity of the fluid directly at the boundary is zero. The inclusion of the slip-free boundary condition greatly

TABLE 2: Velocity uniformity indexes.

Water saturation	CV	γ_v
$S_w = 1.000$	1.0193	0.5943
$S_w = 0.902$	0.9803	0.6037
$S_w = 0.698$	1.0921	0.5427
$S_w = 0.458$	1.1623	0.5138

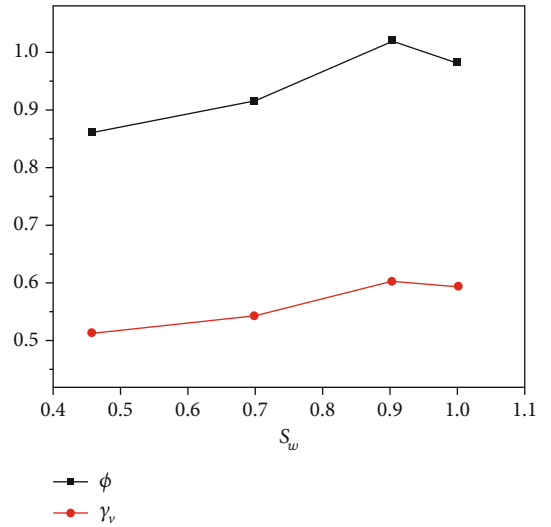


FIGURE 3: Velocity uniformity at different water saturations. The ϕ ($\phi = 1/\text{CV}$) and γ_v value showed the same trend, increased, and then decreased as water saturation decreased.

simplifies the mathematical representation of the interactions between different materials and their corresponding surfaces. Different pressure differences were set for the different models to characterize the distribution of water pressure, and the water flowed under the initial pressure difference.

As a fundamental requirement for solute transport, it was important to determine the principles controlling the fluctuation of the flow field in porous media. The Navier-

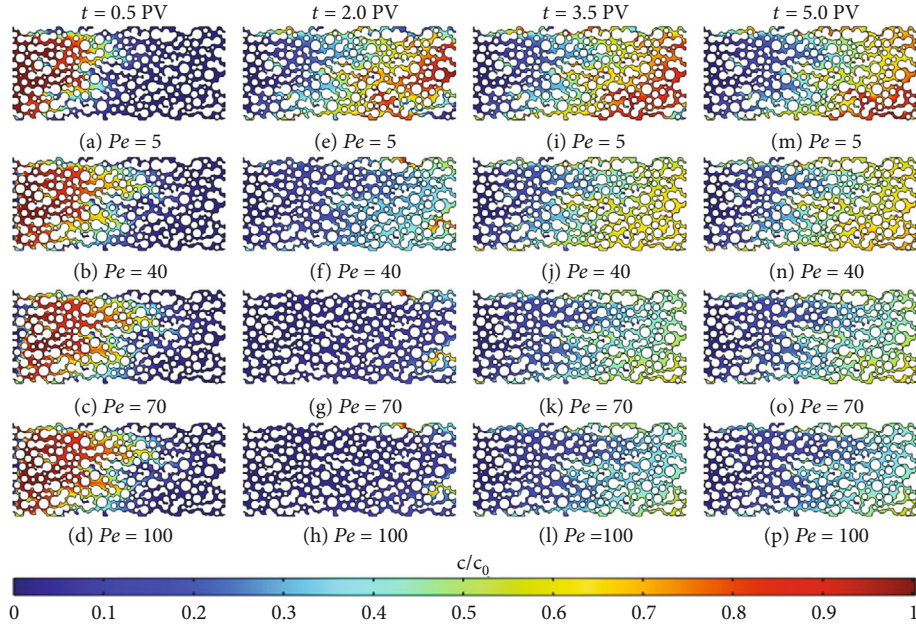


FIGURE 4: Reactive transport processes in porous media ($S_w = 0.902$). c/c_0 is the dimensionless concentration.

Stokes equation was coupled with the advection-diffusion equation to regulate the flow field. Water flow is controlled by applying the pressure difference (5 Pa) between the inlet and outlet. To simulate adsorption behavior at liquid-liquid interfaces in unsaturated porous media in the pore structure, the solute with the specific concentration ($c_0 = 2 \times 10^{-3}$ mol/m³) was injected along the inlet boundary. At the same time, the corresponding reaction rate constants were determined to represent the adsorption reaction at the interface. The specific parameters are given in Table 1.

3. Results and Discussion

3.1. Impact of Water Saturation on the Flow Fields. Figure 2 shows the distribution of the flow field at different water saturations. It can be seen that the distribution of the flow field was complex, and there was a clear phenomenon of preferential flow. This preferential flow generally occurred between two groups of solid particles that formed the dominant channel and were almost parallel to each other. Compared with the flow velocity in the surrounding area, the dominant channel had a higher velocity, and the flow direction was approximately parallel to the water flow. At the same water saturation, the distribution of dominant channels was complex and random due to the influence of pore structure and the distribution of water. Multiple dominant channels may be connected at one location to form a larger dominant channel or separated at another location to form multiple smaller dominant channels. This random separation creates the heterogeneity of the flow field in porous media. In Figure 2, it can be seen that water saturation has a significant influence on the occurrence of connectivity and separation of the dominant flow. The strongest connectivity and separation occurred in the least saturated porous media.

To investigate the phenomenon of preferential flow, the location of the peak velocity of the flow field was selected

for magnification. In Figures 2(a)–2(d), it can be seen that there was a clear phenomenon in the velocity distribution of the flow field in the pore structure: the peak velocity was located on the line connecting the centers of the circles of two groups of nearly parallel solid particles, and the velocity decreased in all directions with the peak velocity as the center. In Figure 2(e), the water flowed in the dominant channel. As the distance between the two groups of solid particles decreased, the flow velocity peaked. However, due to the random distribution of the pores, the particles differed greatly in size, and the dominant channel was divided into two parts, forming two tributaries that continued the flow.

In this study, the profiles of flow velocity were determined to quantitatively evaluate the uniformity of flow velocity. The coefficient of variation [31] and uniformity index [32] were used for the comprehensive analysis.

The coefficient of variation (CV) is dimensionless. It reflects the degree of dispersion of the flow velocity compared to the mean flow velocity and exhibits a negative relationship with the flow field uniformity.

$$S = \sqrt{\frac{1}{n-1} \sum_{i=1}^n (V_i - \bar{V})^2}, \quad (9)$$

$$CV = \frac{S}{\bar{V}} \times 100\%,$$

where S is the standard deviation. V_i [m·s⁻¹] is the velocity value at i , and \bar{V} [m·s⁻¹] is the mean velocity. n represents the total number of sample points obtained.

As the crucial evaluation parameter of the flow field uniformity, the uniformity index (γ_i) shows the flow velocity distribution across the entire section. The range of values is 0 to 1.

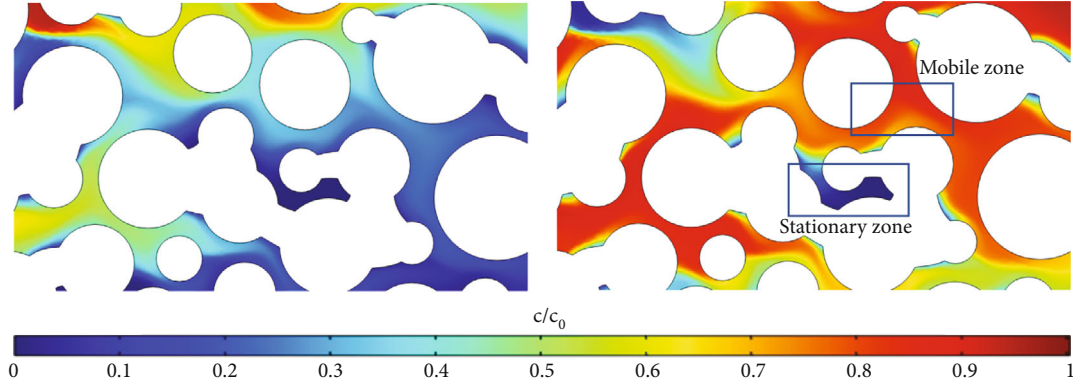


FIGURE 5: Distribution of stationary and mobile zones in the concentration field.

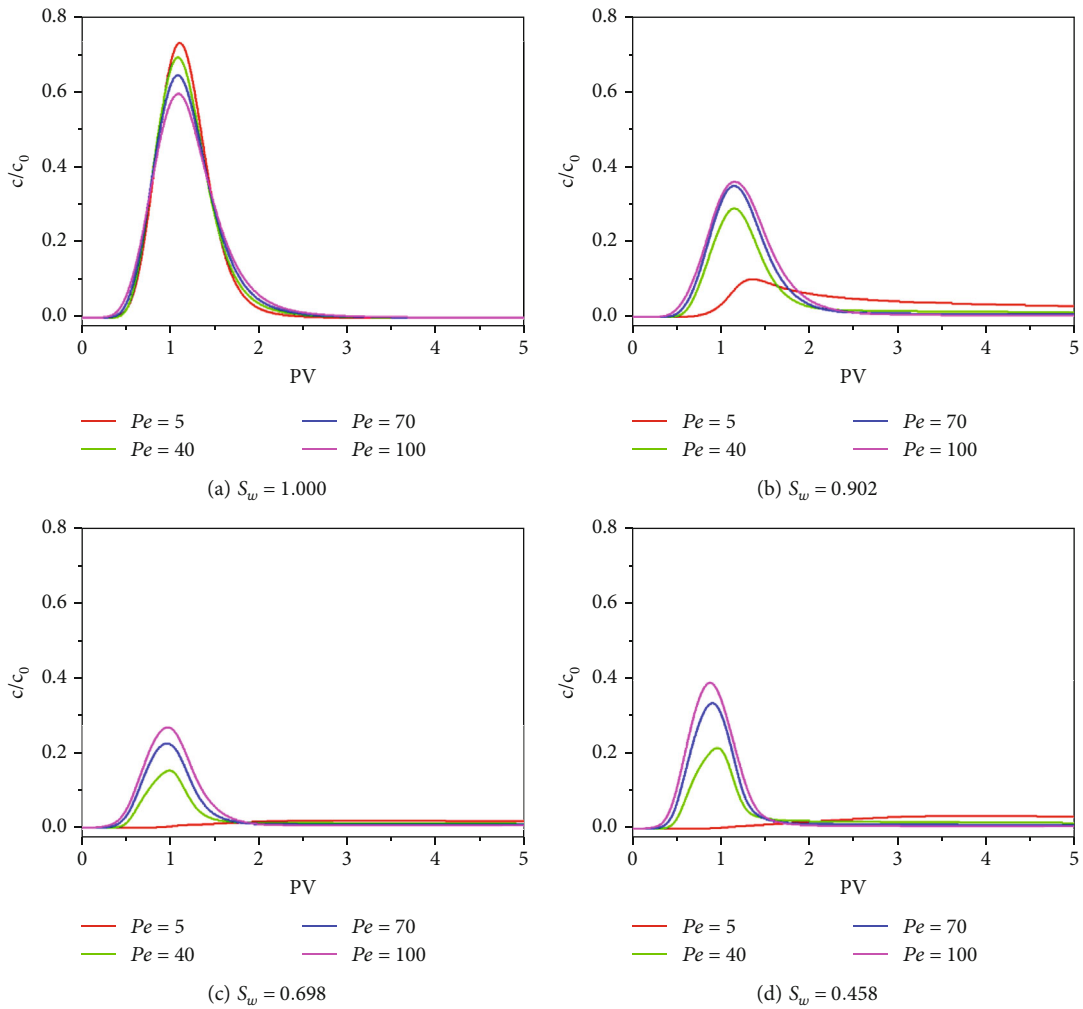


FIGURE 6: Breakthrough curves at different Peclet numbers.

$$\gamma_v = 1 - \frac{1}{2n} \sum_{i=1}^n \frac{\sqrt{(V_i - \bar{V})^2}}{\bar{V}}. \quad (10)$$

According to Table 2, the CV were all close to 1.000 and did not significantly change with water saturation. Mean-

while, the γ_v values at four water saturation were all more than 0.5000. Poor uniformity of the flow field was discovered after a thorough investigation of the two indicators. We plotted the relationship between uniformity and water saturation, as seen in Figure 3, in order to clearly analyze the relationship. Since the CV was inversely related to uniformity, we

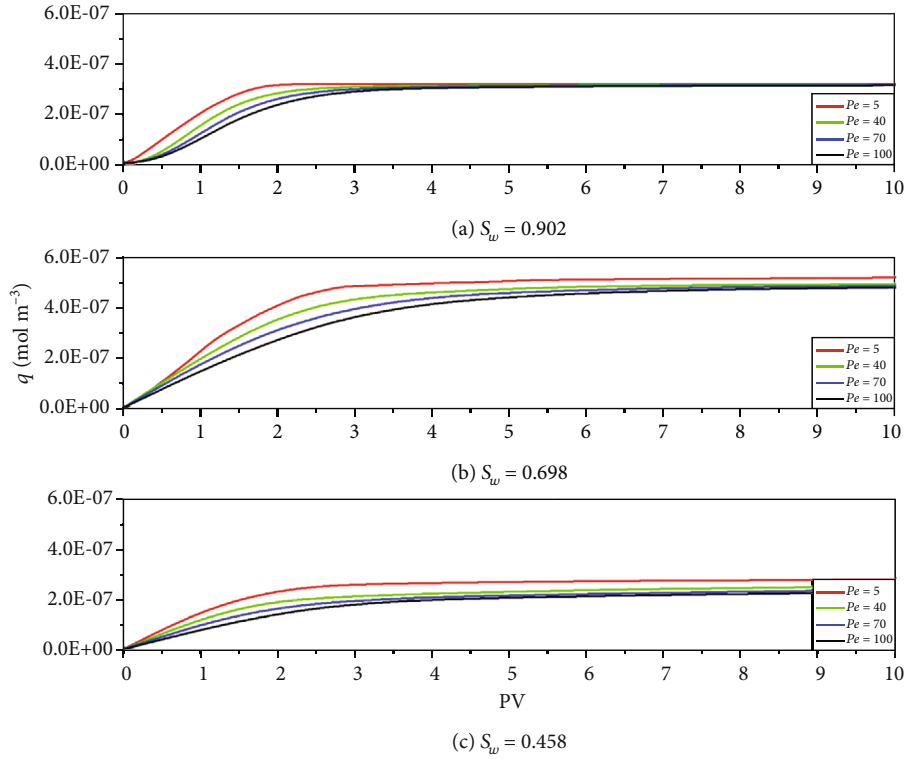


FIGURE 7: The influence of contact time on the adsorbed amount at different Peclet numbers. The adsorbed amount varied regularly with time and gradually increased to equilibrium as time increased.

TABLE 3: The values of the saturated adsorption and adsorption time at different Peclet numbers and water saturations.

Peclet number	Water saturation	q_{max} (mol/m ³)	T (PV)
Pe = 5	$S_w = 0.902$	$3.1730E-7$	2.8093
	$S_w = 0.698$	$5.3186E-7$	17.005
	$S_w = 0.458$	$2.9541E-7$	43.079
Pe = 40	$S_w = 0.902$	$3.1694E-7$	14.363
	$S_w = 0.698$	$5.3157E-7$	131.91
	$S_w = 0.458$	$2.8396E-7$	118.67
Pe = 70	$S_w = 0.902$	$3.1424E-7$	9.2185
	$S_w = 0.698$	$5.3154E-7$	220.02
	$S_w = 0.458$	$2.8405E-7$	208.67
Pe = 100	$S_w = 0.902$	$3.1434E-7$	12.945
	$S_w = 0.698$	$5.3137E-7$	298.81
	$S_w = 0.458$	$2.8421E-7$	300.9

used the inverse of CV ($\phi = 1/CV$) and the γ_v value to effectively indicate the magnitude of the flow field uniformity. The ϕ and γ_v value showed the same trend, increased, and then decreased as water saturation decreased. In other words, the flow uniformity showed a nonmonotonic relationship as water saturation decreased.

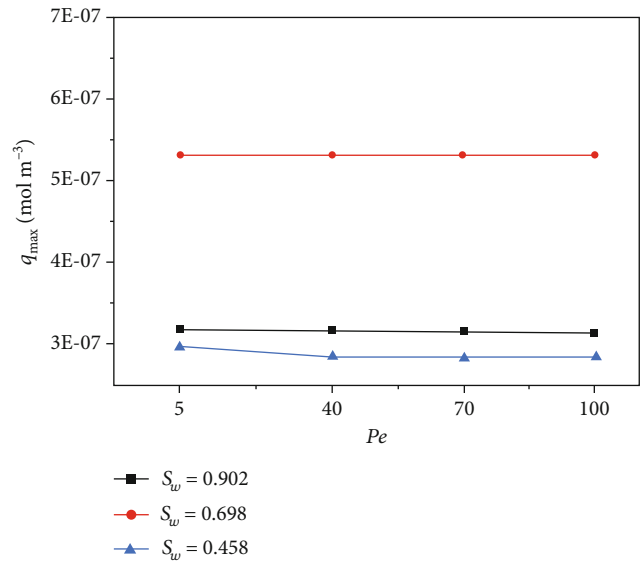


FIGURE 8: The values of the maximum adsorption at different Peclet numbers. Peclet number had little influence on the maximum adsorption.

3.2. Impact of the Peclet Number on Adsorption Behavior at Liquid-Liquid Interfaces. Four different Peclet numbers (Pe = 5, Pe = 40, Pe = 70, and Pe = 100) were set at the same water saturation to investigate the influence of different

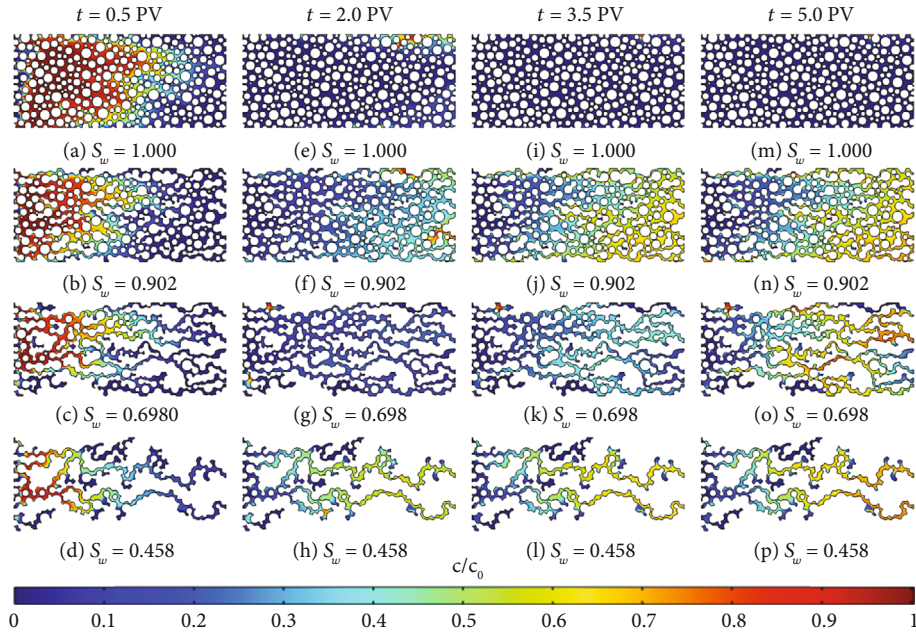


FIGURE 9: Reactive transport processes in porous media ($Pe = 40$). c/c_0 is the dimensionless concentration.

Peclet numbers on reactive transport in unsaturated porous media.

It is evident from Figure 4 that the Peclet number has a significant influence on reactive transport in unsaturated porous media. One or more preferential fronts with high transport rates occurred in the porous media. These fronts were distributed at higher concentrations when the solutes were still at low concentrations in other areas. During solute transport, the solutes first occupied the larger pores and then diffused toward the smaller pores, with several larger pores together forming the preferred channel for solute transport. Large pore channels had a better connection and higher flow velocity than small pore channels, which allowed large pores to load up with solutes at higher head pressures. However, the velocity in small pores was significantly lower than in large pores that form the preferred channels because small pore channels were mainly filled by diffusion due to weak advection. The direction of movement of the fronts formed by solute transport was affected by the distribution of the larger pore spaces, and the fronts moved along the channels formed mainly by the larger pore spaces.

Considering four groups of models of unsaturated porous media with different Peclet numbers at the same water saturation, we find the following: at 0.5 PV, all the solute was injected, and the concentration near the left inlet was in the higher range, but some of the ranges lagged behind the concentration changes in the surrounding area. Then, the injection of water is continued. At 2 PV, the solutes had essentially flowed out of the right outlet, and the entire region was in a state of zero concentration. However, some areas still had a high residual solute concentration and lagged behind the change in the concentration center. Because of this phenomenon, these areas were referred to as “stationary zones.” Stationary zones were usually made up of smaller pores or dead-end pores with a slow flow

velocity and weak advection that relied on diffusion filling of solute molecules, so these areas lagged behind changes in the surrounding area as if they were stopped. In contrast, there were also “mobile zones” (see Figure 5).

In the following simulation period, the solutes in the stationary zone were largely dispersed by the continuous input of water. However, due to adsorption, a large number of solutes were adsorbed on the surface of the nonwetting liquid phase in the initial phase. The desorption reaction at the interface gradually became visible due to the repulsion of water, as shown by the results in Figures 4(i)–4(p). It can be observed that the desorption is strongly affected by the Peclet number. For the models with unsaturated porous media geometry and smaller Peclet number, significantly more solute was desorbed from the surface of the nonwetting liquid, while less was desorbed for the larger Peclet number.

In this study, the outlet boundary was used as the location for calculating the concentration of the breakthrough curves. The simulation time was set to 5 PV in the COMSOL Multiphysics software (0–0.5 PV for solute injection and 0.5–5 PV for water injection), and this was used as the horizontal coordinate. The expression for the dimensionless concentration was as follows.

$$\frac{c}{c_0} = \frac{\int_0^{L_y} (c\bar{u})dy}{\int_0^{L_y} (c_0\bar{u})dy}, \quad (11)$$

where the solute concentration is c [$\text{mol}\cdot\text{L}^{-1}$] and the initial concentration of solute is c_0 [$\text{mol}\cdot\text{L}^{-1}$]. The length of the outlet boundary is L_y . The average velocity of water flow is \bar{u} .

The breakthrough curves for different Peclet numbers at four different water saturations are shown in Figure 6. All BTCs at the same water saturation showed typical characteristics of anomalous transport behavior (e.g., long tails of BTCs).

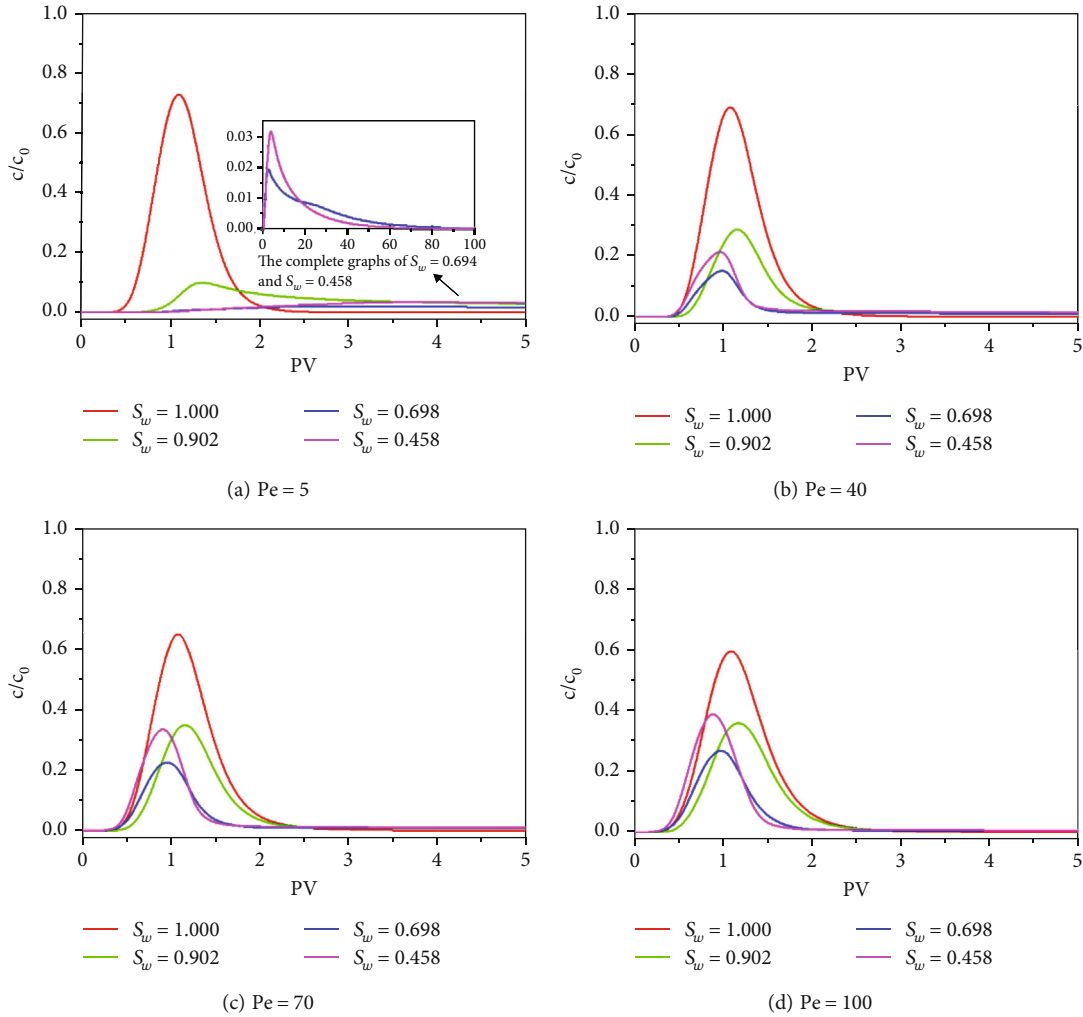


FIGURE 10: Breakthrough curves at different water saturations. The extended simulation time at Pe = 5 to 100 PV revealed the complete trend.

As can be seen in Figure 6, breakthrough curves follow a similar trend at different Peclet numbers. As the Peclet number increased, the arrival time was earlier. This is because advection was the primary mechanism of reactive solute transport. And at larger Peclet numbers, the flow was faster. It should be noted that the breakthrough curves exhibited left-right asymmetry and a significant tailing phenomenon. For the tailing phenomenon, the saturated and unsaturated curves were diametrically opposed. At unsaturated curves, the trailing phenomenon became more pronounced as the Peclet number decreased. In this study, solute chemistry and adsorption in saturated conditions were ignored, so the above phenomena were caused by the microscopic morphology of the pore structure and the inhomogeneous particles within the porous media. In unsaturated conditions, it was the result of a combination of adsorption reactions at the surface of the nonwetting liquid phase and the influencing variables in saturated media.

In order to quantitatively describe the influence of Peclet number on adsorption behavior at liquid-liquid interfaces, 500 PV of contaminate was injected to reach adsorption satu-

ration. The influence of adsorption within 10 PV was exhibited to clearly highlight the trend, as shown in Figure 7. The adsorbed amount at different Peclet numbers varied regularly with time and gradually increased to equilibrium as time increased. At early times, the adsorbed amount increased in a very similar way for all cases, and the adsorption rate decreased with increasing Peclet number. As time increased, the adsorption rate decreased, and the adsorption reached saturation. Table 3 shows the maximum adsorption and adsorption time at different Peclet numbers and water saturations. Further, we also plotted the maximum adsorption at different Peclet numbers as shown in Figure 8. It indicated that the Peclet number had little influence on the maximum adsorption. The adsorption time at saturation, on the other hand, increased with increasing Peclet number and showed a nearly linear relationship with the Peclet number. This is due to the fact that at higher velocities, the ability of solutes to penetrate the interface and experience adsorption is less than the transport capacity in the direction of water flow. Therefore, the adsorption rate is lower at higher flow velocities, and thus, more adsorption time is required.

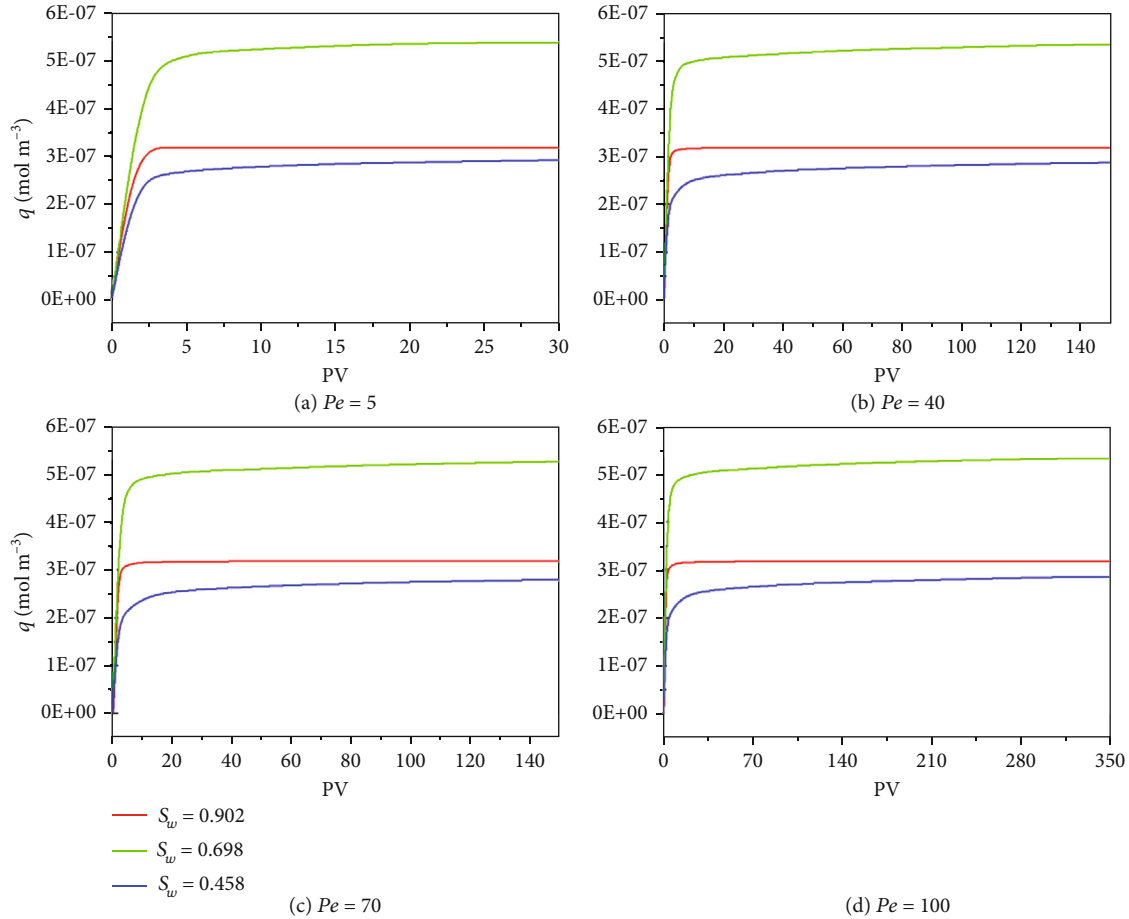


FIGURE 11: The influence of contact time on the adsorbed amount at different water saturations. In the early stage, the adsorbed amount increased in a very similar way, and the adsorption rate increased and then decreased with increasing water saturation.

3.3. Impact of Water Saturation on Adsorption Behavior at Liquid-Liquid Interfaces. The relevant parameters were determined as described above. Numerical simulations with constant PV were performed in four groups of geometric models with different water saturations ($S_w = 0.458$, $S_w = 0.698$, $S_w = 0.902$, and $S_w = 1.000$).

At the same Peclet number, as shown in Figure 9, it became clear that the same phenomenon of preferential flow occurred in reactive transport in the four different water saturation groups. In the less saturated geometric model, more fluids were in the nonwetting phase, resulting in a greater number of fronts with significant separation, compared to the more saturated geometric model in which there were fewer fronts without significant separation. Similarly, there were stationary and mobile zones as the water spread, resulting in strong stagnation.

Figure 10 clearly depicts the influence of the nonwetting phase fluid (TCE) and of the heterogeneity; it adds to the pore structure on reactive transport. The solute shows larger spreading, with earlier arrival times and a more pronounced tailing as water saturation decreases. This is due to the fact that with decreasing water saturation, more fronts existed in the unsaturated porous media, and reactive solute transport along the dominant channel became more obvious.

Although the internal heterogeneity resulted in strong lateral dispersion, the change in transport channels dominated in comparison, resulting in a decrease in transport time.

Similarly, we investigated the direct influence of saturation on adsorption behavior at liquid-liquid interfaces. The adsorbed amount at different water saturations is shown in Figure 11. In the early stage, the adsorbed amount increased in a very similar way, and the adsorption rate increased and then decreased with increasing water saturation. Figure 12(a) also shows a nonlinear relationship between the maximum adsorption and water saturation. The maximum adsorption tended to increase and then decrease as saturation increased. We explained this trend by finding a link with the area in porous media available for adsorption. It can be seen that the adsorption area tends to increase and then decrease with saturation as shown in Figure 12(b). This was consistent with the change in the maximum adsorption with saturation. The maximum adsorption at $S_w = 0.458$ exceeded that of $S_w = 0.698$ (the largest adsorption area), and this was thought to be due to the combined influence of the stationary zone and the preferential front. According to Table 3, the shortest adsorption times occurred in porous media with $S_w = 0.902$. Due to the microscopic morphology of the pore structure and the inhomogeneous particles within

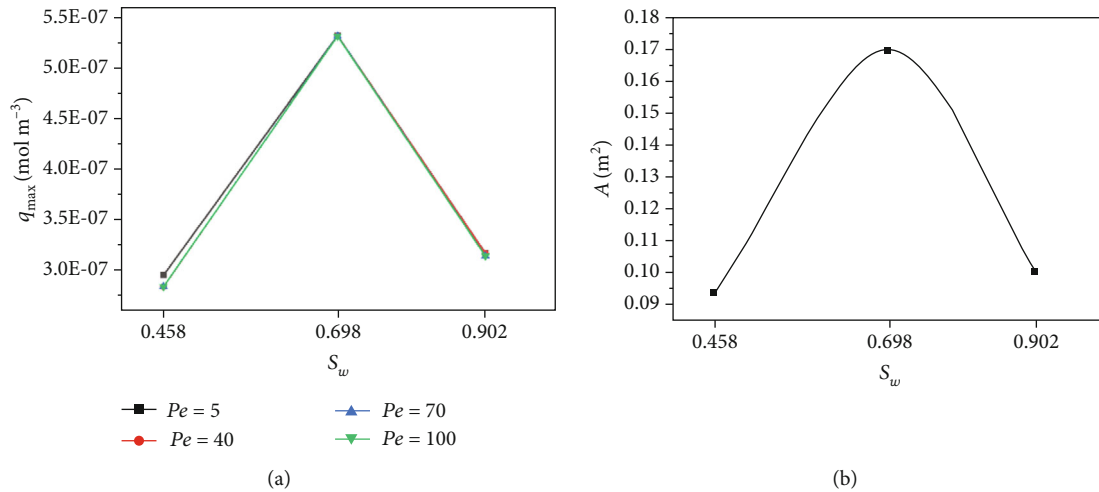


FIGURE 12: The maximum adsorption at different water saturations (a) and relationship between the adsorption area and water saturation (b). Their changes were consistent.

the porous media, $S_w = 0.458$ and $S_w = 0.698$ were substantially longer than those for $S_w = 0.902$. However, the difference in adsorption times for saturations of 0.458 and 0.698 was not significant and was only about 20 PV difference.

4. Conclusions

- (1) The complexity of the flow field was influenced by water saturation, and the uniformity of the flow showed a nonmonotonic relationship with water saturation. Quantitative evaluation of the CV and γ_v values showed that the uniformity of the flow field first increased and then decreased with decreasing water saturation
- (2) The Peclet number had little influence on the maximum adsorption. On the other hand, the adsorption time showed a nearly linear relationship with the Peclet number and increased with increasing Peclet number
- (3) A nonlinear relationship was found between water saturation and the maximum adsorption. With increasing water saturation, the maximum adsorption tended to increase to a peak and then decrease. The peak of the maximum adsorption occurred at $Pe = 5$, $S_w = 0.458$, and the shortest adsorption time was observed at $S_w = 0.902$. However, the difference in adsorption times for saturations of 0.458 and 0.698 was not significant and was only about 20 PV difference

Data Availability

The underlying data used to support the findings of this study are included within the article.

Conflicts of Interest

The authors declare that there is no conflict of interest regarding the publication of this paper.

Acknowledgments

The study is financially supported by the National Key Research and Development Program of China (No. 2019YFC1804300), the National Natural Science Foundation of China (Grant No. 42272278), and the China Scholarship Council (CSC202106710083).

References

- [1] K. H. Wei, J. Ma, B. D. Xi et al., "Recent progress on in-situ chemical oxidation for the remediation of petroleum contaminated soil and groundwater," *Journal of Hazardous Materials*, vol. 432, article 128738, 2022.
- [2] P. Mazumder, A. Das, M. Khwairakpam, and A. S. Kalamdhad, "A comprehensive insight into ecological risk assessment and remediation of metal contaminated coal mine soil: towards a cleaner and sustainable environment," *Journal of Cleaner Production*, vol. 324, article 129185, 2021.
- [3] C. Liu, X. Jiang, Y. Ma, and B. J. Cade-Menun, "Pollutant and soil types influence effectiveness of soil-applied absorbents in reducing rice plant uptake of persistent organic pollutants," *Pedosphere*, vol. 27, no. 3, pp. 537–547, 2017.
- [4] J. Li and Y. Ye, "Analysis of soil heavy metal pollution in Hechuan wetland," *Agricultural Science & Technology*, vol. 18, no. 1, p. 60, 2017.
- [5] S. Mishra, Z. Lin, S. Pang, Y. Zhang, P. Bhatt, and S. Chen, "Biosurfactant is a powerful tool for the bioremediation of heavy metals from contaminated soils," *Journal of Hazardous Materials*, vol. 418, article 126253, 2021.
- [6] C. V. Chrysikopoulos, P. K. Kitanidis, and P. V. Roberts, "Analysis of one-dimensional solute transport through porous media with spatially variable retardation factor," *Water Resources Research*, vol. 26, no. 3, pp. 437–446, 1990.

- [7] G. Sposito, V. K. Gupta, and R. N. Bhattacharya, "Foundation theories of solute transport in porous media: a critical review," *Advances in Water Resources*, vol. 2, pp. 59–68, 1979.
- [8] X. Yang, H. Sun, Y. Yang, Y. Liu, and X. Li, "Recent progress in multi-scale modeling and simulation of flow and solute transport in porous media," *WIREs Water*, vol. 8, no. 6, article e1561, 2021.
- [9] Y. Li, J. Bian, Q. Wang, and T. Li, "Experiment and simulation of non-reactive solute transport in porous media," *Groundwater*, vol. 60, no. 3, pp. 330–343, 2022.
- [10] A. X. Wu, C. Liu, S. H. Yin, Z. L. Xue, and X. Chen, "Pore structure and liquid flow velocity distribution in water-saturated porous media probed by MRI," *Transactions of Non-ferrous Metals Society of China*, vol. 26, no. 5, pp. 1403–1409, 2016.
- [11] M. Wang, H. Liu, D. Zak, and B. Lennartz, "Effect of anisotropy on solute transport in degraded fen peat soils," *Hydrological Processes*, vol. 34, no. 9, pp. 2128–2138, 2020.
- [12] X. P. Zhou and N. Xiao, "Analyzing fracture properties of the 3D reconstructed model of porous rocks," *Engineering Fracture Mechanics*, vol. 189, pp. 175–193, 2018.
- [13] Z. Liu, D. Liu, Y. Cai, Y. Yao, Z. Pan, and Y. Zhou, "Application of nuclear magnetic resonance (NMR) in coalbed methane and shale reservoirs: a review," *International Journal of Coal Geology*, vol. 218, article 103261, 2020.
- [14] B. Zhao, G. Wang, B. Wu, and X. Kong, "A study on mechanical properties and permeability of steam-cured mortar with iron-copper tailings," *Construction and Building Materials*, vol. 383, article 131372, 2023.
- [15] M. Luo, P. W. Glover, P. Zhao, and D. Li, "3D digital rock modeling of the fractal properties of pore structures," *Marine and Petroleum Geology*, vol. 122, article 104706, 2020.
- [16] Y. Zhao, X. Sun, T. Wen, R. Chen, and L. Huang, "Micro-structural evolution of granite residual soil under external loading based on X-ray micro-computed tomography," *KSCSE Journal of Civil Engineering*, vol. 25, no. 8, pp. 2836–2846, 2021.
- [17] S. Jiménez, R. Brauchler, R. Hu et al., "Prediction of solute transport in a heterogeneous aquifer utilizing hydraulic conductivity and specific storage tomograms," *Water Resources Research*, vol. 51, no. 7, pp. 5504–5520, 2015.
- [18] J. Niu and M. S. Phanikumar, "Modeling watershed-scale solute transport using an integrated, process-based hydrologic model with applications to bacterial fate and transport," *Journal of Hydrology*, vol. 529, pp. 35–48, 2015.
- [19] L. Budinski, "Solute transport in shallow water flows using the coupled curvilinear lattice Boltzmann method," *Journal of Hydrology*, vol. 573, pp. 557–567, 2019.
- [20] M. Morales-Hernández, J. Murillo, and P. García-Navarro, "Diffusion–dispersion numerical discretization for solute transport in 2D transient shallow flows," *Environmental Fluid Mechanics*, vol. 19, no. 5, pp. 1217–1234, 2019.
- [21] D. Costa, K. Shook, C. Spence et al., "Predicting variable contributing areas, hydrological connectivity, and solute transport pathways for a Canadian Prairie basin," *Water Resources Research*, vol. 56, no. 12, article e2020WR027984, 2020.
- [22] A. L. Harrison, G. M. Dipple, I. M. Power, and K. U. Mayer, "Influence of surface passivation and water content on mineral reactions in unsaturated porous media: implications for brucite carbonation and CO₂ sequestration," *Geochimica et Cosmochimica Acta*, vol. 148, pp. 477–495, 2015.
- [23] A. L. Harrison, G. M. Dipple, I. M. Power, and K. U. Mayer, "The impact of evolving mineral–water–gas interfacial areas on mineral–fluid reaction rates in unsaturated porous media," *Chemical Geology*, vol. 421, pp. 65–80, 2016.
- [24] A. Raoof, H. M. Nick, S. M. Hassanizadeh, and C. J. Spiers, "PoreFlow: a complex pore-network model for simulation of reactive transport in variably saturated porous media," *Computers & Geosciences*, vol. 61, pp. 160–174, 2013.
- [25] J. Jiménez-Martínez, P. D. Anna, H. Tabuteau, R. Turuban, T. L. Borgne, and Y. Méheust, "Pore-scale mechanisms for the enhancement of mixing in unsaturated porous media and implications for chemical reactions," *Geophysical Research Letters*, vol. 42, no. 13, pp. 5316–5324, 2015.
- [26] A. J. Valocchi, D. Bolster, and C. J. Werth, "Mixing-limited reactions in porous media," *Transport in Porous Media*, vol. 130, no. 1, pp. 157–182, 2019.
- [27] Z. Dou, X. Zhang, C. Zhuang, Y. Yang, J. Wang, and Z. Zhou, "Saturation dependence of mass transfer for solute transport through residual unsaturated porous media," *International Journal of Heat and Mass Transfer*, vol. 188, article 122595, 2022.
- [28] L. Yue, C. Ge, D. Feng, H. Yu, H. Deng, and B. Fu, "Adsorption-desorption behavior of atrazine on agricultural soils in China," *Journal of Environmental Sciences*, vol. 57, pp. 180–189, 2017.
- [29] D. Lyu, Y. B. Mollamahale, S. Huang et al., "Ultra-high surface area graphitic Fe–N–C nanospheres with single-atom iron sites as highly efficient non-precious metal bifunctional catalysts towards oxygen redox reactions," *Journal of Catalysis*, vol. 368, pp. 279–290, 2018.
- [30] Z. Dou, X. Zhang, Z. Chen, Y. Yang, C. Zhuang, and C. Wang, "Effects of cemented porous media on temporal mixing behavior of conservative solute transport," *Water*, vol. 11, no. 6, p. 1204, 2019.
- [31] A. Saif, R. R. William, B. A. Daryl, and Z. Hailin, "Prediction of maize (*Zea mays* L.) population using normalized-difference vegetative index (NDVI) and coefficient of variation (CV)," *Journal of Plant Nutrition*, vol. 42, no. 6, pp. 673–679, 2019.
- [32] S. Jafaradar, H. Taghavifar, H. Taghavifar, and A. Navid, "Numerical assessment of flow dynamics for various DI diesel engine designs considering swirl number and uniformity index," *Energy Conversion and Management*, vol. 110, pp. 347–355, 2016.

Research Article

Evolutions of Anisotropic Hydraulic Properties of Rough-Walled Rock Fractures under Different Shear Displacements

Dapeng Lu 

China Railway No. 10 Engineering Group Co. Ltd., Jinan 250101, China

Correspondence should be addressed to Dapeng Lu; dapenglu@126.com

Received 28 December 2022; Revised 17 February 2023; Accepted 5 April 2023; Published 15 May 2023

Academic Editor: Bao Jia

Copyright © 2023 Dapeng Lu. This is an open access article distributed under the Creative Commons Attribution License, which permits unrestricted use, distribution, and reproduction in any medium, provided the original work is properly cited.

Four cylindrical sandstone samples were extracted from the original rectangular sample with a rough-walled fracture. Each drilling angle (θ) of cylindrical sandstone samples is different to consider the anisotropies of rough-walled rock fractures. For each sample, different flow velocities ranging from 0 m/s to 13 m/s were designed. For a given flow velocity, a series of different confining pressures (σ_n), including 1.5 MPa, 2.5 MPa, and 3.5 MPa, were applied on the fractured samples. The hydraulic properties of each cylindrical sandstone sample were tested under different shear displacements (u_s) and σ_n . The results show that the hydraulic gradient (J) shows an increasing trend with the increment of σ_n . With the increment of the Reynolds number (Re), the transmissivity (T) decreases in the form of the quadratic function. The normalized transmissivity (T/T_0) decreases with the increment of J . The variations in T/T_0 with J can be divided into three stages. The first stage is that T/T_0 approximately holds a constant value of 1.0 when J is small indicating that the fluid flow is in the linear regime. The last two stages are that T/T_0 decreases with the continuous increase of J , and the reduction rate first increases and then decreases. The critical Reynolds number (Re_c) of the sample angle with a drilling angle of 90° is different from that of other samples. The corresponding Re_c is 6.52, 28.73, and 32.1 when the shear displacement (u_s) = 2 mm, 3 mm, and 4 mm, respectively. The variations in Re_c and J along different drilling angles are significantly obvious. When the confining pressure is large, the effect of anisotropy on Re_c is much greater than that of confining pressure.

1. Introduction

Rock fracture network plays a critical role in controlling the main paths of contaminant migration and fluid flow in tight rock masses [1–5]. During the past several decades, the permeability of fractured rock masses has been extensively studied in many geosciences and geoengineering such as geothermal energy development, enhanced oil recovery, and CO₂ sequestration [6, 7]. The rock fractures are commonly assumed to be parallel plate models and obey the cubic law, in which the flow rate is linearly correlated to the hydraulic gradient [3, 8]. However, the natural surface of fractures is rough, in which fluid flows through the nonlinear flow regime, and the flow rate is nonlinearly proportional to the hydraulic gradient [9]. Therefore, the estimation of the hydraulic properties of rough-walled rock fractures contributes to the accurate assessment of the flow properties of fractured rock masses.

Previous studies have reported that the geometry of rough-walled fractures significantly influences the flow properties of the rock masses [2, 10–14]. Zou et al. [14] developed a two-dimensional (2D) finite volume method (FVM) code to examine the effects of the original wall surface roughness of fractures on fluid flow. Liu et al. [2] summarized the mathematical expressions for the effects of aperture distribution and anisotropy on the equivalent permeability of DFNs. Huang et al. [11] originally developed a numerical procedure to effectively calculate fluid flow through 3D discrete fracture network (DFN) models and systematically investigated the roughness of fracture surface and anisotropy of aperture distribution on the permeability of DFN models. Kong and Chen [12] simulated fluid flow behavior within the three-dimensional (3D) rough fractures to study the influence of the properties of the rough fracture surface on the fracture conductivity. He et al. [10] carried out laboratory triaxial seepage tests to study the seepage characteristics of the columnar

fractured rock masses at the Baihetan hydropower dam sites. The experimental results showed that the similar material model samples of columnar fractured rock mass showed obvious seepage anisotropies. Gong et al. [15, 16] presented a new heavily parallelized, dynamic pore-network modeling platform that is capable of simulating two-phase flow in rough-walled fractures with high computational efficiency. Lavrov [13] performed four finite-difference schemes to numerically evaluate the fluid flow in rough-walled fractures. However, underground excavation and/or earthquakes can induce significant deformation of preexisting fractures in rock masses. Due to the slip-along fractures, the flow properties of fractured rock masses can be influenced. Therefore, considering the effect of shear displacement on the flow properties of fractured rock masses is necessary.

Many studies have focused on the effect of share-induced deformation [17–24]. Kim et al. [24] developed analytical and numerical techniques, which combined micromechanics-based continuum (MBC) model analysis and FracMan/Mafic package, for calculating fluid flow through a single rock joint and the transmissivities due to shearing. Ahmadi et al. [17] imposed contact asperities of saw-tooth-like structures and in the shear direction to investigate the effects of the degree of contact between the fracture faces on the compliance ratio in the stiff direction. Lang et al. [20] developed a numerical approach to investigate the influences of transmissivity anisotropy induced by shearing on the overall permeability of fractured rock masses based on contact mechanics. Liu et al. [21, 22] proposed a modified successive random additions (SRA) algorithm to generate the rough fracture surface and used a mechanistic model to calculate the distribution of aperture during shearing. Cardona et al. created synthetic fractal surfaces using the power law, contact mechanics, and kinematic constraints to explore the evolution of aperture distribution during shear displacement and normal loading. Song et al. [23] performed direct shear tests to study the description of permeability anisotropy-based joint shear deformation of natural sandstone replicated by artificial materials. Chen et al. [19] carried out direct shear test conditions to study the influence of anisotropy of roughness on the shear failure mechanism of fracture surfaces under constant normal load (CNL). However, the anisotropic of rough-walled rock fracture during shearing has not been studied in the previous studies.

In the present study, four standard sandstone samples were extracted from the original sandstone sample. A rough-walled fracture exists in the original sandstone sample. To consider the anisotropic properties of rough-walled rock fractures, intersection angles between the axis along the height direction of cylindrical standard sandstone samples and the axis along the height direction of the original sample are different. The hydraulic properties of each standard sandstone sample were tested under different shear displacements and confining pressures.

2. Experimental Setup

2.1. Original Sample Preparation and Surface Roughness Measurement. The porosity and permeability of the matrix

of sandstones used in this study are 20.3% and $2.71 \times 10^{-8} \text{ m}^2$. The original rock block was cut and polished to a rectangular sample. The size of the rectangular block is 200 mm in length, 100 mm in width, and 100 mm in height. Brazilian splitting test was performed to manufacture tensile fracture along the center of the rectangular block in the height direction.

Three-dimensional characterization and digital reconstruction of fracture surface topography were carried out using a high-precision noncontact 3D laser scanner as shown in Figure 1(a). The 3D laser scanner has a horizontal (x, y) scanning accuracy of $\pm 20 \mu\text{m}$ and a vertical (z) scanning accuracy of $\pm 10 \mu\text{m}$.

The scanning interval in both x and y directions is set to 0.5 mm, and the 3D reconstruction results are shown in Figure 1(b). According to the recommended method of the International Society for Rock Mechanics and Engineering [25], a series of equidistant two-dimensional (xz) sections are extracted every 2 mm along the y direction on the three-dimensional rough fracture surface to quantitatively characterize the roughness coefficient of the three-dimensional fracture surface. Referring to the experiences of previous scholars [26], the point spacing of 1 mm is selected along the y direction for the two-dimensional section and the joint roughness coefficient (JRC) is calculated according to the following formulas:

$$Z_2 = \left[\frac{1}{M} \sum \left(\frac{z_{i-1} - z_i}{x_{i-1} - x_i} \right)^2 \right]^{1/2}, \quad (1)$$

$$\text{JRC} = 32.2 + 32.47 \lg Z_2, \quad (2)$$

where M is the number of sample points selected along the y direction, x_i and z_i are the coordinates of sample points on the two-dimensional contour.

As shown in Figure 2(a), the fracture surface height of fracture surface goes through three stages, including uphill, hill, and downhill, along the y direction (shear direction). The fluctuation height distribution frequency of the scanning point obeys the typical Gaussian distribution. The minimum value of fracture surface height is 3.08 mm, and the maximum value of fracture surface height is 12.43 mm. The mean value of fracture surface height is 7.91 mm, and the standard deviation (StDev) is 1.92 mm. The distribution of JRC values of two-dimensional (xz) sections, which are extracted every 2 mm along the y direction on the three-dimensional rough fracture surface, is shown in Figure 2(b).

2.2. Sample Extraction. The sample preparation process can be divided into three stages. First, cylindrical samples were extracted from the original rectangular sandstone using different sampling methods as shown in Figures 3(a)–3(c). The preparation process of the original rectangular sandstone sample and the geometrical characteristics of the artificial fracture surface in the specimen have been described in Section 2.1. In the extraction process, each drilling angle between the axis along the height direction of cylindrical

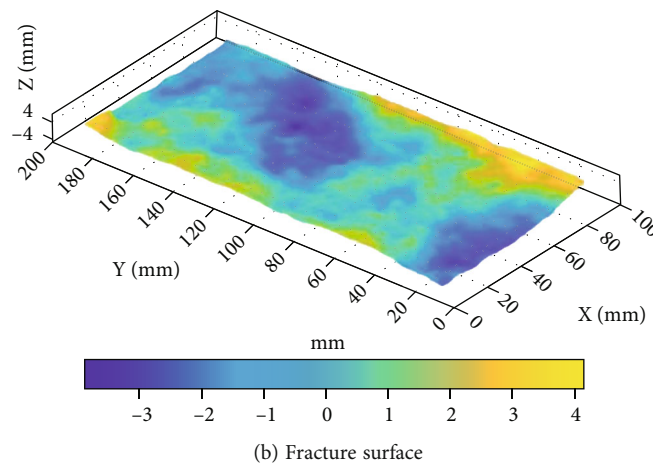
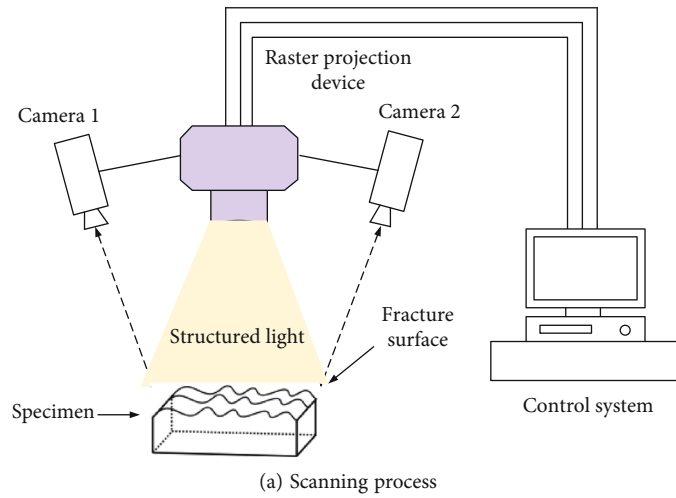


FIGURE 1: Roughness acquisition.

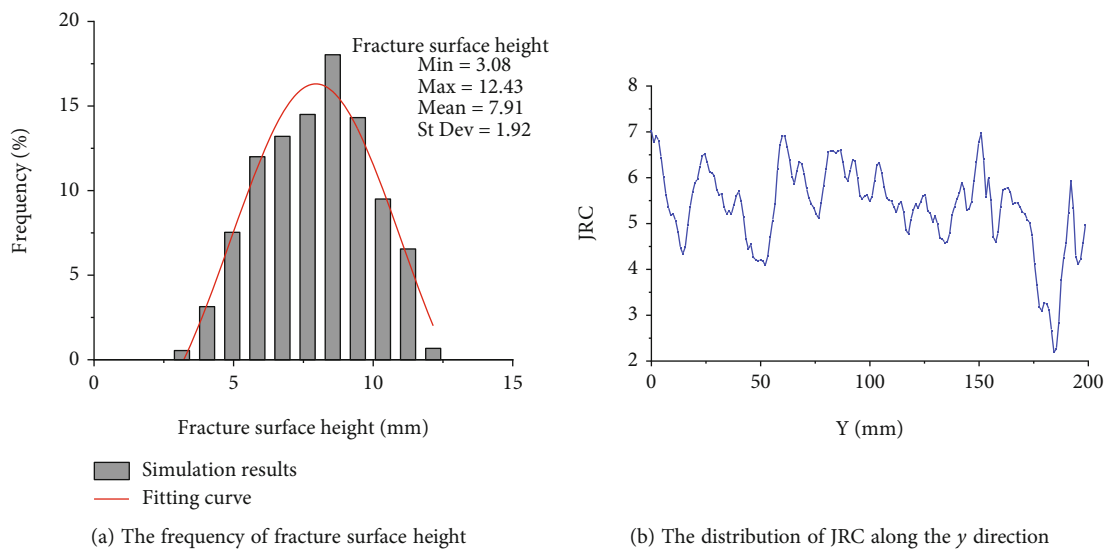


FIGURE 2: The geometric characteristics of the rough fracture surface.

sandstone samples and the artificial fracture of the original sample is different. The four drilling angles are 0°, 45°, 90°, and 135°. Samples drilled at 0° and 90° are samples with a

diameter of 50 mm and a height of 100 mm, as shown in Figure 3(d). The sizes of samples drilled at 45° and 135° are 50 mm in diameter and 70 mm in height. Since the drilling

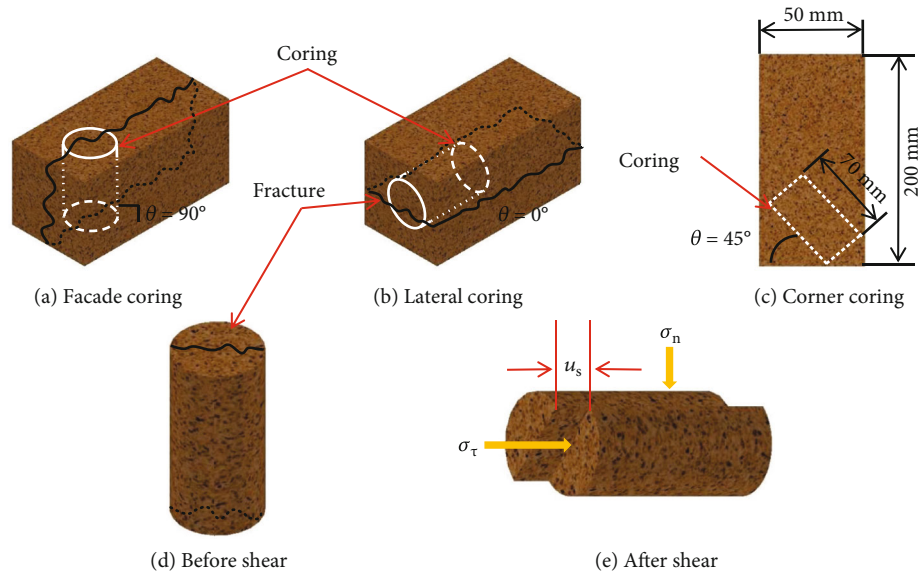


FIGURE 3: Sample preparation: (a–c) sandstone with varying coring methods, (d) cored sandstone sample, and (e) extraction process during shearing.

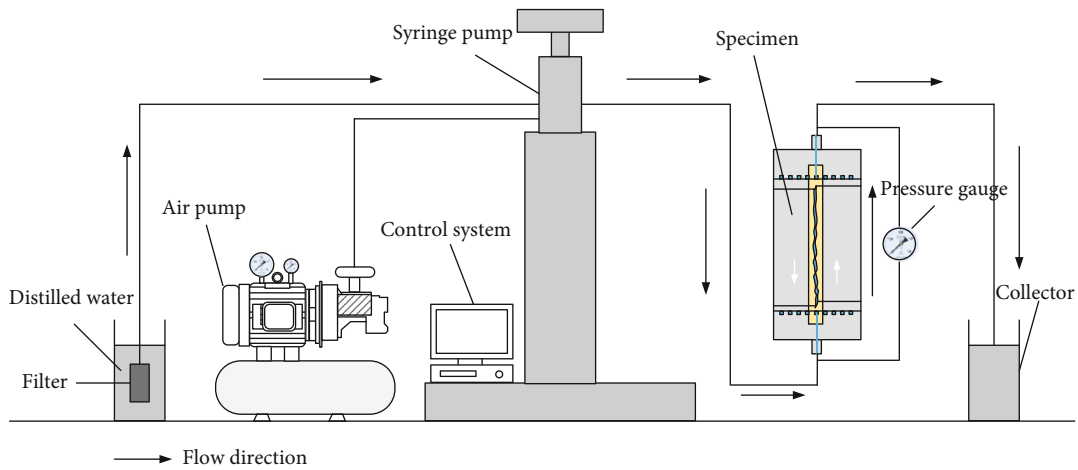


FIGURE 4: Multifunctional seepage testing apparatus.

angles of 45° and 135° are symmetrical, only 45° is shown in Figure 3(c).

To investigate the influence of the shear displacement on the hydraulic properties of cylindrical samples, the position of the rock blocks on both sides of the fracture is adjusted according to the shear displacement (u_s) as shown in Figure 3(e). The shear displacement is set to be 2 mm, 3 mm, and 4 mm, respectively. In order to ensure the stability of the sample during the seepage test, rigid gaskets are added at both ends of the cylindrical samples.

2.3. Testing Procedure. The seepage tests under different flow velocities and confining pressures (σ_n) were carried out using the multifunctional seepage testing system as shown in Figure 4. The test system is mainly consisted of the water injection device, sample holder, and data acquisition device. The water injection device includes a filter, air pump, syringe

pump, and control system. The data acquisition device includes a pressure gauge and collector. The sample holder can apply confining pressure on the cylindrical sample. The accuracy of confining pressure was 0.1 MPa, and the accuracy of the volumetric flow velocity was 0.01 m/s. For each sample, different flow velocities ranging from 0 m/s to 13 m/s were designed. For a given flow velocity, different confining pressures (σ_n) were applied. During the test process, the fractured sample was first put into the holder after being equipped with a rubber sleeve. Then, different confining pressures, including 1.5 MPa, 2.5 MPa, and 3.5 MPa, were applied on the fractured sample. Applying axial stress can effectively protect the rubber sleeve from being damaged by the confining pressure. For a given flow velocity and confining pressure, the difference in pressure gradient (∇P) between the inlet and the outlet of the samples and flow rate (Q) was recorded in real-time using the automatic data acquisition system.

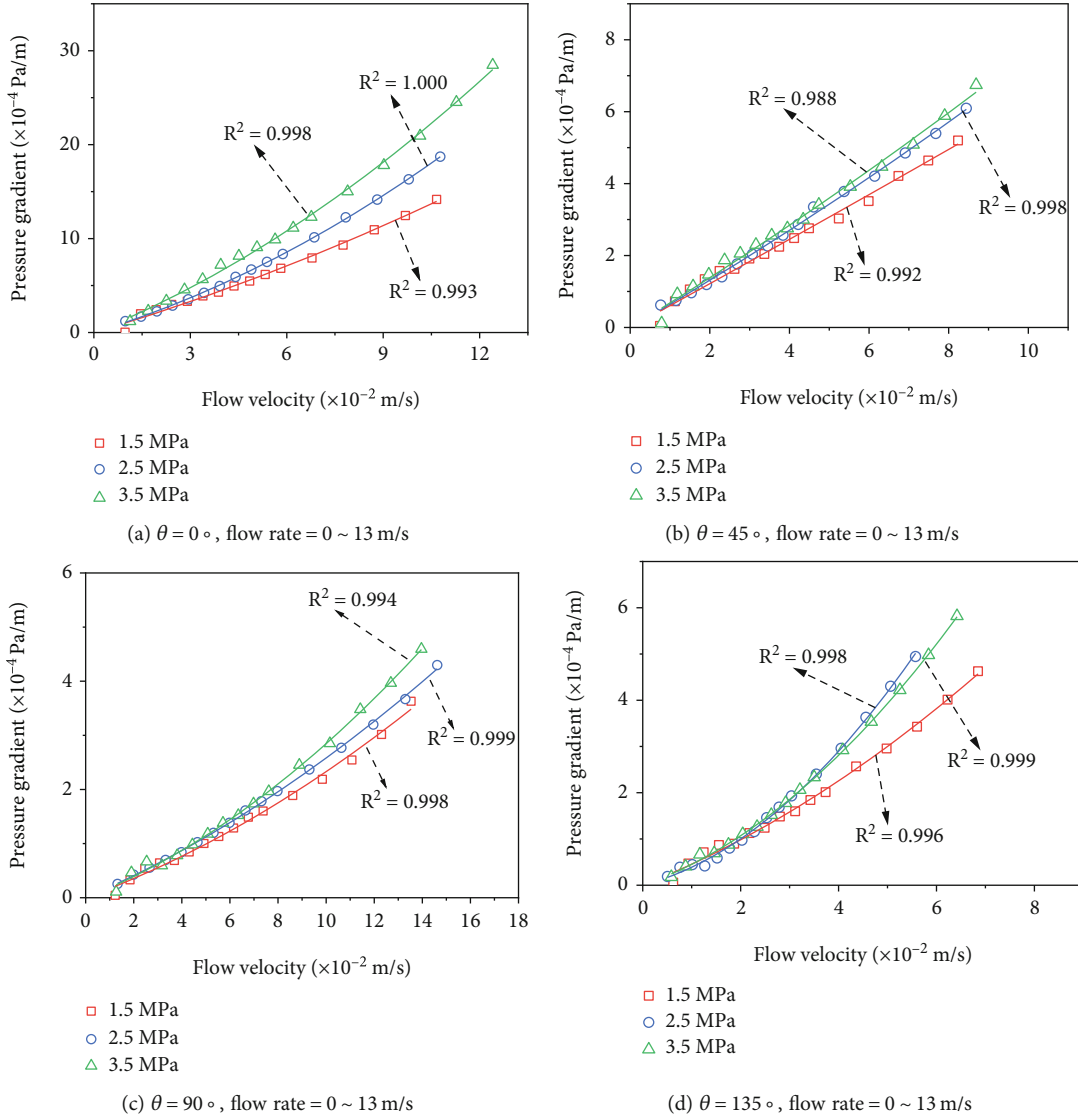


FIGURE 5: Evolution of pressure gradient under different confining pressures σ_n and drilling angle θ with varying flow velocity from 0 to 13 m/s.

The Reynolds number Re is defined as the ratio of inertial forces to the viscous forces and can be formulated as follows [27, 28]:

$$Re = \frac{\rho Q}{\mu w}, \quad (3)$$

where ρ is the fluid density, w is the fracture width, and μ is the dynamic viscosity.

The apparent transmissivity T is a commonly used parameter to describe the flow state of fluids. If the flow follows a Darcy-type law, it is found that T is independent of Re :

$$T = \frac{E^3}{12} = -\frac{\mu Q}{w \nabla P} = -\frac{\mu Q}{w(AQ)} = T_0 = \text{constant}, \quad (4)$$

where E is the hydraulic aperture, A is the linear coefficient, and T_0 is the intrinsic transmissivity.

As the flow rate increases, doubling the pressure drop does not produce a double flow rate, which is known as the nonlinear flow. In this regime, the apparent transmissivity is given by the following:

$$T = -\frac{\mu Q}{w \nabla P} = -\frac{\mu Q}{w(AQ + BQ^2)}, \quad (5)$$

where B is the nonlinear coefficient.

For a fixed flow channel, a nonlinear relationship between flow rate and pressure drop exists for a strong inertial regime, especially at a relatively high flow rate. The normalized transmissivity (T/T_0) is defined as the ratio of apparent transmissivity (T) to intrinsic transmissivity (T_0), which is used to characterize the transition of fluid from

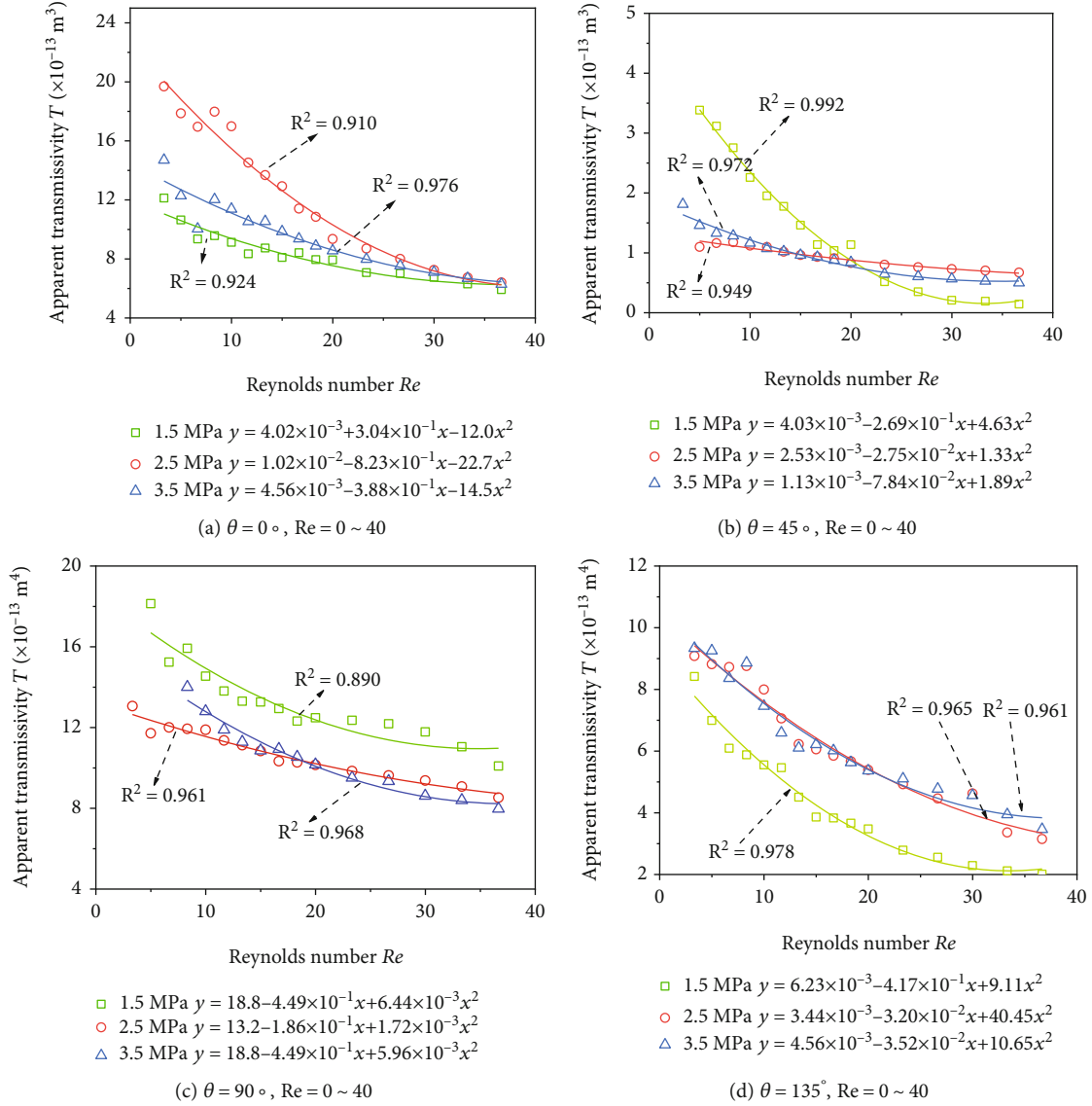


FIGURE 6: Evolution of apparent transmissivity T under different confining pressures σ_n and drilling angle θ with varying Reynolds' number Re from 0 to 40.

linear regimes to nonlinear regimes. Therefore, the rate of T to T_0 is calculated by the following:

$$\frac{T}{T_0} = \frac{-\mu Q/w(AQ + BQ^2)}{-\mu Q/w(AQ)} = \frac{AQ}{AQ + BQ^2}. \quad (6)$$

When the fluid flow is in a linear state, T_0 corresponds to the value of T . When the nonlinear term (BQ^2) accounts for 10% of the pressure drop, that is, $T/T_0 = 0.9$, it is considered as the critical condition for the fluid to change from linear to nonlinear [29–31].

3. Results and Discussion

3.1. Effect of Extraction Angle of Standard Samples on Hydraulic Properties. Figure 5 shows the relationships between $-\nabla P$ and Q for water flow through the fracture.

The flow velocity is in the range of 0–13 m/s, and the corresponding pressure gradient is in the ranges of $0 - 27.9 \times 10^{-4}$, $0 - 6.7 \times 10^{-4}$, $0 - 4.5 \times 10^{-4}$, and $0 - 5.8 \times 10^{-4}$ Pa/m, for $\theta = 0^\circ$, 45° , 90° , and 135° , respectively. For a certain θ , as σ_n increases, the pressure gradient shows an increasing trend. The best-fit regression analyses were conducted on the experimental data using the Forchheimer equation and were plotted as the solid lines. The values of residual squared R^2 for all cases are larger than 0.99, which indicates that the experimental values agree well with the fitting curves.

$T/T_0 = 0.9$ has the same physical meaning that the nonlinear term (BQ^2) contributes to 10% of the pressure drop, in which the current Re is Re_c . As shown in Figure 6, with the increment of Re , the T presented a reduction trend, and the decreasing rate gradually weakened, which confirmed the existence of flow nonlinearity in fractures. Figure 7 shows that Re_c is in the ranges of 5.4–13.4, 18.8–32.1, 3.92–7.47,

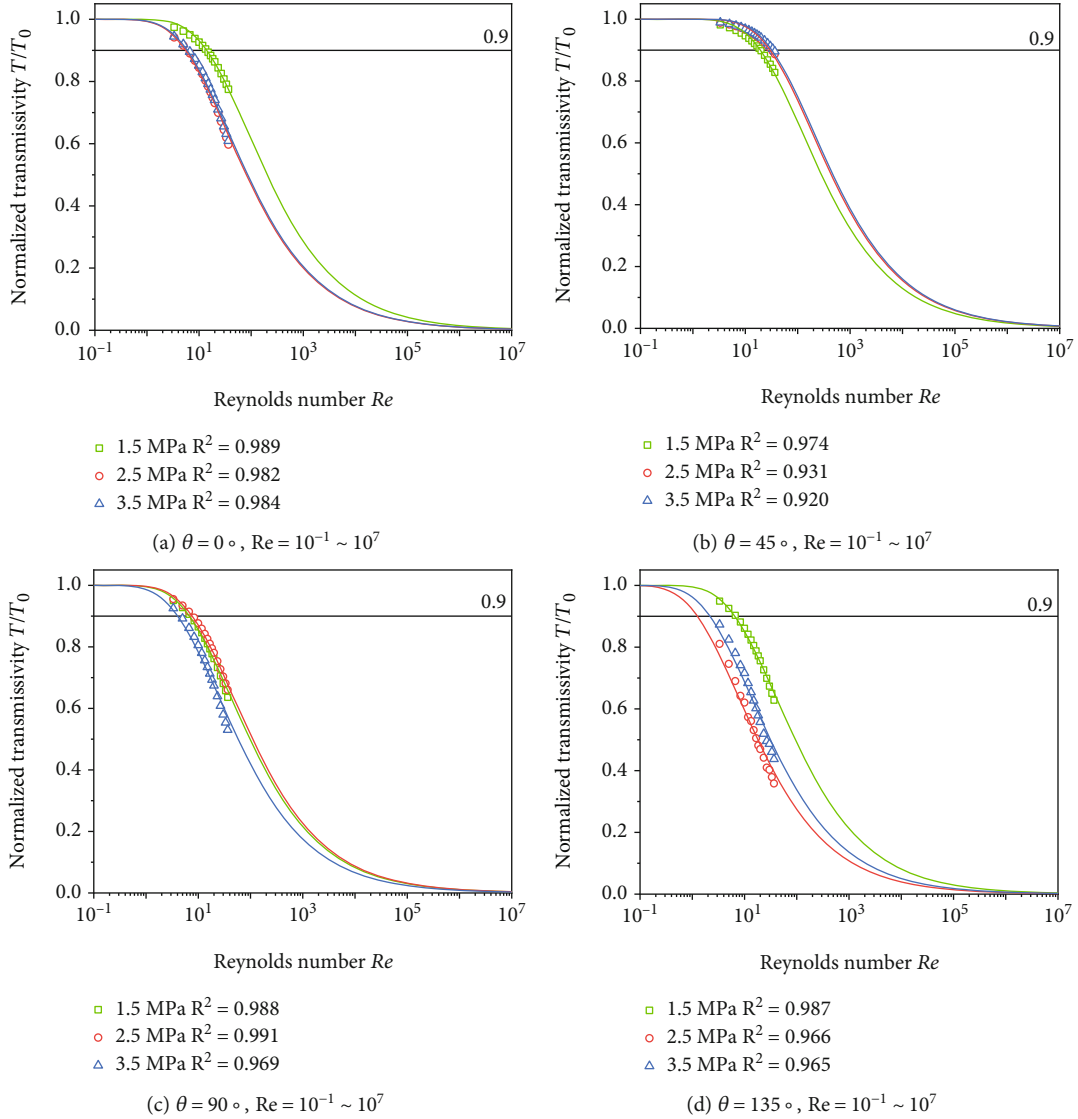


FIGURE 7: Evolution of the normalized transmissivity T/T_0 under confining pressures σ_n and drilling angle θ with varying Reynolds' number Re .

and 1.16-6.69 for $\theta = 0^\circ$, 45° , 90° and 135° , respectively. Generally, T/T_0 remains constant at 1.0 for $Re = 0.01 - 1$ with $\theta = 0^\circ$, 45° and 90° , and it exhibits a remarkable decrease when $Re > 1$. When $\theta = 135^\circ$, T/T_0 remains constant at 1.0 for $Re = 0.01 - 0.1$, and it exhibits a remarkable decrease when $Re > 0.1$.

For fluid flow through fractured media, the normalized transmissivity T/T_0 has also been applied to estimate the nonlinear flow regime [32]. The variations in T/T_0 against J can be expressed as follows:

$$\frac{T}{T_0} = 1 - \exp(-\alpha J^{-0.45}). \quad (7)$$

The values of T/T_0 were calculated and plotted in terms of J as shown in Figure 8. As J increases, T/T_0 shows a downward trend. The variations in T/T_0 with J can be divided into three stages. When J is small, T/T_0 approxi-

mately holds a constant value of 1.0; thus, the fluid flow is within the linear regime. Then, with the continuous increase of J , T/T_0 decreases, and the reduction rate first increases and then decreases. Based on Equation (7), when $T/T_0 = 0.9$, J_c can be calculated and is in the ranges of 2.26-5.12, 4.27-5.71, 0.09-0.66 for $\theta = 0^\circ$, 45° , 90° , 135° , respectively.

3.2. Effect of Shear Displacement on Hydraulic Properties. The dislocation of rock will change the void space in the fracture. As a result, the shear displacement will cause the change of the fracture seepage characteristics, such as T and T/T_0 . Different shear displacements are carried out for the fractures with different cutting angles, and the evolution characteristics of T/T_0 are shown in Figure 9. With the increase of hydraulic gradient, T/T_0 gradually decreases, which means that the proportion of nonlinear flow is increasing. This is because with the increase in hydraulic gradient, the inertial flow of the fracture increases, and the sample is more able to enter the nonlinear flow stage.

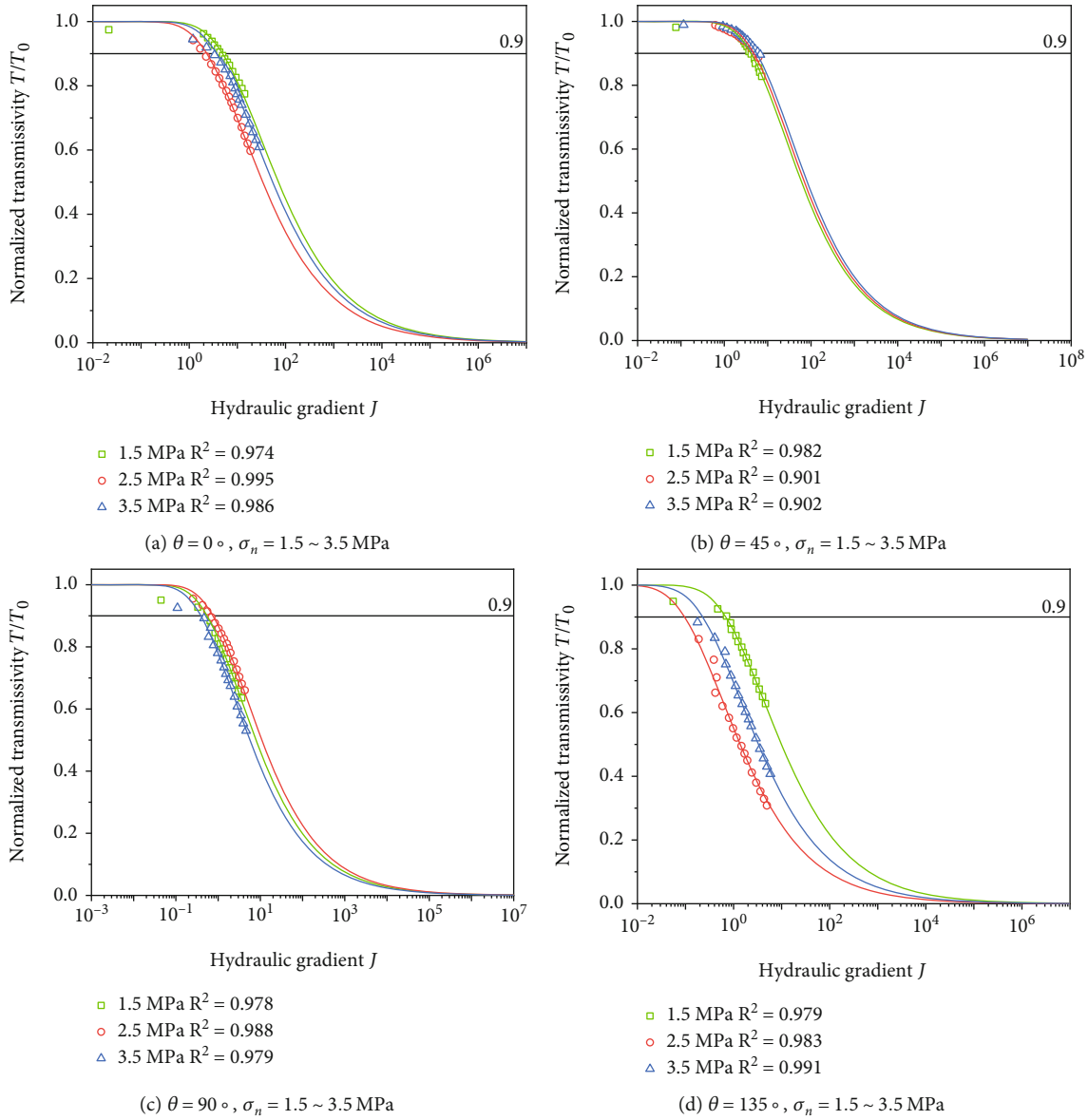


FIGURE 8: Relation between normalized transmissivity T/T_0 and hydraulic gradient J when confining pressure $\sigma_n = 1.5$ MPa, 2.5 MPa, and 3.5 MPa.

We take $T/T_0 = 0.9$ as a reference value, which means the proportion of nonlinear flow will account for 10%, and the fluid will change from a linear flow regime to a nonlinear flow regime. When $u_s = 2$ mm, the J of the samples with 0° and 45° angles is 4.73 and 3.85 when reaching $T/T_0 = 0.9$, which is significantly larger than that of the samples with 90° and 135° angles ($J = 0.53$ and 0.71). This is because with the increment of the cutting angle, the corresponding fractures are rougher when the shear displacement is 2 mm, and there are more contacts in the fracture. The flow rate Q required for the fluid to enter the nonlinear flow stage is smaller; therefore, the required critical hydraulic gradient J_c is smaller. It is worth noting that as shear advances, the J_c of the fracture with a cutting angle of 90° becomes larger when $T/T_0 = 0.9$, which indicates that the fracture is obviously affected by shear displacement. This results in a larger

void space and less contacts in the fracture and makes it more difficult for the fractures to enter the nonlinear flow stage. Therefore, a larger J is required to get the critical value. However, for other fractures such as the fracture with a cutting angle of 0° , the J_c decreases with the increase of shear displacement, which indicates that the seepage characteristics of fractured rock mass under different cutting angles are obviously different.

Figure 10 shows the variation characteristics of T/T_0 with Reynolds' coefficient of fractures with different cutting angles under different shear displacements. The Re_c of the fracture with a cutting angle of 90° is different from that of other samples. When the $u_s = 2$ mm, 3 mm, and 4 mm, the corresponding Re_c is 6.52, 28.73, and 32.1. This shows that with the increase of shear displacement, the void space is larger, and Re_c is larger. In contrast, for other fractures such

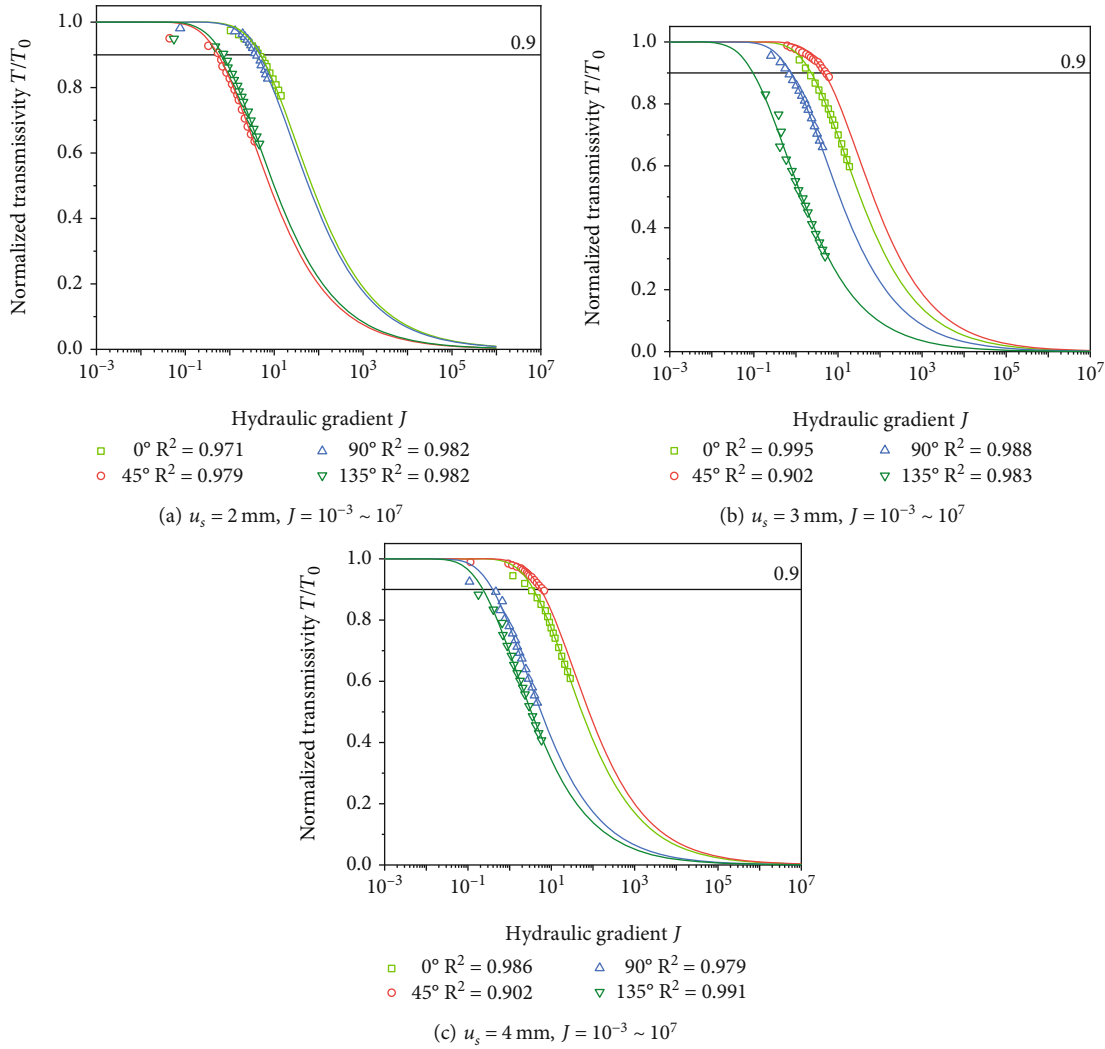


FIGURE 9: Evolution of normalized transmissivity T/T_0 under confining pressures and angles with varying hydraulic gradient J and shear displacement u_s .

as the fracture with a cutting angle of 0° , when $u_s = 2 \text{ mm}$, 3 mm , and 4 mm , the corresponding Re_c continuously decreases, which is different from the fracture with 90° . This shows that J and Re_c of the fracture that changes from linear flow regime to nonlinear flow regime under different cutting angles have different variation characteristics, depending on the geometric characteristics of fracture surfaces.

3.3. Effect of Coring Directions with Confining Pressures. Figure 11(a) compares Re_c contours for samples of different drilling angles under different confining pressures. The variations in Re_c along different drilling angles are significantly obvious. It is fully explained that the Re_c of the same rough fracture surface are also anisotropic. When the confining pressure is large (e.g., 2.5 MPa and 3.5 MPa), the difference between Re_c of samples with different drilling angles is small. This shows that when the confining pressure is large, the effect of anisotropy on Re_c is much greater than that of confining pressure. Figure 11(b) compares J_c contours for samples of different drilling angles under different confining pressures. When the confining pressure is small (e.g.,

1.5 MPa and 2.5 MPa), the difference between J_c of samples with different drill angles is relatively small. This shows that when the confining pressure is small, the effect of anisotropy on J_c is much greater than that of confining pressure.

Figure 12(a) compares Re_c contours for samples of different drilling angles with different u_s . The variations in Re_c along different drilling angles are significantly obvious. It is proved that the Re_c of the same rough fracture surface are anisotropic on the other hand. When u_s is large (e.g., 3 mm and 4 mm), the difference between Re_c of samples with different drilling angles is relatively small. This shows that when u_s is large, the effect of anisotropy on Re_c is much greater than that of u_s . Figure 12(b) compares J_c contours for samples of different drilling angles under different u_s . The variations in J_c along different drilling angles are significantly obvious. It is further indicated that the J_c of the same rough fracture surface is anisotropic. Regardless of the value of u_s , the difference between J_c is very obvious. When the confining pressure is small (e.g., 1.5 MPa and 2.5 MPa), the difference between J_c of samples with different drill angles is relatively small. This shows that when the

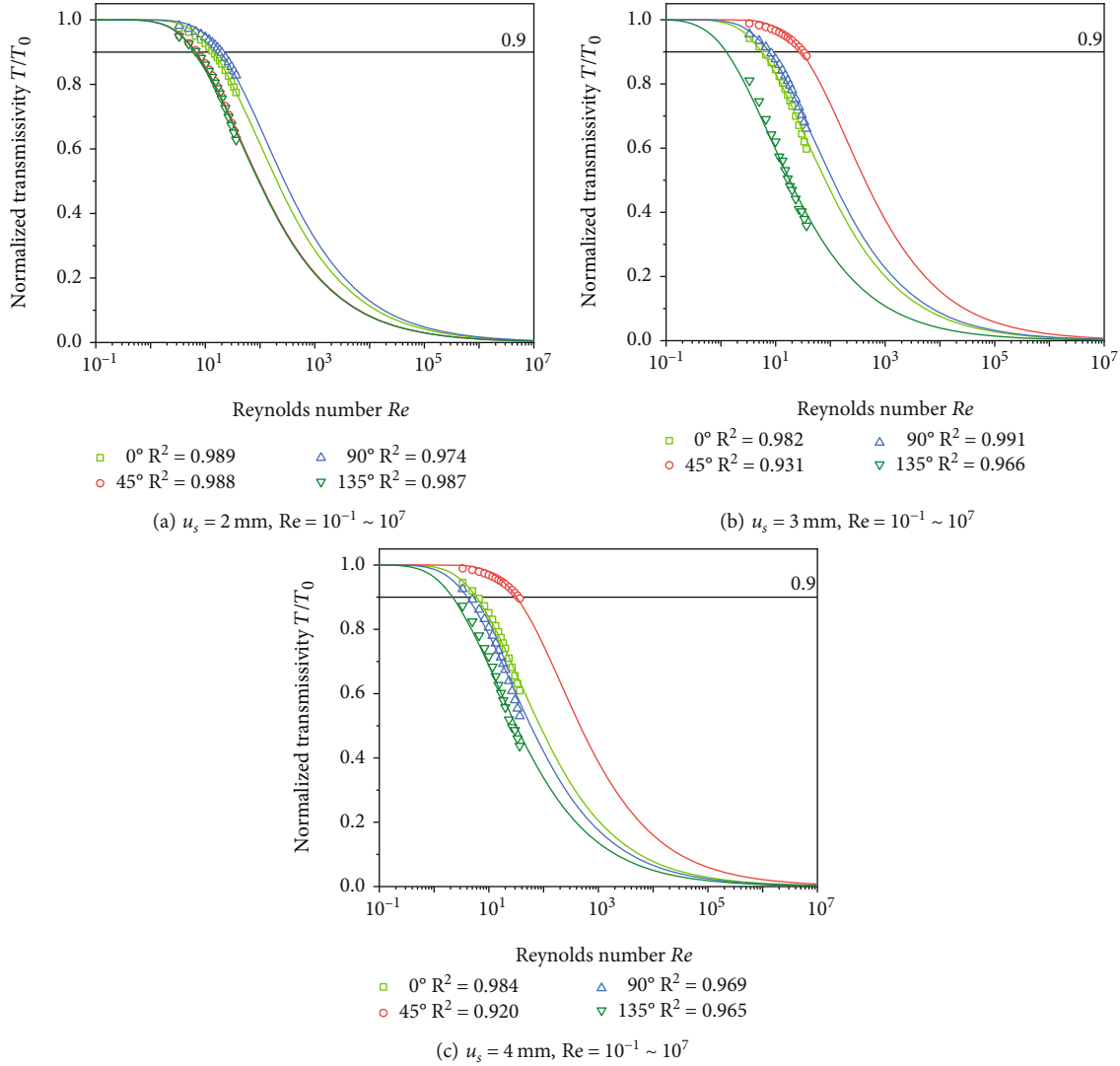


FIGURE 10: Evolution of normalized transmissivity T/T_0 under confining pressures and angles with varying Reynolds' number Re and shear displacement u_s .

confining pressure is small, the effect of anisotropy on J_c is much greater than that of confining pressure. So, anisotropy is important for the hydraulic properties of fractured rock masses.

4. Conclusions

To consider the anisotropic properties of rough-walled rock fracture, four cylindrical sandstone samples were extracted from the original rectangular sample with a rough-walled fracture. A series of seepage tests were carried out to investigate the hydraulic properties of cylindrical sandstone samples with different shear displacements (u_s) under different confining pressures (σ_n).

The results show that the apparent transmissivity (T) decreases with the increment of Reynolds' number (Re), and the decreasing rate gradually weakened, which confirmed the existence of flow nonlinearity in fractures. As the hydraulic gradient (J) increases, the normalized trans-

missivity (T/T_0) decreases. The variations in T/T_0 with J can be divided into three stages. When J is small, T/T_0 approximately holds a constant value of 1.0; thus, the fluid flow is within the linear regime. Then, with the continuous increase of J , T/T_0 decreases, and the reduction rate first increases and then decreases. When $u_s = 2 \text{ mm}$, 3 mm , and 4 mm , the values of critical Reynolds' number (Re_c) are 6.52, 28.73, and 32.1, respectively. This shows that with the increase in u_s , the void space is larger, and Re_c is larger. In contrast, for other fractures such as the fracture with a cutting angle of 0° , when $u_s = 2 \text{ mm}$, 3 mm , and 4 mm , the Re_c continuously decreases, which is different with the fracture with 90° . This shows that J and Re_c of the fracture that changes from linear flow regime to nonlinear flow regime under different cutting angles have different variation characteristics, depending on the geometric characteristics of the fracture surface. The variations in Re_c and J along different drilling angles are significantly obvious. It is fully explained that the Re_c and J of the same rough

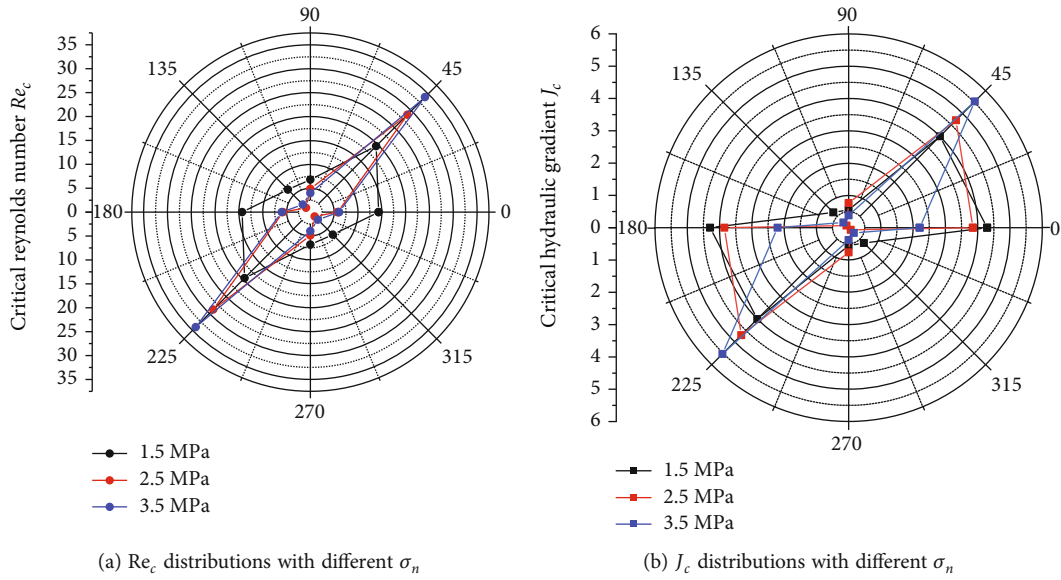


FIGURE 11: The distributions of critical Reynolds' number Re_c and critical hydraulic gradient J_c in different directions with different confining pressures σ_n .

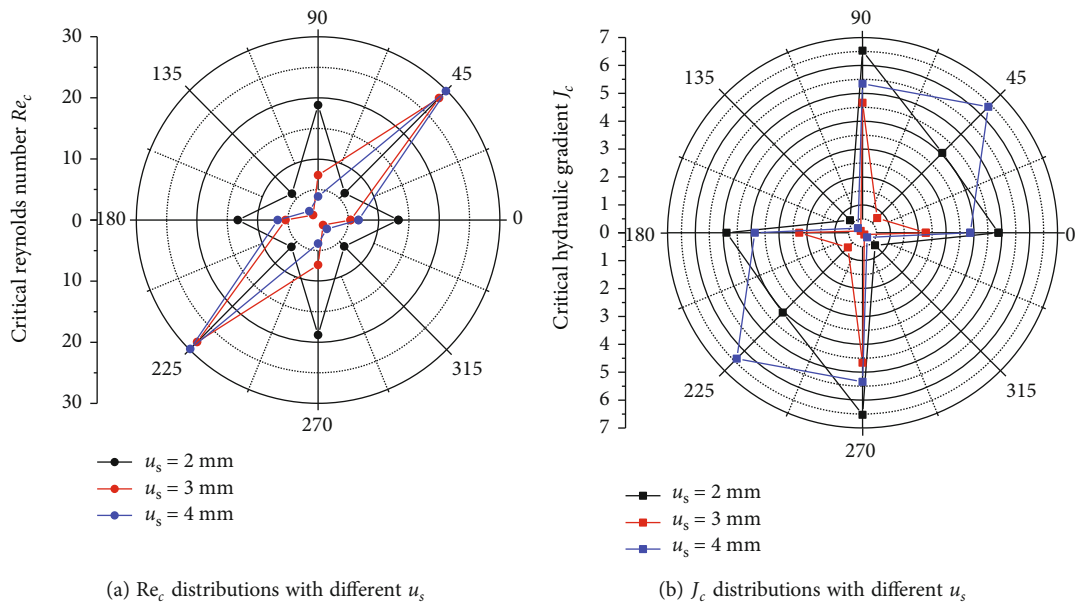


FIGURE 12: The distributions of critical Reynolds' number Re_c and critical hydraulic gradient J_c in different directions with different shear displacements u_s .

fracture surface are also anisotropic. When the confining pressure is large (e.g., 2.5 MPa and 3.5 MPa), the difference between Re_c of samples with different drilling angles is small. This shows that when the confining pressure is large, the effect of anisotropy on Re_c is much greater than that of confining pressure.

The permeability of fractures is several times larger than that of the matrix, and the connected fractures/fracture networks provide the dominant flow paths for fluid through hard or crystalline rocks during the shearing process. In the future work, we will investigate the mechanisms of opening/closure of fractures induced by shear/normal stresses

and clarify the separate roles of fractures and matrix on permeability during shearing.

Data Availability

The data can be obtained by contacting the author after the manuscript is accepted.

Conflicts of Interest

The authors declare that they have no conflict of interest.

Acknowledgments

This study has been partially funded by the Natural Science Foundation of China, China (Grant no. 51879105). These supports are gratefully acknowledged.

References

- [1] A. Baghbanan and L. Jing, "Hydraulic properties of fractured rock masses with correlated fracture length and aperture," *International Journal of Rock Mechanics and Mining Sciences*, vol. 44, no. 5, pp. 704–719, 2007.
- [2] R. Liu, B. Li, and Y. Jiang, "A fractal model based on a new governing equation of fluid flow in fractures for characterizing hydraulic properties of rock fracture networks," *Computers and Geotechnics*, vol. 75, pp. 57–68, 2016.
- [3] K. B. Min, L. Jing, and O. Stephansson, "Determining the equivalent permeability tensor for fractured rock masses using a stochastic REV approach: method and application to the field data from Sellafeld, UK," *Hydrogeology Journal*, vol. 12, no. 5, pp. 497–510, 2004.
- [4] C. Müller, S. Siegesmund, and P. Blum, "Evaluation of the representative elementary volume (REV) of a fractured geothermal sandstone reservoir," *Environmental Earth Sciences*, vol. 61, no. 8, pp. 1713–1724, 2010.
- [5] M. Wang, P. Kulatilake, J. Um, and J. Narvaiz, "Estimation of REV size and three-dimensional hydraulic conductivity tensor for a fractured rock mass through a single well packer test and discrete fracture fluid flow modeling," *International Journal of Rock Mechanics and Mining Sciences*, vol. 39, no. 7, pp. 887–904, 2002.
- [6] J. Song, M. Dong, S. Koltuk, H. Hu, L. Zhang, and R. Azzam, "Hydro-mechanically coupled finite-element analysis of the stability of a fractured-rock slope using the equivalent continuum approach: a case study of planned reservoir banks in Blaubeuren, Germany," *Hydrogeology Journal*, vol. 26, no. 3, pp. 803–817, 2018.
- [7] W. Xu, Y. Zhang, X. Li et al., "Extraction and statistics of discontinuity orientation and trace length from typical fractured rock mass: a case study of the Xinchang underground research laboratory site, China," *Engineering Geology*, vol. 269, article 105553, 2020.
- [8] L. Jing, "A review of techniques, advances and outstanding issues in numerical modelling for rock mechanics and rock engineering," *International Journal of Rock Mechanics and Mining Sciences*, vol. 40, no. 3, pp. 283–353, 2003.
- [9] Y. Chen, S. Hu, R. Hu, and C. Zhou, "Estimating hydraulic conductivity of fractured rocks from high-pressure packer tests with an Izbash's law-based empirical model," *Water Resources Research*, vol. 51, no. 4, pp. 2096–2118, 2015.
- [10] Y. He, Z. Zhu, W. Lu, Y. Tian, X. Xie, and S. Wang, "Experimental study on seepage anisotropy of a hexagonal columnar jointed rock mass," *Shock and Vibration*, vol. 2021, Article ID 6661741, 15 pages, 2021.
- [11] N. Huang, Y. Jiang, B. Li, and R. Liu, "A numerical method for simulating fluid flow through 3-D fracture networks," *Journal of Natural Gas Science and Engineering*, vol. 33, pp. 1271–1281, 2016.
- [12] B. Kong and S. Chen, "Numerical simulation of fluid flow and sensitivity analysis in rough-wall fractures," *Journal of Petroleum Science and Engineering*, vol. 168, pp. 546–561, 2018.
- [13] A. Lavrov, "Comparison of symmetric and asymmetric schemes with arithmetic and harmonic averaging for fracture flow on Cartesian grids," *Transport in Porous Media*, vol. 142, no. 3, pp. 585–597, 2022.
- [14] L. Zou, L. Jing, and V. Cvetkovic, "Roughness decomposition and nonlinear fluid flow in a single rock fracture," *International Journal of Rock Mechanics and Mining Sciences*, vol. 75, pp. 102–118, 2015.
- [15] Y. B. Gong, M. Sedghi, and M. Piri, "Two-phase relative permeability of rough-walled fractures: a dynamic pore-scale modeling of the effects of aperture geometry," *Water Resources Research*, vol. 57, no. 12, article e2021WR030104, 2021.
- [16] Y. B. Gong, M. Sedghi, and M. Piri, "Dynamic pore-scale modeling of residual trapping following imbibition in a rough-walled fracture," *Transport in Porous Media*, vol. 140, no. 1, pp. 143–179, 2021.
- [17] M. Ahmadi, A. D. Taleghani, and C. M. Sayers, "The effects of roughness and offset on fracture compliance ratio," *Geophysical Journal International*, vol. 205, no. 1, pp. 454–463, 2016.
- [18] A. Cardona, T. Finkbeiner, and J. C. Santamarina, "Natural rock fractures: from aperture to fluid flow," *Rock Mechanics and Rock Engineering*, vol. 54, no. 11, pp. 5827–5844, 2021.
- [19] F. Chen, H. Yu, Y. Yang, and D. Wu, "Influences of roughness sampling interval and anisotropy on shear failure mechanism of rock joint surface," *Energies*, vol. 14, no. 21, p. 6902, 2021.
- [20] P. S. Lang, A. Paluszny, M. Nejati, and R. W. Zimmerman, "Relationship between the orientation of maximum permeability and intermediate principal stress in fractured rocks," *Water Resources Research*, vol. 54, no. 11, pp. 8734–8755, 2018.
- [21] R. Liu, M. He, N. Huang, Y. Jiang, and L. Yu, "Three-dimensional double-rough-walled modeling of fluid flow through self-affine shear fractures," *Journal of Rock Mechanics and Geotechnical Engineering*, vol. 12, no. 1, pp. 41–49, 2020.
- [22] R. Liu, N. Huang, Y. Jiang, H. Jing, and L. Yu, "A numerical study of shear-induced evolutions of geometric and hydraulic properties of self-affine rough-walled rock fractures," *International Journal of Rock Mechanics and Mining Sciences*, vol. 127, article 104211, 2020.
- [23] Y. Song, B. Liu, H. Liu, X. Shi, D. Ren, and M. Yu, "A method to obtain artificial sandstone joint specimens for the description of permeability anisotropy-based joint shear deformation," *Geomechanics and Geophysics for Geo-Energy and Geo-Resources*, vol. 7, no. 2, pp. 1–19, 2021.
- [24] H. Kim, J. Inoue, and H. Horii, "Flow analysis of jointed rock masses based on excavation-induced transmissivity change of rough joints," *International Journal of Rock Mechanics and Mining Sciences*, vol. 41, pp. 959–974, 2004.
- [25] ISRM, "Rock characterization, testing and monitoring-ISRM suggested methods," in *Suggested methods for the quantitative description of discontinuities in rock masses*, E. T. Brown, Ed., pp. 3–52, E. T. Brown, Pergamon, 1981.
- [26] N. Huang, R. Liu, Y. Jiang, B. Li, and L. Yu, "Effects of fracture surface roughness and shear displacement on geometrical and hydraulic properties of three-dimensional crossed rock fracture models," *Advances in Water Resources*, vol. 113, pp. 30–41, 2018.
- [27] R. W. Zimmerman, A. Al-Yaarubi, C. C. Pain, and C. A. Grattoni, "Non-linear regimes of fluid flow in rock fractures," *International Journal of Rock Mechanics and Mining Sciences*, vol. 41, no. 3, pp. 163–169, 2004.

- [28] J. Q. Zhou, S. H. Hu, S. Fang, Y. F. Chen, and C. B. Zhou, "Nonlinear flow behavior at low Reynolds numbers through rough-walled fractures subjected to normal compressive loading," *International Journal of Rock Mechanics and Mining Sciences*, vol. 80, pp. 202–218, 2015.
- [29] G. Rong, J. Yang, L. Cheng, and C. Zhou, "Laboratory investigation of nonlinear flow characteristics in rough fractures during shear process," *Journal of Hydrology*, vol. 541, pp. 1385–1394, 2016.
- [30] Z. Zhang and J. Nemeik, "Fluid flow regimes and nonlinear flow characteristics in deformable rock fractures," *Journal of Hydrology*, vol. 477, no. 1, pp. 139–151, 2013.
- [31] Q. Yin, R. C. Liu, H. W. Jing, H. J. Su, L. Y. Yu, and L. X. He, "Experimental study of nonlinear flow behaviors through fractured rock samples after high-temperature exposure," *Rock Mechanics and Rock Engineering*, vol. 52, no. 9, pp. 2963–2983, 2019.
- [32] Q. Yin, H. W. Jing, G. W. Ma, H. J. Su, and R. C. Liu, "Investigating the roles of included angle and loading condition on the critical hydraulic gradient of real rock fracture networks," *Rock Mechanics and Rock Engineering*, vol. 51, no. 10, pp. 3167–3177, 2018.

Research Article

Stress Sensitivity of Proppant-Containing Fractures and Its Influence on Gas Well Productivity

Hao Chen ^{1,2}, Jianfei Wei,¹ Hanlie Cheng ¹, Qiang Qin ¹, Ying Chen,³
and Linqiang Zhang⁴

¹COSL-EXPRO Testing Services (Tianjin) Co., Ltd., Tianjin 300457, China

²Unconventional Oil and Natural Gas Institute, China University of Petroleum, Beijing 102249, China

³Engineering Company, Offshore Oil Engineering Co., Ltd., Tianjin 300451, China

⁴China United Coalbed Methane Co., Ltd., Beijing 100011, China

Correspondence should be addressed to Hanlie Cheng; chenghl@cosl-expro.com

Received 8 December 2022; Revised 21 April 2023; Accepted 26 April 2023; Published 4 May 2023

Academic Editor: Bao Jia

Copyright © 2023 Hao Chen et al. This is an open access article distributed under the Creative Commons Attribution License, which permits unrestricted use, distribution, and reproduction in any medium, provided the original work is properly cited.

Formation pressure gradually decreases with fracturing fluid flowback and gas production. Due to the stress sensitivity of the fractures, the permeability of the artificial fractures after fracturing becomes lower, which significantly affects gas well productivity. This paper focuses on two questions: (1) the stress sensitivity of proppant-containing fractures with different roughness and (2) tight gas well productivity considering stress sensitivity. Two types of artificial fracture samples, smooth and rough, are prepared and filled with different proppant concentrations. Then, the changing confining pressure method is used to quantify sample stress sensitivity. On this basis, the productivity equation for the fractured well with finite conductivity that considers fracture and matrix stress sensitivity is derived, and the influence of stress sensitivity on productivity is discussed. The results show that proppant concentration and fracture surface roughness will significantly affect fracture permeability and stress sensitivity; with increasing proppant concentration, fracture permeability increases, stress sensitivity decreases, and well productivity increases; under the same proppant concentration, the stress sensitivity is lower and the gas production is higher for smooth fracture; and when the artificial fracture changes from no proppant to proppant, the productivity of the fracturing well is improved the most.

1. Introduction

Since global oil and gas consumption grows continuously, conventional oil and gas development alone cannot meet social needs [1]. Therefore, unconventional oil and gas reservoirs, which cannot be developed conventionally, are receiving more and more attention [2, 3]. In China, unconventional oil and gas resources are widely distributed in Sichuan, Songliao, Ordos Junggar, and other basins, offering considerable development potential and broad prospects [4–7]. However, unconventional reservoirs have extremely low porosity and permeability, which requires massive hydraulic fracturing for effective development [8, 9]. During hydraulic fracturing, artificial fractures are formed as large-scale fracturing fluid enters the formation. Oil and gas well

production is strongly affected by these fractures since they are the main channels for reservoir fluid to enter the wellbore after fracturing [10]. With the fracturing fluid flowback and well production, the formation pressure gradually decreases, and the effective stress of the reservoir increases. Due to the stress sensitivity of fractures and reservoir matrix, permeability and fracture conductivity are drastically reduced, resulting in irreversible permeability loss and seriously affecting well productivity [11, 12].

Many researchers have studied reservoir stress sensitivity and oil and gas well productivity, establishing power law, and exponential and polynomial relationships between permeability and stress sensitivity [13–16]. Zhang et al. investigated the influencing factors and control mechanisms of shale stress sensitivity through permeability testing, rock

physical property analysis, and the dual pore medium stress sensitivity model [17, 18]. Rahman and Rahman investigated the interaction between induced and preexisting fractures in naturally fractured reservoirs by a numerical model using finite element analysis [19]. Sun et al. and Liu et al. studied volcanic rocks with different pore types and concluded that fractured volcanic gas reservoir rocks have strong stress-sensitive characteristics [20, 21]. Dong et al. examined the porosity and permeability of shale and sandstone, and the results showed that shale has stronger stress sensitivity than sandstone [22]. Xiao et al. studied the stress sensitivity of coal permeability and indicated that the coal shows significant anisotropic permeability and stress sensitivity due to the complex heterogeneity of the natural fracture system [23]. Yang et al. investigated the stress sensitivity of naturally fractured shale, and the results showed that the permeability evolution is consistent with the fracture aperture change during loading [24]. The above studies are focused on reservoir matrix and natural fractures, and there are fewer studies on artificial fracture permeability stress sensitivity.

Rock plate conductivity experiments are the primary method for studying the effects of closure pressure, proppant concentration, and proppant embedding on the permeability of artificial fractures [25–28]. Shaibu et al. conducted fracture conductivity experiments on saw-cut shale core, and the results showed that the main driver of fracture conductivity was induced fractures. However, permeability data were not obtained for this study, and large-scale cores could not be tested by a conventional permeameter [29]. However, the method has several drawbacks, including experimental complexity, large sample size, and preparation difficulties. Therefore, developing a more straightforward experimental method for studying artificial fractures is necessary. Wuguang et al. studied the effect of proppant on stress sensitivity by splitting shale cores and filling the fractures with proppant. This study concluded that proppant filling can effectively enhance the permeability of artificial fractures and reduce stress sensitivity, but this study did not quantify the proppant concentration [10]. Dong et al. and Lei et al. conducted experimental and theoretical research to investigate the effects of stress on fracture width and particle plugging in porous media. The study found that high stress causes increased pore blockage, and larger pores are less likely to experience particle plugging. Closure pressure reduction increases fracture width, as it decreases the contact force between fractured surfaces [30, 31]. Chen et al. used the Brazilian splitting method to create rough fractures and quantified the effect of proppant concentration on the stress sensitivity of artificial fractures by changing gas flow pressure and confining pressure, respectively. It concluded that the stress sensitivity of fractures obtained by the above two methods is not much different at low proppant concentrations, and the test methods significantly affect stress sensitivity at high proppant concentrations [32]. Nevertheless, it did not study the effect of fracture roughness on stress sensitivity.

The effect of stress sensitivity on production has been studied in depth by many scholars. Bo et al. derived a production prediction method considering stress sensitivity

and threshold pressure gradient based on the dual-porosity theory model, and the results show that two parameters must be considered in tight gas reservoirs [33]. Jiang et al. established a coupled matrix-fracture fluid flow model and investigated different stress-sensitive effects in different subsystems. This study concluded that the influence of stress sensitivity in fractures depends on the properties and location of the fractures [34]. Xinli conducted stress sensitivity experiments on sandstone containing microfractures and further investigated its effect on productivity, which indicated that the stress sensitivity of sandstone containing microfractures had little effect on oil production [35]. Liu et al. studied the stress sensitivity of low permeability reservoirs and its impact on oil and gas development through experiments and theoretical derivations and concluded that the lower the permeability and the faster the loading rate, the higher the permanent damage rate; the stronger the heterogeneity, the greater the productivity is affected by stress sensitivity [36]. The above studies of well production either did not conduct stress sensitivity experiments or only considered matrix stress sensitivity.

In this research, core-scale smooth and rough artificial fracture samples were prepared by wire cutting and splitting, respectively. Then, the samples were filled with different proppant concentrations. The influence of proppant concentration and fracture surface roughness on permeability and stress sensitivity was investigated by a conventional gas-measured permeability apparatus. Furthermore, the productivity equation of fractured gas wells considering matrix and artificial fracture stress sensitivity is derived to study the effect of stress sensitivity on well productivity. The objective of this study is to introduce a practical approach to conducting core-scale fracturing experiments, examine the stress sensitivity of fractures containing proppant, and evaluate the production capacity of gas wells in various types of fractures. This study helps to understand the flow of geofluids in fractures after fracturing and provides a basis for optimizing hydraulic fracture design and fracture fluid flow-back procedures.

2. Experimental Method

2.1. Sample Preparation. In this study, samples were collected from the sedimentary pyroclastic rock of the Lower Cretaceous Yingcheng Formation in Songliao Basin, northeastern China. The logging data indicates that the porosity of this formation is 10.78% and the permeability is $0.19 \times 10^{-3} \mu\text{m}^2$. In order to study the fracture surface with different roughness, wire cutting and splitting methods were used to make artificial fractures. Artificial fractures with smooth surfaces can be obtained by wire cutting, as shown in Figure 1(a), and artificial fractures with rough surfaces can be obtained by splitting, as shown in Figure 1(b).

The proppant used in this experiment was ceramic granules with a mesh size of 40/70 and an apparent density of 1570 kg/m^3 . According to the designed proppant concentration, the theoretical fracture width and proppant mass were calculated. The cores were prepped with theoretical fracture widths, the sample side was taped tightly, and then one side

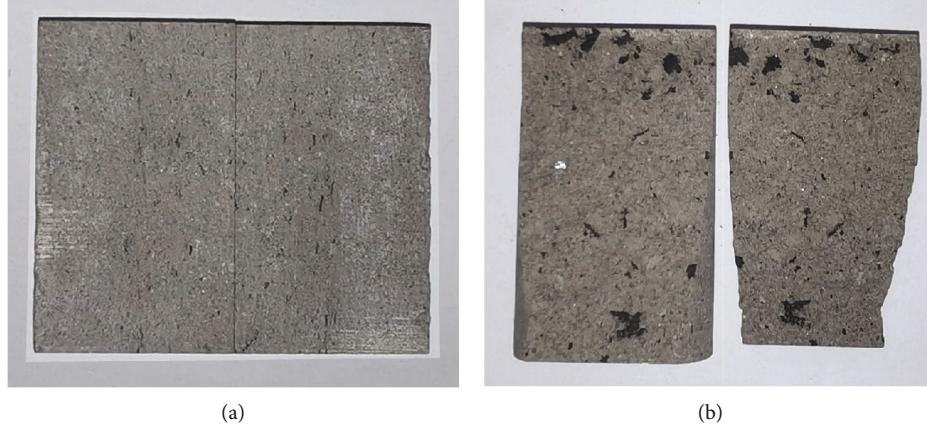


FIGURE 1: Experimental materials: (a) smooth fracture sample; (b) rough fracture sample.

end face was sealed with gauze. After that, the proppant was placed in fracture, and another side end face was sealed with gauze. At last, the actual width and proppant concentration were calculated by the actual proppant addition mass by the following formulas:

$$c_p = \frac{m_{\text{prop}}}{dL}, \quad (1)$$

$$w = \frac{c_p}{\rho_{\text{prop}}}, \quad (2)$$

where c_p is proppant concentration, kg/m^2 ; m_{prop} is proppant mass, kg ; d and L are the diameter and length of the sample, m ; w is fracture width, m ; and ρ_{prop} is proppant apparent density, kg/m^3 .

This experiment consisted of 4 smooth fracture samples and 2 rough fracture samples, with 1 nonfractured matrix sample used as a comparison. The basic parameters of the samples are shown in Table 1.

2.2. Experimental Method and Procedure. In this study, a gas-measured permeability apparatus was employed to investigate the stress sensitivity of artificial fracture. The test is conducted by changing confining pressure, and the test fluid is nitrogen with 99.9% purity. Following the requirements of SY/T 5358-2010 Formation damage evaluation by flow test, the specific experimental procedure is as follows:

- (1) *Basic Parameter Testing.* Dry the cores and measure the length, diameter, and mass of the samples
- (2) *Artificial Fracture Preparing.* Smooth surfaces can be obtained by wire cutting, and rough fractures are prepared by the splitting method. Dry and weigh the samples again
- (3) *Proppant Filling.* Fill the fractures with proppant as designed and then calculate the proppant concentration based on the actual mass
- (4) *Permeability Testing.* The permeability tests are performed with a constant gas flow pressure of

0.05 MPa and confining pressure of 2, 5, 9, 15, 20, 25, and 30 MPa. During the test, each designed confining pressure is maintained for more than 30 min, waiting for the flow to stabilize before metering begins. The following equation can calculate the gas permeability of the samples:

$$k_g = \frac{2q_0 p_0 \mu L}{A(p_1^2 - p_2^2)}, \quad (3)$$

where k_g is gas permeability, m^2 ; q_0 is gas flow rate, m^3/s ; μ is nitrogen viscosity, $\text{Pa}\cdot\text{s}$; A is the cross-sectional area of the sample, m^2 ; and p_1 and p_2 are the pressures at the inlet and outlet of the sample, respectively, Pa .

The effective stress of the sample was calculated by Terzaghi's effective stress equation:

$$P_e = P_c - P_f, \quad (4)$$

where P_e is effective stress, MPa ; P_c is confining pressure, MPa ; and P_f is gas flow pressure, MPa .

3. Experimental Results and Discussions

3.1. Permeability Variation Rules with Effective Stress. The permeability test results of the samples are shown in Table 2. By normalizing the permeability based on the permeability at effective stress of 2 MPa, the variation of normalized permeability with effective stress can be obtained (Figure 2). As can be seen in the figure, the permeability of the sample gradually decreases with increasing effective stress. As effective stress increases, the reduction rate of permeability decreases.

When effective stress was increased from 2 MPa to 15 MPa, samples 1[#]-7[#] lost 74.47%, 36.37%, 22.48%, 12.18%, 84.18%, 66.52%, and 55.61% of their permeability. Comparatively, only 17.28%, 22.50%, 22.29%, 9.67%, 14.40%, 26.67%, and 21.93% of permeability were lost in 15-30 MPa loading intervals for samples 1[#]-7[#]. This is because the initial proppant is loosely arranged and more easily compressed, leading to a reduction in fracture width

TABLE 1: Basic parameters of the samples.

Fracture type	Sample number	Length (mm)	Diameter (mm)	Fracture width (mm)	Proppant concentration (kg/m ²)
Smooth	1 [#]	50.02	24.36	0	0
	2 [#]	48.24	24.34	0.36	0.57
	3 [#]	49.75	24.36	0.66	1.04
	4	47.36	24.24	1.11	1.75
Rough	5 [#]	49.68	24.32	0	0
	6 [#]	48.97	24.34	0.34	0.54
Nonfractured	7 [#]	49.37	24.36	—	—

TABLE 2: Permeability test results of samples.

p_e (MPa)	Permeability ($\times 10^{-3} \mu\text{m}^2$)						
	1 [#]	2 [#]	Smooth fracture 3 [#]	4 [#]	Rough fracture 5 [#]	6 [#]	Matrix 7 [#]
2	241.42	1921.01	2418.00	3350.00	263.21	1413.00	0.187
5	180.62	1737.92	2290.00	3158.00	166.41	1181.25	0.165
9	148.06	1586.46	2032.00	3053.00	94.10	756.78	0.122
15	61.63	1222.27	1874.54	2942.00	41.63	473.13	0.083
20	35.41	999.94	1660.93	2805.00	12.00	283.69	0.062
25	23.04	876.56	1484.89	2681.00	6.20	201.61	0.051
30	19.91	790.13	1335.55	2618.00	3.74	96.26	0.042

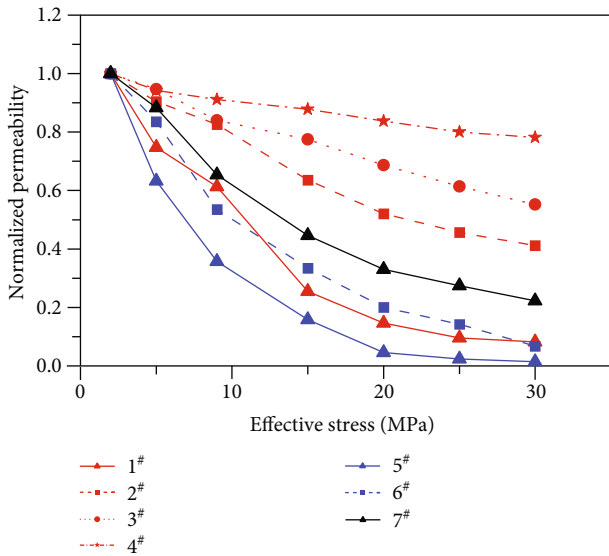


FIGURE 2: The relationship between normalized permeability and effective stress.

and a decrease in permeability. As the effective stress increases, the proppant arrangement becomes tighter and more difficult to compress, the fracture structure does not easily change, and the permeability decreases slower.

This result is similar in trend to those researches of Wuguang et al. and Chen et al. on shale [10, 32], but with a more significant permeability loss in the rough fracture samples of the same proppant concentration compared to Chen et al. There are two possible reasons for this: One is

that the sedimentary pyroclastic rock used in this experiment has a relatively low hardness compared to shale, which is more likely to deform when the effective stress is changed. Another is that laminae are developed in shale, and fractures are easily generated along the surface of laminates when the shale is split. The fracture surfaces of shale are smoother, and the proppant distribution will be relatively uniform, reducing the likelihood of permeability reduction caused by partial low proppant concentration.

3.2. *Effect of Proppant Concentration on Permeability and Stress Sensitivity.* The permeability is normalized based on the fracture samples without proppant, and the normalized permeability versus proppant concentration is represented in Figure 3. The normalized permeability is defined as follows:

$$k_{Nc_p} = \frac{k_i}{k_{i,c_p=0}}, \quad (5)$$

where k_{Nc_p} is normalized permeability, dimensionless; k_i is permeability under i effective pressure, m^2 ; and $k_{i,c_p=0}$ is permeability of fracture samples without proppant under i effective pressure, m^2 .

The figure shows that with an increase in the proppant concentration, whether in smooth or rough fracture samples, the permeability increases significantly under each effective stress. It shows that the higher the effective stress, the greater the normalized permeability. Taking the smooth fracture samples as an example, when the effective stress is 2 MPa, the permeability of the samples with sand concentrations of 0.57, 1.04, and 1.75 kg/m^2 is 7.96, 10.02, and 13.88

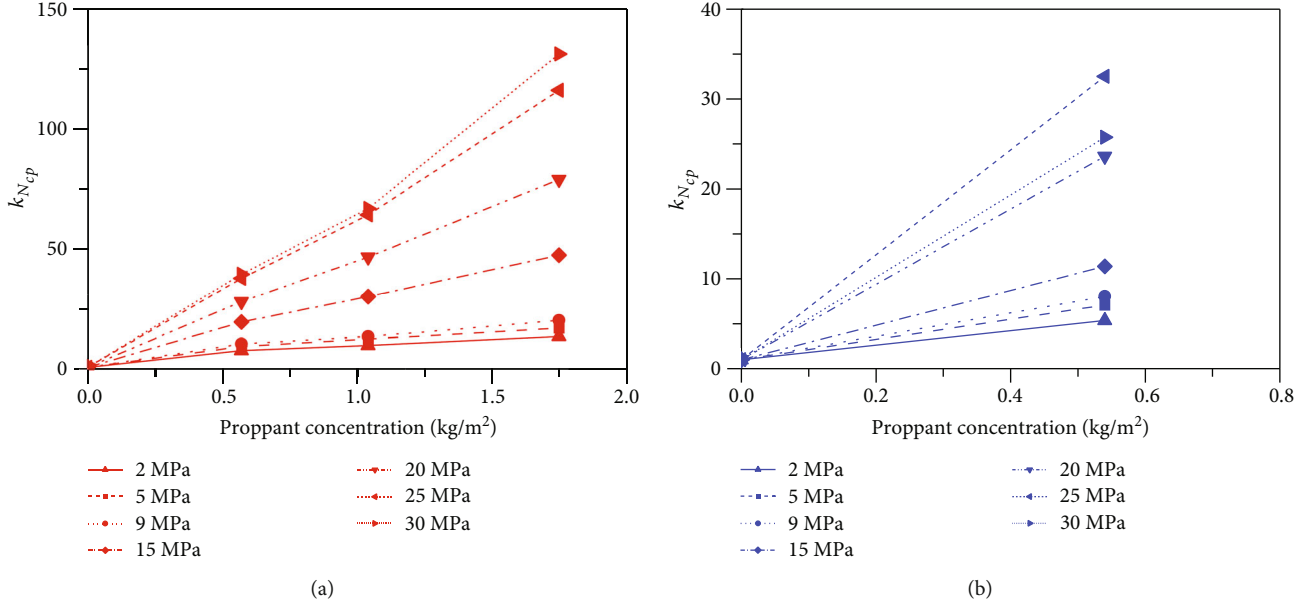


FIGURE 3: The relationship between normalized permeability (k_{Nc_p}) and proppant concentration: (a) smooth fracture; (b) rough fracture.

times greater than that of the sample without proppant. Comparatively, the values at 30 MPa are 39.69, 67.08, and 131.49 times. This is because as the effective stress increases, the arrangement of the proppant becomes tighter and tighter, the support capacity gradually increases, and the permeability increase multiplier becomes larger accordingly.

Based on Figure 3, a segmented linear fit is performed to determine each stage's slope separately. The slope is defined as the proppant efficiency, as shown in the following equation:

$$E_{prop} = \frac{\Delta k_{Nc_p}}{\Delta c_p}, \quad (6)$$

where E_{prop} is proppant efficiency, m^2/kg ; Δc_p is the proppant concentration change in a certain stage, kg/m^2 ; and Δk_{Nc_p} is normalized permeability change in the corresponding stage, dimensionless. The physical meaning of proppant efficiency is the multiple of the increase in permeability per unit proppant concentration at this stage.

As shown in the proppant efficiency statistical graph (Figure 4), the proppant efficiency is enhanced with increased effective stress in the same proppant concentration interval. Taking the proppant concentration interval of 0-0.57 kg/m^2 as an example, the proppant efficiency of this interval increased from 13.96 m^2/kg to 69.62 m^2/kg when the effective stress increased from 2 MPa to 30 MPa.

The proppant efficiency decreases with increasing proppant concentration under the same effective pressure. For the same effective stress of 2 MPa, the proppant efficiency was 13.96, 2.68, and 1.95 m^2/kg for proppant concentration intervals of 0-0.57, 0.57-1.04, and 1.04-1.75 kg/m^2 , respectively. It indicates that the lower the proppant concentration, the more effective it is to increase the proppant concentration in improving permeability.

During hydraulic fracturing, in addition to increasing the proppant amount, a proper proppant-adding method should be used to allow proppant to reach fractures with low proppant concentrations, such as the deep portion of the main fracture and the secondary fractures, as much as possible. Thus, the average proppant concentration of fractures is enhanced, and the permeability of fractures is greatly improved. The proppant efficiency for rough fractures is lower at 30 MPa than 25 MPa. This may be caused by the proppant starting embedding in the fracture surface during the effective stress interval between 25 and 30 MPa.

An exponential fitting is performed on the effective stress and permeability to obtain the sample's stress sensitivity coefficient. The fitting equation is given by

$$k = k_0 e^{-bp_e}, \quad (7)$$

where k and k_0 are permeability and initial permeability, respectively, $10^{-3} \mu m^2$, and b is the stress sensitivity coefficient, MPa^{-1} .

Since the permeability of the artificial fracture sample is much larger than the matrix permeability, the matrix permeability can be ignored for the artificial fracture sample. Therefore, the permeability of the sample in the experiment is regarded as the fracture permeability, and the stress sensitivity coefficient of the sample is considered to be the stress sensitivity coefficient of artificial fracture.

Figure 5 shows the stress sensitivity coefficient of each sample. In this experiment, the smooth fracture sample without proppant and the rough fracture samples reveal strong stress sensitivity. The matrix sample presents medium stress sensitivity, while the smooth fracture with proppant shows moderately weak to weak stress sensitivity with increasing proppant concentration. The stress sensitivity of rough and smooth fractures decreases with increasing

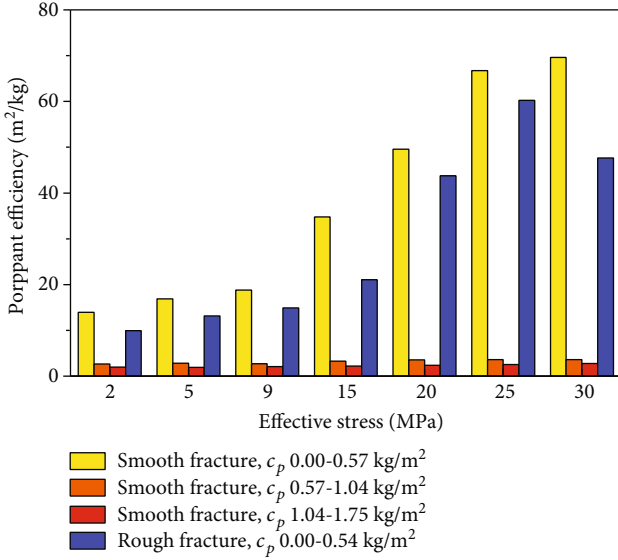


FIGURE 4: Statistical graph of proppant efficiency.

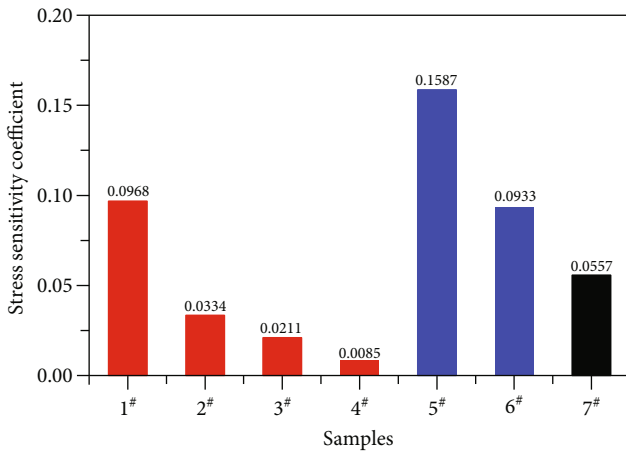


FIGURE 5: The stress sensitivity coefficient of samples.

proppant concentration. This is because a higher proppant concentration increases its ability to support fractures, making them more difficult to close.

3.3. Effect of Fracture Surface Roughness on Permeability and Stress Sensitivity. Figure 6 shows the variation curve of permeability with effective stress under differing fracture roughness. For cracks without proppant, there is no significant difference in permeability between smooth and rough fractures at low effective stress (≤ 5 MPa). As the effective stress increases, the permeability of rough fractures decreases more rapidly, and smooth fractures exhibit higher permeability than rough fractures under the same effective stress. It is possible that compared to the smooth fracture, the rough fracture may have a lower fracture closure due to the self-propping effect of rough surfaces under low pressure. Meanwhile, the rough fracture has a long infiltration length due to

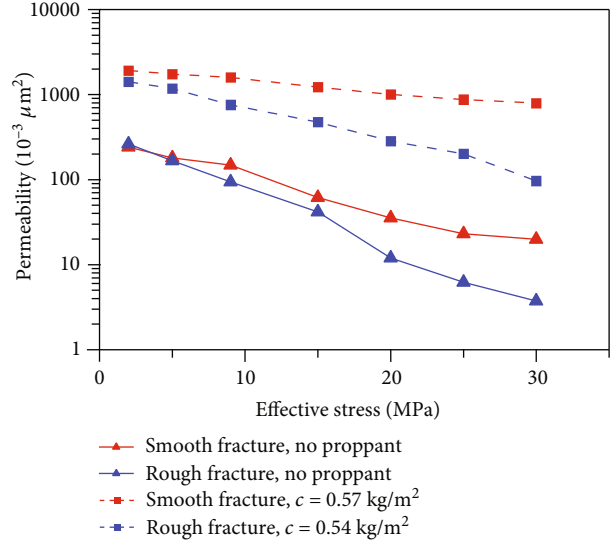


FIGURE 6: Variation of permeability with effective stress at different fracture surface roughness.

its high tortuosity. At low pressure, rough fractures are affected by the factors simultaneously, resulting in a permeability similar to smooth fractures. As the effective stress increases, the rough surfaces gradually compact, and the permeability is primarily affected by tortuosity, resulting in a lower permeability than the smooth fractures.

When proppant concentrations are about 0.55 kg/m², smooth fractures have higher permeability than rough fractures. This trend gradually increases with the increase of effective stress. It can be mainly attributed to the nonuniform distribution of proppant and relatively increased fracture surface area caused by the irregular surface of the rough fracture. The nonuniform distribution of proppant leads to more partial fracture closures, resulting in a decrease in overall permeability. The relatively increased surface of the rough fracture causes the proppant concentration to be lower than that of the smooth fracture, resulting in the rough cracks being insufficiently propped, resulting in a lower permeability. For the same reason, rough fracture exhibits higher stress sensitivity than smooth fracture at the same proppant concentration.

4. Fractured Well Productivity for Tight Gas considering Fracture and Matrix Stress Sensitivity

4.1. Derivation of the Fractured Gas Well Productivity Equation. The production of the fractured tight gas well is a coupled matrix and fracture flow process. Therefore, both the matrix and fracture stress sensitivity need to be considered. In addition, considering the fracture's flow resistance, a productivity equation for fractured wells considering fracture and matrix sensitivity is developed based on the formula for the production productivity equation for fractured wells with finite conductivity.

The equivalent well radius of finite conductivity fractures can be calculated as follows [37, 38]:

$$R_{we} = 2x_f e^{-[3/2+f(C_{FD})]}, \quad (8)$$

where R_{we} is the equivalent well radius, m; x_f is fracture half-length, m; and $f(C_{FD})$ is a function of the dimensionless fracture conductivity, and it can be expressed as follows [39, 40]:

$$f(C_{FD}) = \frac{1.65 - 0.328\mu + 0.116\mu^2}{1 + 0.18\mu + 0.064\mu^2 + 0.005\mu^3}, \quad (9)$$

$$\mu = \ln C_{FD}, \quad (10)$$

$$C_{FD} = \frac{k_f w_f}{k_m x_f}, \quad (11)$$

where C_{FD} is dimensionless fracture conductivity and k_f and k_m are fracture and matrix permeability, respectively, m^2 .

The permeability of fracture and matrix considering the stress sensitivity is calculated by

$$k_f = k_{fi} e^{-b_f(p_e - p_w)}, \quad (12)$$

$$k_m = k_{mi} e^{-b_m(p_e - \bar{p}_m)}, \quad (13)$$

where k_{fi} is initial permeability of fracture, m^2 ; b_f is the stress sensitivity coefficient of fracture, MPa^{-1} ; p_e is original formation pressure, MPa; p_w is bottom hole pressure, MPa; k_{mi} is initial permeability of matrix, m^2 ; b_m is the stress sensitivity coefficient of matrix, MPa^{-1} ; and \bar{p}_m is the average pressure of matrix, MPa. If the calculated fracture permeability is lower than the matrix permeability, the fracture is considered closed, and the fracture permeability is equal to the matrix permeability.

During the gas well production, the reservoir pressure distribution is given by the following equation:

$$\frac{dp}{dr} = \frac{p_e^2 - p_w^2}{\ln R_e/R_{we}} \frac{1}{2rp}. \quad (14)$$

And the average pressure of the matrix can be calculated by

$$\bar{p}_m = \frac{\int_{R_{we}}^{R_e} p \cdot 2\pi r dr}{\pi(R_e^2 - R_{we}^2)} = \frac{2 \int_{R_{we}}^{R_e} (p_e^2 - p_e^2 - p_w^2 / \ln R_e/R_{we} \ln R_e/r)^{0.5} r dr}{R_e^2 - R_{we}^2}. \quad (15)$$

As the average pressure of the matrix is also a function of the equivalent well diameter, the two parameters cannot be calculated directly, so the trial and error method is used instead. The calculation flow chart of equivalent well radius and average matrix pressure is shown in Figure 7. When the relative error ε between the trial and calculated values is less than 5%, the calculation is stopped, and the two parameters are output.

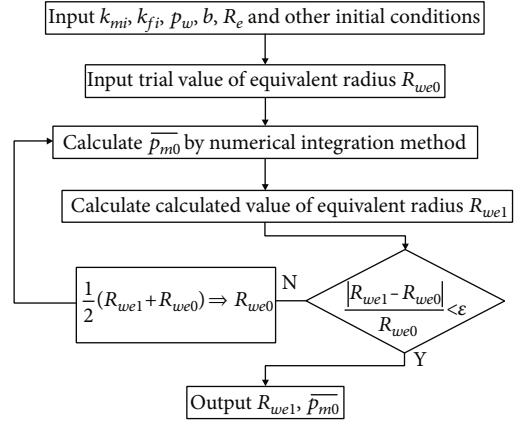


FIGURE 7: The calculation flow chart of equivalent well radius and matrix average pressure.

The fractured gas well productivity considering fracture and matrix stress sensitivity is

$$Q = \frac{\pi k_m h Z_{sc} T_{sc}}{\bar{\mu} \bar{Z}} \frac{p_e^2 - p_w^2}{p_{sc} T \ln R_e/R_{we}}, \quad (16)$$

where $\bar{\mu}$ is average gas viscosity, $\text{mPa}\cdot\text{s}$; \bar{Z} is the average gas deviation factor; Z_{sc} is the gas deviation factor in standard condition; T_{sc} is the gas temperature in standard condition, K; p_{sc} is the gas pressure in standard condition, MPa; and T is layer temperature, K.

4.2. Case Study. In the case analysis of this paper, the reservoir parameters are collected from well logging and testing data of the sampled well. The production layer properties of this well are as follows: the overburden pressure is 94.2 MPa, the formation pressure is 40 MPa, the initial permeability is $0.19 \times 10^{-3} \mu\text{m}^2$, the layer temperature is 120°C , and the reservoir effective thickness is 17.13 m. Based on the assumption that the supply radius is 300 meters, the fracture width is 5 millimeters, and the fracture half-length is 100 meters, the gas well production was calculated at the bottom hole pressure range of 40 to 30 MPa.

Table 3 shows the calculated productivity results of the fractured gas well, where Q is gas well productivity considering stress sensitivity, m^3/d ; Q' is gas well productivity without considering stress sensitivity, m^3/d ; and η is the productivity loss rate due to stress sensitivity, %. The defining equation is as follows:

$$\eta = \frac{Q' - Q}{Q'} \times 100\%. \quad (17)$$

According to Table 3, stress sensitivity significantly impacts fractured well productivity, and the productivity loss rate due to stress sensitivity increases as bottom hole pressure declines. For unproped rough fractures, the stress sensitivity can result in a productivity loss of more than 90%. As the bottom hole pressure decreases, the productivity of each fracture tends to increase gradually. Nevertheless, the productivity of unproped rough fractures ($5^\#$) decreases

TABLE 3: The calculated productivity results of fractured gas well.

Fracture type	Well productivity	p_w (MPa)					
		40	38	36	34	32	30
1 [#]	Q	0	2905	5271	7095	8373	9093
	Q'	0	6551	12632	18245	23389	28064
	η	—	55.66	58.27	61.11	64.20	67.60
2 [#]	Q	0	6666	12816	18471	23649	28368
	Q'	0	9299	18041	26231	33873	40970
	η	—	28.31	28.96	29.58	30.18	30.76
3 [#]	Q	0	7747	14945	21609	27754	33395
	Q'	0	9683	18819	27410	35460	42972
	η	—	20.00	20.59	21.17	21.73	22.29
4 [#]	Q	0	9346	18135	26373	34066	41220
	Q'	0	10212	19880	29005	37589	45633
	η	—	8.48	8.78	9.07	9.37	9.67
5 [#]	Q	0	1248	2190	2784	2970	2643
	Q'	0	6742	12889	18428	23337	27577
	η	—	81.49	83.01	84.89	87.27	90.42
6 [#]	Q	0	4239	7962	11173	13876	16070
	Q'	0	9009	17326	24951	31881	38112
	η	—	52.94	54.05	55.22	56.48	57.83

when the bottom hole pressure is reduced from 32 MPa to 30 MPa. This is because the infiltration power increased by the reduced bottom hole pressure is less than the resistance caused by stress sensitivity.

Smooth fractures have significantly higher productivity than rough fractures when proppant concentrations are the same. Unpropped smooth fracture is 3.44 times more productive than unpropped rough fracture at 30 MPa, and the value is 1.77 at a proppant concentration of 0.55 kg/m^2 . In the same fracture surface roughness, the gas well productivity increases with increasing proppant concentration; especially when the fracture goes from unpropping to propping, the productivity increases the most. At the bottom hole pressure of 30 MPa, the productivity of the unpropped smooth fracture (1[#]) is $9093 \text{ m}^3/\text{d}$. In comparison, the productivity of the smooth fracture (2[#]) with a proppant concentration of 0.57 kg/m^2 is $28368 \text{ m}^3/\text{d}$, a 3.12 times increase in productivity. And for rough fractures, productivity can increase by 6.08 times.

To summarize, during fracturing design, construction, and the subsequent formulation of the flowback strategy, as well as increasing the total proppant addition and increasing the average proppant concentration in the fractures, it will be important to target the fractures that cannot easily be propped, such as secondary fractures and deep parts of main fractures. With a certain proppant amount, the flowback pressure should be controlled, and the timing of flowback should be optimized to reduce the proppant backflow

to improve the overall proppant concentration in the fracture. During hydraulic fracturing, the construction process can be optimized by the sand slug addition method to make the proppant enter the deep part of the fracture as much as possible, and the proppant can be distributed more equally.

5. Conclusions

In this paper, the effects of proppant concentration and fracture surface roughness on permeability and stress sensitivity are investigated experimentally. The productivity equation of fractured gas well is derived to study the effect of stress sensitivity on productivity. The main conclusions are obtained as follows:

- (1) The proppant can effectively enhance permeability and reduce the stress sensitivity of artificial fracture. As proppant concentration increases, the fracture permeability increases, the fracture stress sensitivity decreases, and the proppant efficiency decreases. For the same increment in proppant concentration, the artificial fracture has the most significant enhancement in permeability from unpropped to propped
- (2) The roughness of the fracture surface can significantly affect fracture permeability and stress sensitivity. For unpropped fractures, the permeability of smooth fracture and rough fracture is similar under

low effective stress (≤ 5 MPa). For unpropped fractures under high effective stress (≥ 10 MPa) and propped fractures, the rough fractures have lower permeability and higher stress sensitivity than smooth fractures

- (3) The stress sensitivity dramatically impacts the productivity of fractured wells. Under the same proppant concentration, the stress sensitivity is lower, and the gas production is higher for smooth fractures. As proppant concentration increases, fracture permeability increases, stress sensitivity decreases, and gas well productivity increases. The most significant increase in fractured well productivity occurs when the artificial fracture changes from no proppant to proppant. During hydraulic fracturing, reasonable measures should be taken to distribute the proppant uniformly and to enhance the effective propping of the deep parts of the fractures

Data Availability

The figures and tables used to support the findings of this study are included in the article.

Conflicts of Interest

The authors declare that there is no conflict of interest regarding the publication of this paper.

Acknowledgments

The authors would like to sincerely thank those techniques which have contributed to this research.

References

- [1] W. H. Haider, "IPTC-19729-MS estimates of total oil & gas reserves in the world, future of oil and gas companies and smart investments by E & P companies in renewable energy sources for future energy needs," in *International Petroleum Technology Conference*, Dhahran, Saudi Arabia, 2020.
- [2] W. Hu, J. Bao, and B. Hu, "Trend and progress in global oil and gas exploration," *Petroleum Exploration and Development*, vol. 40, no. 4, pp. 439–443, 2013.
- [3] L. Zheng, P. Wei, Z. Zhang et al., "Joint exploration and development: a self-salvation road to sustainable development of unconventional oil and gas resources," *Natural Gas Industry B*, vol. 4, no. 6, pp. 477–490, 2017.
- [4] C. Jia, M. Zheng, and Y. Zhang, "Unconventional hydrocarbon resources in China and the prospect of exploration and development," *Petroleum Exploration and Development*, vol. 39, no. 2, pp. 139–146, 2012.
- [5] Z. Yang and C. Zou, "'Exploring petroleum inside source kitchen': connotation and prospects of source rock oil and gas," *Petroleum Exploration and Development*, vol. 46, no. 1, pp. 181–193, 2019.
- [6] H. Cheng, J. Wei, and Z. Cheng, "Study on sedimentary facies and reservoir characteristics of Paleogene sandstone in Yingmaili block, Tarim Basin," *Geofluids*, vol. 2022, Article ID 1445395, 14 pages, 2022.
- [7] J. Han, H. Cheng, Y. Shi, L. Wang, Y. Song, and W. Zhnag, "Connectivity analysis and application of fracture cave carbonate reservoir in Tazhong," *Science Technology and Engineering*, vol. 16, no. 5, pp. 147–152, 2016.
- [8] T. Guo, S. Zhang, Z. Qu, T. Zhou, Y. Xiao, and J. Gao, "Experimental study of hydraulic fracturing for shale by stimulated reservoir volume," *Fuel*, vol. 128, pp. 373–380, 2014.
- [9] C. Zou, D. Dong, S. Wang et al., "Geological characteristics and resource potential of shale gas in China," *Petroleum Exploration and Development*, vol. 37, no. 6, pp. 641–653, 2010.
- [10] L. Wuguang, B. Zhong, X. Zhang, Z. Hu, and L. Xie, "Evaluating method of the stress sensitivity for the artificial fracture in the shale," *Petroleum Geology & Oilfield Development in Daqing*, vol. 35, no. 3, pp. 159–164, 2016.
- [11] Z. Zhang, S. He, G. Liu, X. Guo, and S. Mo, "Pressure buildup behavior of vertically fractured wells with stress-sensitive conductivity," *Journal of Petroleum Science and Engineering*, vol. 122, pp. 48–55, 2014.
- [12] A. Reinicke, E. Rybacki, S. Stanchits, E. Huenges, and G. Dresen, "Hydraulic fracturing stimulation techniques and formation damage mechanisms— implications from laboratory testing of tight sandstone-proppant systems," *Chemie der Erde-Geochemistry-Interdisciplinary Journal for Chemical Problems of the Geosciences and Geoecology*, vol. 70, pp. 107–117, 2010.
- [13] V. S. Pathi, *Factors affecting the permeability of gas shales*, PhD diss., University of British Columbia, 1995.
- [14] G. R. L. Chalmers, D. J. K. Ross, and R. M. Bustin, "Geological controls on matrix permeability of Devonian Gas Shales in the Horn River and Liard basins, northeastern British Columbia, Canada," *International Journal of Coal Geology*, vol. 103, pp. 120–131, 2012.
- [15] H. Yuanzhi and W. Enzhi, "Experimental study on coefficient of sensitiveness between percolation rate and effective pressure for low permeability rock," *Chinese Journal of Rock Mechanics and Engineering*, vol. 26, no. 2, pp. 410–414, 2007.
- [16] Q. Lei, W. Xiong, C. Yuan, and Y. S. Wu, *Analysis of Stress Sensitivity and Its Influence on Oil Production from Tight Reservoirs - eScholarship*, Society of Petroleum Engineers, 2008.
- [17] R. Zhang, Z. Ning, F. Yang, H. Zhao, and Q. Wang, "A laboratory study of the porosity-permeability relationships of shale and sandstone under effective stress," *International Journal of Rock Mechanics and Mining Sciences*, vol. 81, pp. 19–27, 2016.
- [18] R. Zhang, *Effective stress law and stress dependent mechanism for the permeability of shale*, Doctoral thesis. China University of Petroleum, 2018.
- [19] M. M. Rahman and S. S. Rahman, "Fully coupled finite-element-based numerical model for investigation of interaction between an induced and a preexisting fracture in naturally fractured poroelastic reservoirs: fracture diversion, arrest, and breakout," *International Journal of Geomechanics*, vol. 13, no. 4, pp. 390–401, 2013.
- [20] J.-C. Sun, Y. Zheng-Ming, W. Guo-Qi, and Z. Xue-Min, "Characterization of stress-dependent permeability of volcanic gas reservoir of different types of pore structure," *Rock and Soil Mechanics*, vol. 33, 2012.
- [21] Z. Liu, J. Zhao, P. Kang, and J. Zhang, "An experimental study on simulation of stress sensitivity to production of volcanic gas from its reservoir," *Journal of the Geological Society of India*, vol. 86, no. 4, pp. 475–481, 2015.

- [22] J. J. Dong, J. Y. Hsu, W. J. Wu et al., "Stress-dependence of the permeability and porosity of sandstone and shale from TCDDP Hole-A," *International Journal of Rock Mechanics & Mining Sciences*, vol. 47, no. 7, pp. 1141–1157, 2010.
- [23] K. Xiao, Z. Zhang, R. Zhang et al., "Anisotropy of the effective porosity and stress sensitivity of coal permeability considering natural fractures," *Energy Reports*, vol. 7, pp. 3898–3910, 2021.
- [24] D. Yang, W. Wang, K. Li, W. Chen, J. Yang, and S. Wang, "Experimental investigation on the stress sensitivity of permeability in naturally fractured shale," *Environment and Earth Science*, vol. 78, no. 2, 2019.
- [25] T. Hou, S. Zhang, X. Ma et al., "Experimental and theoretical study of fracture conductivity with heterogeneous proppant placement," *Journal of Natural Gas Science and Engineering*, vol. 37, pp. 449–461, 2017.
- [26] M. Fan, Y. Han, J. McClure, and C. Chen, "Hydraulic fracture conductivity as a function of proppant concentration under various effective stresses: from partial monolayer to multilayer proppants," in *SPE/AAPG/SEG Unconventional Resources Technology Conference*, Austin, Texas, USA, 2017.
- [27] Y. Zhang, H. Ge, G. Liu et al., "Experimental study of fracturing fluid retention in rough fractures," *Geofluids*, vol. 2019, Article ID 2603296, 20 pages, 2019.
- [28] J. Wang, Y. Huang, F. Zhou, and X. Liang, "The influence of proppant breakage, embedding, and particle migration on fracture conductivity," *Journal of Petroleum Science and Engineering*, vol. 193, p. 107385, 2020.
- [29] R. Shaibu, B. Guo, P. B. Wortman, and J. Lee, "Stress-sensitivity of fracture conductivity of Tuscaloosa Marine Shale cores," *Journal of Petroleum Science and Engineering*, vol. 210, article 110042, 2022.
- [30] L. Dong, D. Wang, F. Li, X. Fu, and M. Wang, "Investigation of fracture width change under closure pressure in unconventional reservoir based on the Hertz contact theory," *Geofluids*, vol. 2021, Article ID 1268352, 6 pages, 2021.
- [31] G. Lei, S. Gu, L. Dong, Q. Liao, and L. Xue, "Particle plugging in porous media under stress dependence by Monte Carlo simulations," *Journal of Petroleum Science and Engineering*, vol. 207, article 109144, 2021.
- [32] H. Chen, T. Zhou, H. Fan, J. Zhang, and S. Yang, "Preparation method and stress sensitivity of core samples with hydraulic fractures in shale reservoirs," *Acta Petrolei Sinica*, vol. 41, no. 9, p. 1117, 2020.
- [33] N. Bo, X. Zuping, L. Xianshan et al., "Production prediction method of horizontal wells in tight gas reservoirs considering threshold pressure gradient and stress sensitivity," *Journal of Petroleum Science and Engineering*, vol. 187, article 106750, 2020.
- [34] L. Jiang, J. Liu, T. Liu, and D. Yang, "Semi-analytical modeling of transient pressure behaviour for a fractured vertical well with hydraulic/natural fracture networks by considering stress-sensitive effect," *Journal of Natural Gas Science and Engineering*, vol. 82, article 103477, 2020.
- [35] X. Xinli, "Stress sensitivity of low-permeability reservoir containing micro-fracture and its influence on productivity," *Special Oil & Gas Reservoirs*, vol. 22, no. 1, p. 4, 2015.
- [36] R. Liu, H. Liu, H. Zhang, Y. Tao, and M. Li, "Study of stress sensitivity and its influence on oil development in low permeability reservoir," *Chinese Journal of Rock Mechanics & Engineering*, vol. 30, pp. 2697–2702, 2011.
- [37] F. Zhang, S. Zhao, J. Qin, Y. Deng, W. Sun, and J. Yi, "Productivity of the horizontal well with finite-conductivity fractures," *Natural Gas Geoscience*, vol. 20, no. 5, 2009.
- [38] B. Meyer, R. Jacot, and A. Inc, *SPE 95941 Pseudosteady-State Analysis of Finite-Conductivity Vertical Fractures Presented an Approximate Analytical Mathematical Model for Predicting the Productivity Ratio Increase of Finite-Conductivity Fractures in Pseudosteady*, 2005.
- [39] M. Economides, R. Oligney, and P. Valkó, *Unified Fracture Design: Bridging the Gap between Theory and Practice*, Orsa Press, 2002.
- [40] M. K. Rahman, M. M. Rahman, and A. H. Joarder, "Analytical production modeling for hydraulically fractured gas reservoirs," *Petroleum Science and Technology*, vol. 25, no. 6, pp. 683–704, 2007.

Research Article

Characteristics and Gas-Bearing Properties of Yanchang Formation Shale Reservoirs in the Southern Ordos Basin

Zhendong Gao,¹ Yongdong Wang,¹ Xiaoyu Gu,² Hanlie Cheng ,³ and Nnamdi Puppe ⁴

¹Yanchang Oilfield Co., Ltd., Yan'an, Shaanxi 716000, China

²Laboratory of Advanced Stimulation Technology for Oil & Gas Reservoirs, Xi'an Shiyou University, Xi'an, Shanxi 710065, China

³School of Energy Resource, China University of Geosciences (Beijing), Beijing 434000, China

⁴The King's School, BP1560, Bujumbura, Burundi

Correspondence should be addressed to Nnamdi Puppe; nnamdi.puppe@ksu.edu.bi

Received 1 December 2022; Revised 26 December 2022; Accepted 31 March 2023; Published 28 April 2023

Academic Editor: Kouqi Liu

Copyright © 2023 Zhendong Gao et al. This is an open access article distributed under the Creative Commons Attribution License, which permits unrestricted use, distribution, and reproduction in any medium, provided the original work is properly cited.

Ordos Basin is a multicycle superimposed cratonic basin in northern China with a simple internal structure and a gentle stratigraphic slope. It is characterized by extensive development, numerous oil and gas-bearing layers, and complete source-reservoir-caprock assemblages. However, the research on continental shale reservoirs and gas-bearing characteristics in the southern part of the basin is not in-depth enough, which restricts the further exploration and development of shale gas in this area. In this paper, the development characteristics of pores and fractures in shale reservoirs and the gas-bearing characteristics of Yanchang Formation shale in the study area are summarized by the comprehensive use of field outcrop, core, and logging, combined with common thin section observation, scanning electron microscope observation, X-ray diffraction analysis, and other methods and techniques. Research indicates that the cement content of the sandstone in the Yanchang Formation reservoir in the south of Ordos is generally 5%-25%. The reservoir also has a large number of primary pores, secondary pores, and microfractures. The gas content of the Yanchang Formation shale represented by Chang 7 is related to both organic matter and pore structure.

1. Introduction

The so-called low permeability reservoir not only refers to its low permeability but also refers to its unique micropore structure. Its pore-throat structure is more dense than the conventional reservoir. At present, the development and exploitation of most oilfields have entered the middle and late stages, and most of them are low- and ultralow permeability reservoirs, which are difficult to develop and different from conventional reservoirs. Low-permeability oil and gas resources are widely distributed around the world, such as in the Permian Basin in the United States and the Bestling, Surgut, Ruskin, and other oil fields in the Siberia region of Russia [1, 2]. With the investment in the exploration and development of low-permeability oil and gas fields, the cumulative proven reserves of low-permeability oil and gas resources in China account for nearly half of the national

oil reserves [3]. Among them, most of the Yanchang Formation in the Ordos Basin is typically low, ultrapermeable, or tight reservoirs, and about 73.7% of the proven oil reserves are distributed in such reservoirs [4].

There are some differences in the discussion of classification and evaluation criteria among scholars from different countries, but basically, the permeability value is used as the criteria for classification of low-permeability reservoirs [5–7]. A reservoir with a permeability of 1 to 10 md is considered as low-permeability reservoir. The reservoir with permeability between 0.1 and 1 md is considered as ultralow-permeability reservoir. Permeability lower than 1 md is considered as tight reservoir. The tight sandstone of the Mesozoic Yanchang Formation in Ordos Basin and the tight sandstone and tight limestone of the Middle Sichuan Jurassic System are the most typical. They are comparable with Bakken tight oil and Eagle Ford tight oil in terms of source

rock, reservoir, formation pressure, crude oil quality, etc. Especially in source reservoir configuration, the tight oil of the Yanchang Formation in the Ordos Basin is even better than Bakken tight oil.

The research focus of low-permeability reservoirs is their microscopic pore structure characteristics. The pore structure of rocks refers to the geometric shape, size, distribution, and interconnection of pores and throats. Therefore, studying the pore-throat characteristics of reservoir rocks alone can help analyze the reservoir more accurately. The size and distribution of pore throats and various forms of their combinations are the controlling factors that affect the reservoir and reservoir percolation properties [8, 9]. Some mature technologies, such as nuclear magnetic resonance, CT scanning, X-ray diffraction, the real sandstone microscopic displacement model, and constant-rate mercury intrusion, have been used to describe the pore microstructure from different angles. In addition, a large number of scholars have studied the pore evolution, physical property changes, and diagenesis of low-permeability-ultralow permeability reservoirs (especially the Ordos Basin) through burial history analysis, tight history restoration, quantitative analysis of porosity evolution, and other methods [10–12]. The research has changed the characteristics of diagenetic evolution from qualitative evaluation to quantitative representation and established favorable reservoir facies belt evaluation indicators, ultralow permeability relatively high-quality reservoirs and “sweet spot” screening comprehensive evaluation methods in the corresponding study area [13].

The Ordos Basin is characterized by “South Oil and North Gas.” The southern part of the basin is the main production area of oil, and the upper Triassic Yanchang Formation reservoir is its main oil-producing layer [14]. However, the Triassic Yanchang Formation oil layer has the characteristics of low and ultralow permeability. The concealment and low production of oil and gas reservoirs increase the difficulty of oil and gas exploration. This paper studies the petrology, pore structure, diagenesis type, and influencing factors of shale reservoir physical properties of a certain area in the southern Ordos Basin by means of drilling and coring, cutting testing, thin section identification, mercury intrusion analysis, and cathodoluminescence observation to provide a theoretical basis for reservoir characterization and gas-bearing evaluation understanding and oil and gas exploration [15–17].

The innovation of this paper is to quantitatively analyze the gas-bearing characteristics of Chang 7 shale in Yanchang Formation, the study area, by using gas logging, on-site analysis, and isothermal adsorption experiments, and to study the shale gas content and its main control factors in different occurrence states.

2. Geological Background

The Ordos Basin is a sedimentary basin with the longest evolution time and the earliest formation history. The basin contains abundant mineral resources such as coal, salt, oil, and conventional and unconventional natural gas. There are widely developed fault zones around the basin, which

are the structural transition zone between the basin and external structural units [18, 19]. The Shajingzi fault zone is connected with the Liupanshan and Yinchuan Basins, and the southern margin of the Hetao Basin is connected to Shaanxi Province in the north and Shanxi Province in the east.

The Ordos Basin was affected by two tectonic movements at the same time, namely, the Tethys Himalayan and Pacific tectonic patterns, forming the platform basement in the Archean and early Proterozoic periods. The development and evolution of the Yanchang Formation objectively recorded the history of the occurrence, development, and extinction of this large freshwater lake basin. The Ordos Basin began to develop in the Chang 10 period, and a series of ring-shaped delta skirts were formed around the center of the lake basin, which quickly sank in the Chang 9 period, and the delta system in the Chang 10 period was completely submerged underwater [20]. By the Chang 8 period, the scale and water depth of the lake basin have increased. When the lake basin in the Chang 7 period developed to its heyday, a large area was submerged by lake water, and the area of the deep lake area also expanded rapidly. In the Chang 6 period, the decline rate of the lake basin slowed down, and the sedimentation was greatly strengthened. Two sedimentary systems developed in the northeast and southwest of the basin, forming a huge delta sedimentary body. Then, the basin sank, and the Chang 4+5 lake basin experienced another brief expansion period. Then, with the reuplift of the crust, the lake basin once again entered a shrinking period; that is, in the Chang 3 and Chang 2 periods, the lake basin was further reduced, and the delta was further swamped. At the end of Chang 1, the lake basin was uplifted to expose the surface, and the whole area became plain and swampy, which ended the deposition process of the Yanchang Formation. The sediments are generally thick in the west and thin in the east, thick in the south and thin in the north.

3. Results and Discussion

3.1. Characteristics of Reservoir Bodies. The reservoirs of the Upper Triassic Yanchang Formation in the southern Ordos Basin are mainly lacustrine delta deposits, of which Chang 2, Chang 3, Chang 6, Chang 8, and Chang 4+5 are the main oil reservoirs. Triassic oilfields mainly include Ansai Oilfield, Majiatan Oilfield, Jing'an Oilfield, Huachi Oilfield, Yanchang Oilfield, Nanliang Oilfield, and Xifeng Oilfield. The Ansai, Zhidan, and Wuqi deltas in the east of the Triassic Yanchang series have the highest degree of exploration. The exploration practice shows that the delta front near the ancient lake shoreline is the main place where large oil fields are distributed. This is because the delta sand body extends directly into the lacustrine source rock, forming a good transport layer; the delta front is developed with estuarine bars, distributary channel sands, and “blobs” and has good reservoirs. In addition, multiple sets of good reservoir cap assemblages have been formed near the shoreline due to the overlapping advance and retreat of lake water. Therefore, it is very beneficial to the formation of oil and gas reservoirs. The delta front facies sand bodies have been widely

distributed and developed for a long time. It is mainly composed of medium-fine-grained feldspar sandstone, with a single layer of 15-20 m, and its physical properties are inferior to those of distributary channel sand bodies, but it still has a certain storage capacity compared with ultralow permeability reservoirs. The Chang 8, Chang 6, Chang 4+5, Chang 3, and Chang 2 reservoirs in the study area of this paper are all sand bodies dominated by underwater distributary channels in the delta front. The delta front facies sand bodies include mouth bars, underwater distributary channels, and the sand bodies superimposed by the two.

The estuary dam is located at the estuary of the branch channel, and the sedimentation rate is the fastest. It is composed of fine and silty sand with good sorting properties. Thin fine sandstone with thick mudstone is distributed at the lower part, and thick fine sandstone with thin mudstone is distributed upward, showing a typical reverse rhythm structure vertically, reflecting the transformation of hydrodynamic conditions from low energy to high energy. Small troughed cross-bedding and deformation structures are common in sandstones, with water ripple marks visible and few biological fossils. The sand body of the estuary bar has an obvious antigrain structure, a flat bottom and convex top, and multiphase superposition. Each grain sequence cycle ends with the mudstone at the bottom turning upwards into argillaceous siltstone, siltstone, silt-fine sandstone, and fine sandstone. The thickness of a single layer of sandstone is generally 3-4 m, and the mudstone is often separated by 1-2 m. The sandstone foreset has well-developed bedding, uniform grain size, and generally high porosity and permeability, making it the best reservoir rock in the delta system. Generally, it occurs when the end of the underwater distributary river in the delta front extends into the shallow lake, and it is distributed in florets. The underwater distributary channel sand body is the underwater extension of the distributary channel of the delta plain. The shape of the sand body is similar to that of the water distributary channel sand body. The top is flat, and the bottom is convex. However, the particle size is finer than that of distributary channels. Affected by lake waves, sand bodies are widely distributed in layers with good connectivity. The composite sand body is longitudinal, the lower part is the estuary sand bar, and the upper part is the composite sand body cut and superimposed by the underwater distributary channel sand bar.

The Yanchang Formation sand body has medium structural maturity and low compositional maturity. The Chang 7 Formation is composed of black shale, dark mudstone, fine sandstone, siltstone, and tuff. The Chang 8 reservoir sandstone is dominated by fine-grained and medium-grained lithic feldspar sandstone. The Chang 6 sandstone is dominated by fine-grained lithic feldspar sandstone and feldspar sandstone. The Chang 4+5 sandstone is dominated by fine-grained lithic sandstone. The Chang 3 reservoir sandstone is dominated by fine-grained lithic feldspar sandstone and feldspar sandstone. The Chang 2 sandstone is dominated by fine-grained and medium-grained feldspar sandstone. The mica content of Yanchang Formation sandstone cuttings is very high. Extrusive rock, quartz sandstone, argillite, chert, phyllite, metamorphic quartzite, and schist are com-

mon, in addition to a small amount of chlorite cuttings, dolomite cuttings, and tuff. The cement content of the upper Triassic Yanchang Formation reservoir sandstone in the Ordos Basin is generally 5%-25%, mainly calcite, iron calcite, authigenic chlorite, kaolinite, illite, turbidite, dolomite, iron dolomite, Silica, etc. Turbidite, as the most characteristic cement in the Ordos Basin, is very unevenly distributed in the Yanchang Formation reservoir sandstone, with local distribution on the plane and discontinuous distribution on the vertical facies.

3.2. Pore Structure. The shale reservoir is very dense and has the characteristics of small particle size, complex mineral composition and structure, and strong heterogeneity. The reservoir space of the shale reservoir can not only store fluid but also provide space for fluid seepage. It can be mainly divided into two categories: pore and fracture.

In a broad sense, porosity refers to the space in the rock that is not filled by solid materials, including macroscopic cracks and microscopic pores. Microporosity refers to the interspace between rock particles, in particles (grains), and in fillings. Primary pores include primary intergranular pores and interstitial micropores. We can better identify the primary intergranular pores that have not been significantly changed by diagenesis. For example, when the intergranular pores are lined with chlorite membranes, we can basically think that the intergranular pores are the primary cause. However, in most cases, it is difficult for us to distinguish between the primary and secondary components in the intergranular pores. Therefore, in fact, the intergranular pores include primary and secondary pores, but the primary ones are the main ones.

Intergranular pores refer to the pores formed after primary intergranular pores are partially filled and transformed by interstitials during the burial and diagenesis of sandy sediments, mainly residual intergranular pores, which are generally classified as "primary pores." Such pores are generally larger in size and have good pore connectivity. This type of pore dominates the reservoirs in the study area, and residual intergranular pores are developed in each target interval. From the thin slice, the unfilled intergranular pores are mostly polygonal, with the most triangles, and the pore edges are neat and straight. A scanning electron microscope shows that ferric calcite and ferric dolomite are scattered in the pores, metasomatic debris can be seen, and the edges of some residual intergranular pores are wrapped by the early chlorite shell, which effectively prevents the secondary growth of particles. The intergranular pore size is larger, and the connectivity is good, which is the main contributing pore. In addition, it is found that the residual intergranular pores after the secondary increase of quartz are small in pore size and poor in connectivity. The micropores in the interstitial material refer to the micropores in the argillaceous matrix deposited at the same time as the sandy debris in the sandstone and the intercrystalline micropores of the sandstone authigenic minerals. It is the micropores between the authigenic clays and carbonate wafers that fill and replace the feldspar between the particles. The micropores in the interstitial material are extremely small, generally

smaller than those that can only be seen under the scanning electron microscope, which is commonly found in authigenic clays and carbonate cements. Most of these pores disappear after compaction, and only a part of them are distributed in fine sandstone with high argillaceous content. Most of the authigenic quartz and kaolinite intercrystalline micropores can be seen in the study area. Pores are small in size, uneven in distribution, and poor in connectivity.

The shale secondary pores in this area are dominated by dissolution-type secondary pores. The distribution of such pores is very limited, and the pore size is relatively small. They have a certain contribution to the pore performance of shale reservoirs. The study area has dissolved secondary pores. Through the observation and analysis of cast thin sections and a scanning electron microscope, the pores in the dissolved grains are mostly found in the feldspar grains, and the pores in the dissolved candle grains are often connected with the pores between the dissolved candle grains.

In the Triassic Yanchang Formation of the Ordos Basin, fractures are well-developed. No matter whether in outcrops around the basin or in core logging in the hinterland of the basin, natural fractures are found. Fractures are important seepage channels and effective reservoir spaces for oil and gas in low-permeability reservoirs in the Ordos Basin. Fractures are common in shale cores and thin slices. In shale reservoirs, microfractures formed due to in situ stress are small flakes with curved fracture surfaces. The crack width is generally parallel to the direction of the minimum in situ stress. In the study area, the width of such fractures is between less than a micron and tens of microns, and the fractures account for a small proportion of the total porosity of the rock. Another feature is that when the in situ stress changes significantly, the fracture changes. If the in situ stress increases along the vertical direction of the fracture, the fracture closes, resulting in a sharp drop in the formation permeability.

3.3. Evaluation of Gas-Bearing Properties. Shale gas occurs in a variety of forms. Most shale gas exists on the surface of particles and organic matter in the form of an adsorbed phase or in pores and fractures in the form of a free phase. In addition, a small amount of shale gas exists in fluids in the form of a dissolved phase. The occurrence state of shale gas in various shale gas reservoirs at home and abroad is different. Curtis [21] pointed out that the adsorbed shale gas accounts for 20%~85% of the total shale gas in five sets of shale gas reservoirs in North America. Barton et al. [22] studied the Antrim shale in the Michigan Basin and believed that the shale in this area was mainly in the adsorbed state, and the free shale gas accounted for 25%~30% of the total shale gas. Guo et al. [23] believed that the shale gas of the Yanchang Formation in the south of the Ordos Basin exists in three states: adsorbed state, free state, and dissolved state.

This section takes the Chang 7 section as the research object to further analyze the gas-bearing properties of the Yanchang Formation. According to the field analysis and test results of 74 Yanchang Formations in 8 wells, the total gas content of Chang 7 shale in each well was finally obtained. Similar to the qualitative evaluation results of

gas-bearing characteristics based on the total hydrocarbon value, the total gas content obtained by the on-site analytical method generally also has a decreasing trend from west to east and from south to north. Among them, the total gas content of the wells in the southwest is relatively high, with an average of $4.35 \text{ m}^3/\text{t}$, the total gas content of the wells in the east is slightly reduced, with an average of $2.98 \text{ m}^3/\text{t}$, and the total gas content of the wells in the south is relatively low, with an average of $2.14 \text{ m}^3/\text{t}$.

The adsorbed gas is natural gas in the adsorption state. Kerogen, clay minerals, and matrix pores can provide places for adsorption gas accumulation. Because the adsorbed gas usually contributes a lot to the total gas content, research on the adsorption capacity is of great significance for judging the gas-bearing characteristics. Isothermal adsorption experiments are one of the basic methods to study shale adsorption capacity and reservoir space characteristics. This experiment can obtain the maximum adsorbed gas content of shale.

Based on the Langmuir volume and the Langmuir pressure obtained from isothermal adsorption experiments, the adsorbed gas content of multiple samples in the Chang 7 section under the formation temperature and pressure conditions is calculated using the Langmuir formula. Research shows that the Langmuir volume of Chang 7 shale samples from the Yanchang Formation in the study area is relatively large, with an average of $4.55 \text{ m}^3/\text{t}$. The Langmuir pressure is relatively low, with an average of 2.53 MPa, and the adsorption capacity is large, with an average of $2.87 \text{ m}^3/\text{t}$ (Figures 1–3). The above characteristics indicate that the Chang 7 shale in the Yanchang Formation in the study area has a strong adsorption capacity.

Previous studies have shown that the adsorption capacity of shale for methane and other gases is roughly positively correlated with the total organic carbon content. The organic carbon content is one of the important factors affecting the adsorption capacity of shale. By analyzing the correlation between the maximum methane adsorption capacity (pumping advance), total organic carbon content, and kerogen content of the Chang 7 shale samples in the Yanchang Formation in the study area, the results show that the methane adsorption capacity is significantly related to the total organic carbon content and kerogen content. A good positive correlation (Figures 4 and 5) shows that the adsorption capacity of Chang 7 shale in the Yanchang Formation in the study area generally increases with the increase in organic matter content.

The thermal evolution stage of organic matter has an important impact on the occurrence mode and gas-bearing characteristics of shale gas. On the one hand, the more mature the organic matter, the greater the total hydrocarbon generation; on the other hand, after the organic matter generates hydrocarbons, the volume shrinkage will generate micropores, which is beneficial to the preservation of shale gas. Through the correlation analysis of the maximum methane adsorption capacity (pumping advance), the maximum pyrolysis temperature, and the hydrogen index of the Chang 7 shale samples in the Yanchang Formation in the study area (Figures 6 and 7), the results show that with the increase in

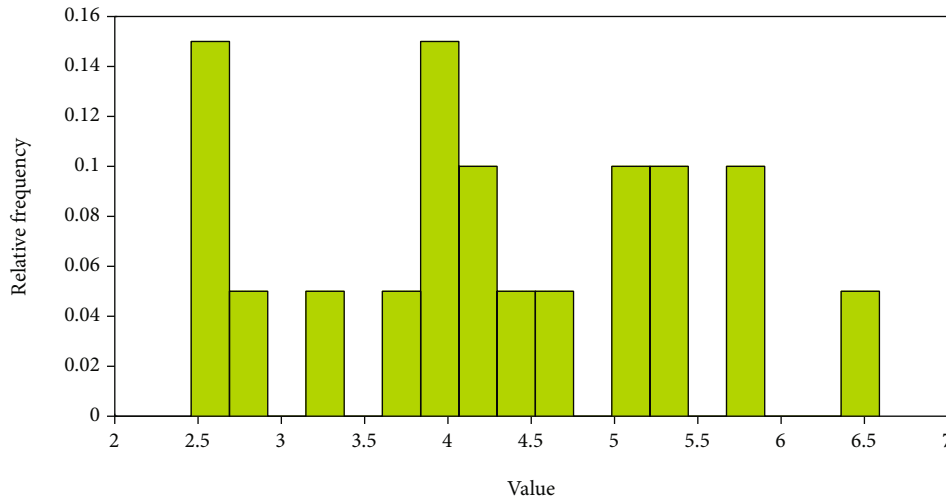


FIGURE 1: Langmuir volume histogram.

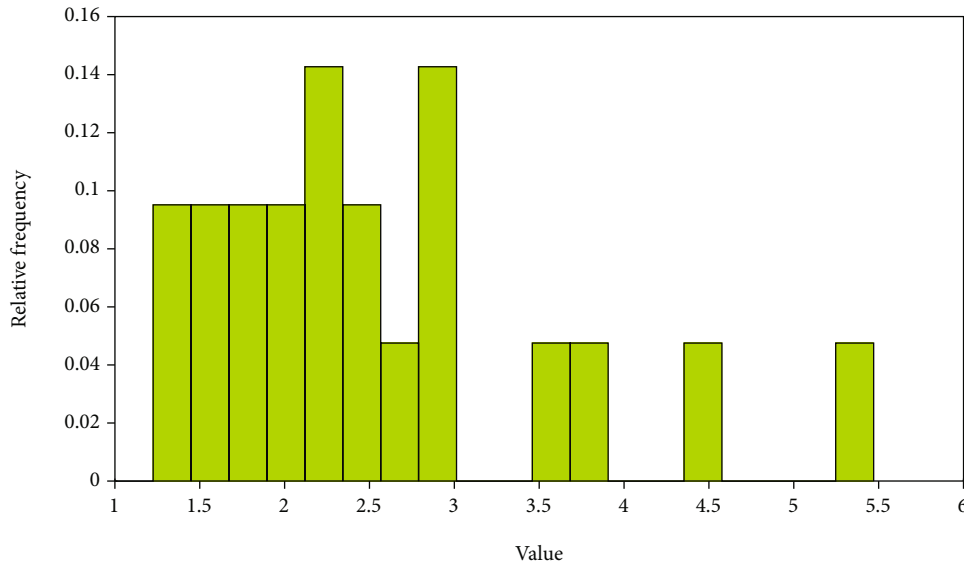


FIGURE 2: Langmuir pressure histogram.

temperature and the decrease in hydrogen index, the maximum amount of adsorbed gas in the shale also increases. It shows that the improvement of shale organic matter maturity is beneficial to the adsorption of shale gas.

Through the correlation analysis between the maximum methane adsorption amount of shale samples (the organic matter extraction advance) and the content of clay minerals, the results show that there is a certain positive correlation between the two, and the correlation is relatively poor, indicating that the adsorption of clay minerals to shale gas content has a certain effect. Micropores, especially those smaller than 50 nm, are the main determinant of the surface area of clay, which is closely related to the gas adsorption capacity of clay minerals. The clay minerals in the Chang 7 shale of the Yanchang Formation in the study area are mainly illite-mixed layers, followed by illite, with relatively low contents of chlorite and kaolinite. The results show that the maxi-

imum adsorption capacity has a positive correlation with the content of the illite/smectite mixed layer in general, while the correlation with the content of illite is not obvious, indicating that the adsorption capacity of the Chang 7 shale clay minerals in the Yanchang Formation in the study area is mainly related to the development degree of the illite/smectite mixed layer (Figure 8).

In order to study the relationship between pores and pore structure and the adsorption capacity of shale, the maximum methane adsorption capacity (pumping advance) of Chang 7 shale samples in the Yanchang Formation was analyzed for the correlation between the specific surface of meso-macropores and the specific surface of micropores. It shows that there is no obvious correlation between the maximum adsorption capacity and the specific surface of medium macropores but has a good positive correlation with the specific surface of micropores (Figure 9). That is,

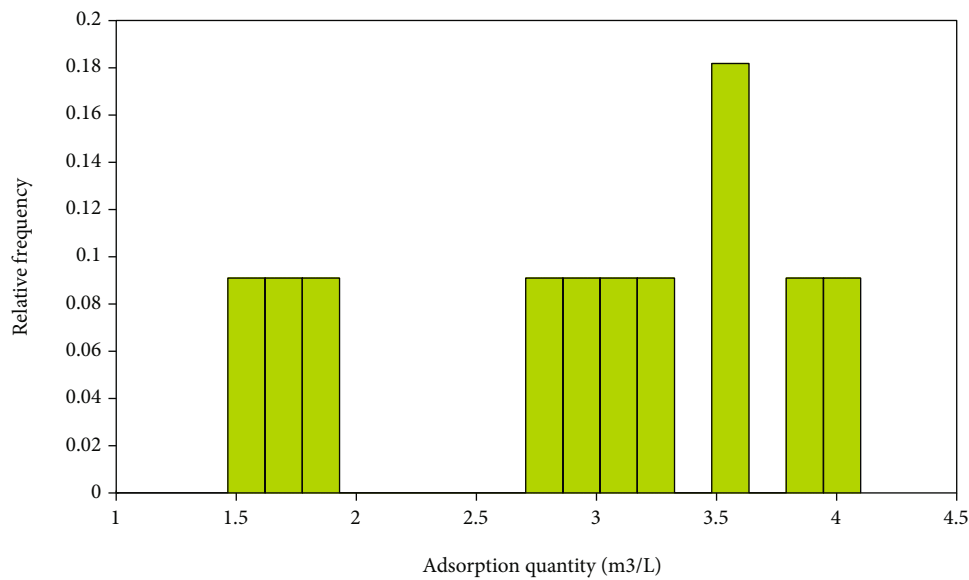


FIGURE 3: Adsorption volume histogram.

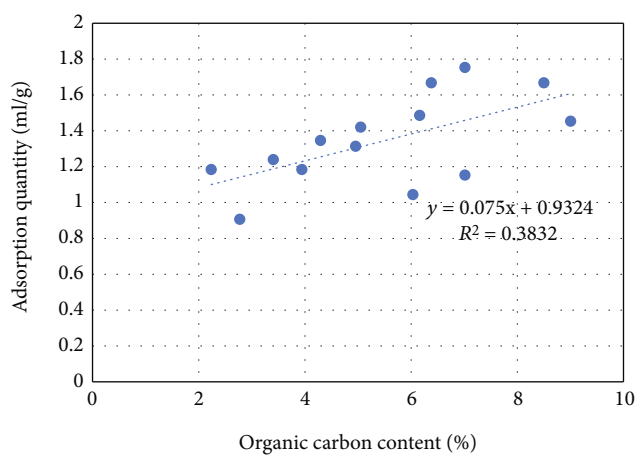


FIGURE 4: Relationship between the maximum amount of methane adsorbed and the total organic carbon content of the Chang 7 shale sample in the Yanchang Formation.

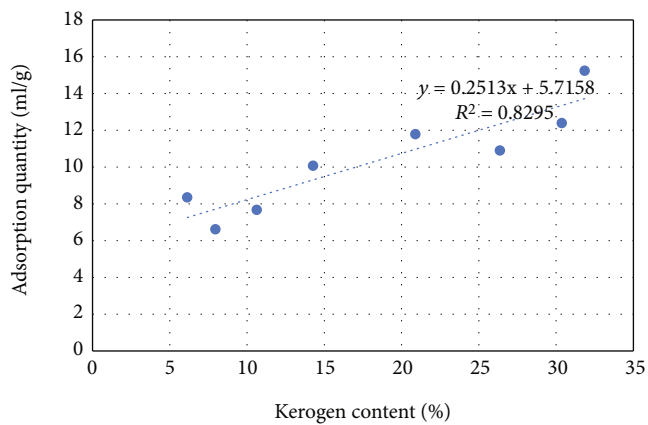


FIGURE 5: Relationship between maximum methane adsorption and kerogen content in the Yanchang Formation Chang 7 shale sample.

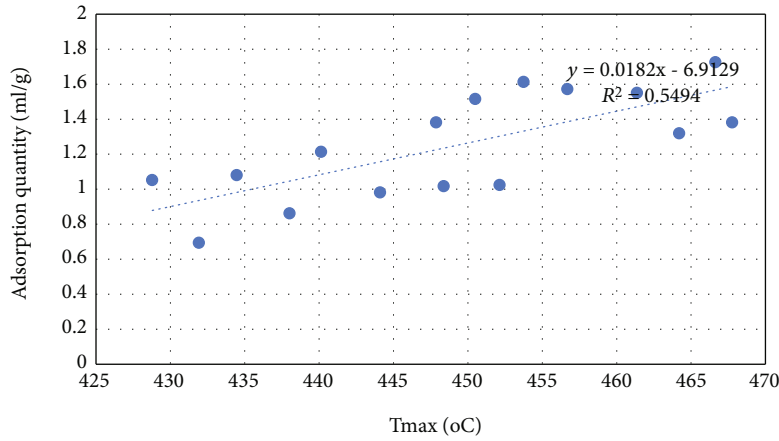


FIGURE 6: Relationship between maximum adsorption capacity and T_{max} of Chang 7 shale sample in the Yanchang Formation.

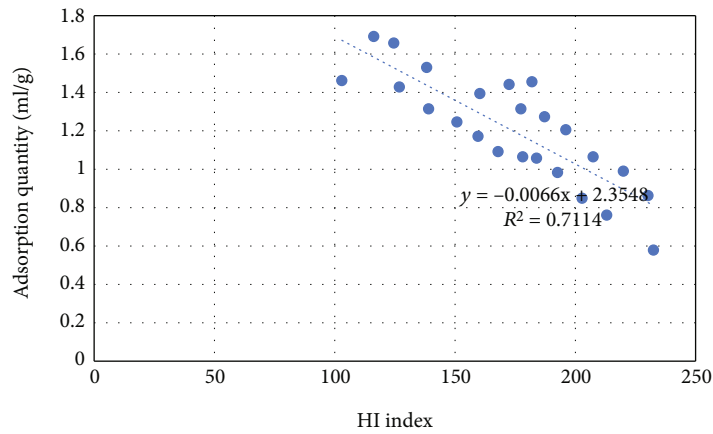


FIGURE 7: Relationship between maximum adsorption capacity and hydrogen content index of Chang 7 shale sample in the Yanchang Formation.

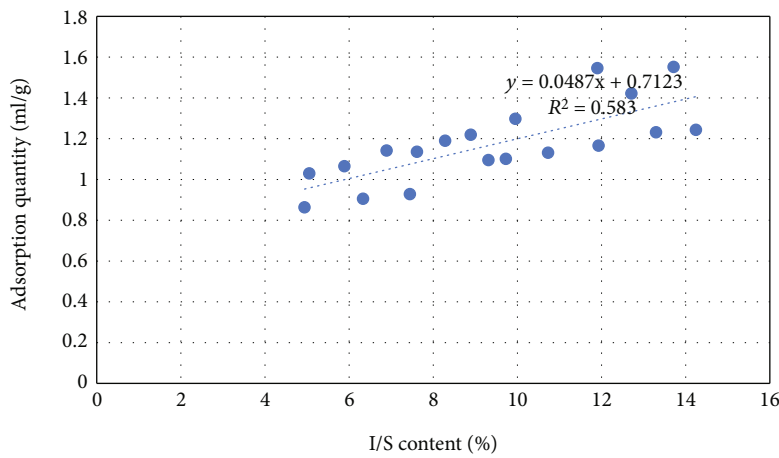


FIGURE 8: Relationship between the maximum adsorption capacity and the content of I/S mixed layers in Chang 7 shale samples.

the development of micropores in Chang 7 shale in the Yanchang Formation in the district has a certain contribution to the content of adsorbed gas in shale.

In essence, the main factors affecting the gas content of adsorbed gas in the above aspects are directly or indirectly related to the development of micropores; the direct

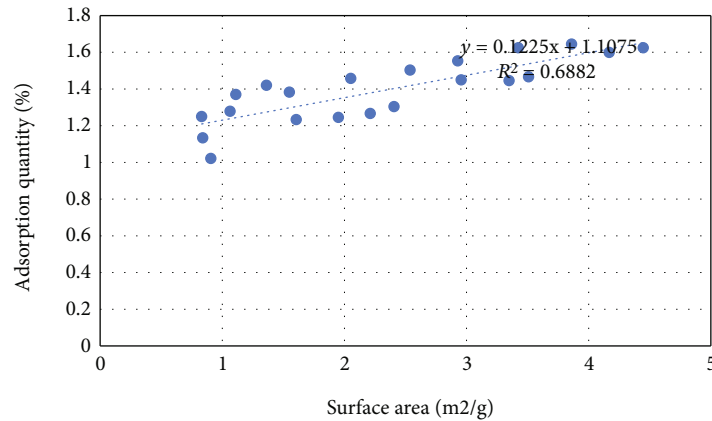


FIGURE 9: Relationship between the maximum adsorption capacity and the micropore-specific surface of the Chang 7 shale sample in the Yanchang Formation.

correlation is shown in that the specific surface area of micropores is positively correlated with the content of adsorbed gas, but not with the surface area of medium to large pore ratios. The indirect correlation is mainly related to the location of micropores, and some micropores are mainly developed in the pore space between and within organic matter. The development of micropores in the other part is mainly related to clay minerals. The reason is that the adsorption gas in shale reservoir is mainly physical adsorption, mainly caused by the van der Waals molecular force. The above characteristics determine that micropores are the most favorable places for adsorption gas enrichment.

4. Conclusion

This paper comprehensively uses the field outcrop, core, and logging data, combined with common thin section observation, a scanning electron microscope observation, X-ray diffraction analysis, and other methods and techniques, summarizes the characteristics of shale reservoir pores and fractures, and makes a quantitative analysis of the gas-bearing characteristics of the shale of the Yanchang Formation in the south of Ordos. The conclusions are as follows:

- (1) Yanchang Formation reservoirs have medium structural maturity and low compositional maturity. The cement content of the upper Triassic Yanchang Formation reservoir sandstone in the Ordos Basin is generally 5%-25%, mainly calcite, iron calcite, authigenic chlorite, kaolinite, illite, turbidite, dolomite, iron dolomite, silica, etc.
- (2) The pores are mostly authigenic quartz and kaolinite intercrystalline micropores. Pores are small in size, uneven in distribution, and poor in connectivity. The study area is dominated by the dissolution secondary pores
- (3) The Chang 7 shale in the Yanchang Formation in the study area has a strong adsorption capacity. With the increase in the maximum pyrolysis temperature of the shale and the decrease in the hydrogen index,

the maximum adsorption capacity of the shale also increases. The maximum adsorption capacity in the study area is positively correlated with the content of the illite/smectite mixed layer, but the correlation with the content of illite is not obvious. There is no obvious correlation between the maximum adsorption capacity and the specific surface of meso-macropores, but it has a good positive correlation with the specific surface of micropores

Data Availability

The figures used to support the findings of this study are included in the article.

Conflicts of Interest

The authors declare that they have no conflicts of interest.

Acknowledgments

The authors would like to show sincere thanks to those techniques who have contributed to this research.

References

- [1] M. Li, X. Pang, L. Xiong et al., "Application of mathematical statistics to shale gas-bearing property evaluation and main controlling factor analysis," *Scientific Reports*, vol. 12, no. 1, p. 9859, 2022.
- [2] D. Xiao, S. Lu, M. Shao, N. Zhou, R. Zhao, and Y. Peng, "Comparison of marine and continental shale gas reservoirs and their gas-bearing properties in China: the examples of the Longmaxi and Shahezi shales," *Energy & Fuels*, vol. 35, no. 5, pp. 4029–4043, 2021.
- [3] W. Jianfa, Z. Shengxian, F. Cunhui et al., "Fracture characteristics of the Longmaxi Formation shale and its relationship with gas-bearing properties in Changning area, southern Sichuan," *Acta Petrolei Sinica*, vol. 42, no. 4, p. 428, 2021.
- [4] K. Wang, F. Du, X. Zhang, L. Wang, and C. Xin, "Mechanical properties and permeability evolution in gas-bearing coal-

- rock combination body under triaxial conditions,” *Environmental Earth Sciences*, vol. 76, no. 24, 2017.
- [5] A. L. Anderson and L. D. Hampton, “Acoustics of gas-bearing sediments. II. Measurements and models,” *America*, vol. 67, no. 6, pp. 1890–1903, 1980.
- [6] T. Xuan, Z. H. A. N. G. Jin-Chuan, D. I. N. G. Wen-Long et al., “The reservoir property of the upper Paleozoic marine continental transitional shale and its gas bearing capacity in the southeastern Ordos Basin,” *Earth Science Frontiers*, vol. 23, no. 2, p. 147, 2016.
- [7] S. P. Meng, J. X. Zhang, H. Liu, and S. S. Liu, “Relationship between the methane carbon isotope and gas-bearing properties of coal reservoir,” *Journal of China Coal Society*, vol. 39, no. 8, pp. 1683–1690, 2014.
- [8] H. Zhang, Z. Lun, X. Zhou, H. Wang, C. Zhao, and D. Zhang, “Role of H₂O of gas-bearing shale in its physicochemical properties and CH₄ Adsorption performance alteration due to microwave irradiation,” *Energy & Fuels*, vol. 35, no. 23, pp. 19464–19480, 2021.
- [9] Y. F. N. Z. H. Changpeng and W. B. P. K. L. Huiqing, “Characterization of microscopic pore structures in shale reservoirs,” *Acta Petrolei Sinica*, vol. 34, no. 2, p. 301, 2013.
- [10] B. Yan, Y. Wang, and J. E. Killough, “Beyond dual-porosity modeling for the simulation of complex flow mechanisms in shale reservoirs,” *Computational Geosciences*, vol. 20, no. 1, pp. 69–91, 2016.
- [11] E. Ozkan, M. Brown, R. Raghavan, and H. Kazemi, “Comparison of fractured-horizontal-well performance in tight sand and shale reservoirs,” *SPE Reservoir Evaluation & Engineering*, vol. 14, no. 2, pp. 248–259, 2011.
- [12] A. H. Kohli and M. D. Zoback, “Frictional properties of shale reservoir rocks,” *Journal of Geophysical Research - Solid Earth*, vol. 118, no. 9, pp. 5109–5125, 2013.
- [13] N. Alharthy, T. Teklu, H. Kazemi et al., “Enhanced oil recovery in liquid-rich shale reservoirs: laboratory to field,” *SPE Reservoir Evaluation & Engineering*, vol. 21, no. 1, pp. 137–159, 2018.
- [14] Y. Niu, C. Wang, E. Wang, and Z. Li, “Experimental study on the damage evolution of gas-bearing coal and its electric potential response,” *Rock Mechanics and Rock Engineering*, vol. 52, no. 11, pp. 4589–4604, 2019.
- [15] H. Cheng, Y. Dong, C. Lu, Q. Qin, and D. Cadasse, “Intelligent oil production stratified water injection technology,” *Wireless Communications and Mobile Computing*, vol. 2022, Article ID 3954446, 7 pages, 2022.
- [16] Z. K. Hou, H. L. Cheng, S. W. Sun, J. Chen, D. Q. Qi, and Z. B. Liu, “Crack propagation and hydraulic fracturing in different lithologies,” *Applied Geophysics*, vol. 16, no. 2, pp. 243–251, 2019.
- [17] J. Han, H. Cheng, Y. Shi, L. Wang, Y. Song, and W. Zhnag, “Connectivity analysis and application of fracture cave carbonate reservoir in Tazhong,” *Science Technology and Engineering*, vol. 16, no. 5, pp. 147–152, 2016.
- [18] H. Cheng, J. Wei, and Z. Cheng, “Study on sedimentary facies and reservoir characteristics of Paleogene sandstone in Yingmaili Block, Tarim Basin,” *Geofluids*, vol. 2022, Article ID 1445395, 14 pages, 2022.
- [19] H. Cheng, P. Ma, G. Dong, S. Zhang, J. Wei, and Q. Qin, “Characteristics of carboniferous volcanic reservoirs in Beisantai Oilfield, Junggar Basin,” *Mathematical Problems in Engineering*, vol. 2022, Article ID 7800630, 10 pages, 2022.
- [20] K. Peng, S. Shi, Q. Zou, Y. Zhang, and G. Tan, “Gas permeability characteristics and energy evolution laws of gas-bearing coal under multi-level stress paths,” *Natural Resources Research*, vol. 29, no. 5, pp. 3137–3158, 2020.
- [21] J. B. Curtis, “Fractured shale-gas systems,” *AAPG Bulletin*, vol. 86, no. 11, pp. 1921–1938, 2002.
- [22] J. M. Barton Jr, W. P. Barnett, E. S. Barton et al., “The geology of the area surrounding the Venetia kimberlite pipes, Limpopo Belt, South Africa: a complex interplay of nappe tectonics and granitoid magmatism,” *South African Journal of Geology*, vol. 106, no. 2-3, pp. 109–128, 2003.
- [23] H. Guo, W. Jia, Y. Lei et al., “The composition and its impact on the methane sorption of lacustrine shales from the Upper Triassic Yanchang Formation, Ordos Basin, China,” *Marine and Petroleum Geology*, vol. 57, pp. 509–520, 2014.